γ-ray Spectroscopy of ^{106}Cd and a Shell-Model based Deformation Analysis of $^{100-110}$Cd Isotopes

Inaugural-Dissertation

zur

Erlangung des Doktorgrades

der Mathematisch-Naturwissenschaftlichen Fakultät

der Universität zu Köln

vorgelegt von

Tobias Schmidt

aus Emsdetten

Köln

2019

Berischterstatter: (Gutachter)	Prof. Dr. Jan Jolie
	Prof. Dr. Alfred Dewald

Tag der mündlichen Prüfung: 23.08.2019

Zusammenfassung

Ein ^{106}Cd(p, $p'\gamma$) Streuexperiment wurde am FN-Tandembeschleuniger des Instituts für Kernphysik an der Universität zu Köln mit dem SONIC@HORUS-Spektrometer durchgeführt. Die Datenanalyse fokussierte sich auf eine detaillierte γ-Spektroskopie und die Bestimmung von Verzweigungsverhältnissen der γ-Strahlen. Zahlreiche neue Ergebnisse konnten gewonnen werden. Zusammengefasst wurden 64 neue γ-Übergänge und 20 neue Anregungszustände entdeckt. Unstimmigkeiten zwischen vorangegangenen Arbeiten zur Untersuchung von ^{106}Cd konnten aufgelöst werden. Für acht Anregungszustände aus der Literatur (NNDC) wurde gezeigt, dass sie falsch platziert sind oder nicht existieren, 14 Verzweigungsverhältnisse konnten signifikant korrigiert werden. Das unbereinigte Spektrum von ^{106}Cd wies eine hohe Dichte an γ-Übergängen auf, erkennbar an der Entdeckung 23 neuer Multipletts von insgesamt 32 beobachteten Multipletts. Dennoch konnten die Verzweigungsverhältnisse für jeden beobachteten γ-Übergang bestimmt werden.

Starke Hinweise für ein Intruderband in ^{106}Cd ergaben sich aus einem neu entdeckten Anregungszustand. Ein starkes Matrixelement, dass den Zustand mit dem Band verknüpft, konnte aus dem Verzweigungsverhältnis abgeschätzt werden. Durch die Einordnung dieser Ergebnisse zu bereits bekannten Ergebnissen der Nachbarisotopen, wird die Existenz eines 4_I^+-Intruderbandmitgliedes mit behauptet.

Die experimentellen Ergebnisse von ^{106}Cd dieser Arbeit wurden mit Daten einer Schalenmodellberechnung verglichen, indem Levelschemata aus dem experimentellen und dem theoretischen Datensatz gebildet wurden. Dabei wurden Informationen über unveröffentlichte mittlere Lebenszeiten aus einer neuerlichen Analyse eines ^{106}Cd(n, $n'\gamma$)-Datensatzes mit den γ-Verzweigungsverhältnissen dieser Arbeit kombiniert.

Zusätzliche Schalenmodellberechnungen für die geraden Isotope $^{100-110}$Cd wurden durchgeführt. Rotationsinvariante wurden aus den $B(E2)$-Werten des Schalenmodells für die Grundzustände dieser Kerne gewonnen. Die effektiven Deformationsparameter β_{eff} und γ_{eff} wurden zum ersten mal zusammen mit ihren Varianzen $\sigma(\beta)$ und $\sigma(\gamma)$ aus Schalenmodelldaten abgeleitet. Die Ergebnisse wurden mit Begrifflichkeiten von IBM-Symmetrien interpretiert. In diesem Zusammenhang wurde festgestellt, dass sich die Isotopenkette $^{100-110}$Cd von einer $U(5)$-artigen, Vibratorstruktur hin zu einem $O(6)$-artigen, assymetrischen, γ-soften Rotor gegen Mitte der Neutronenschale wandelt.

Abstract

A ^{106}Cd(p, $p'\gamma$) experiment was performed at the FN tandem accelerator at the Institute for Nuclear Physics at the University of Cologne, using the SONIC@HORUS spectrometer. The data analysis focused on a detailed γ-ray spectroscopy and the determination of γ-ray branching ratios. Numerous new results could be obtained. In summary, 64 new γ-transitions and 20 new levels were discovered. Discrepancies between former works, studying ^{106}Cd could be solved. Eight levels stated in the literature (NNDC) were proven to be falsely placed or not existing, 14 branching ratios could be corrected significantly. The singles spectrum of ^{106}Cd exhibited a high density of γ-rays, indicated by the discovery of 23 new multiplets among an overall observation of 32 multiplets. Though, branching ratios could be obtained for every observed γ-transition.

Strong hints for an intruder band in ^{106}Cd are given by a newly discovered level. A strong matrix element connecting the state to the band could be estimated by the branching ratio. By classifying this results to known results of neighboring isotopes, a 4_I^+ member of the intruder band is suggested.

The experimental results of ^{106}Cd of this work were compared to data of a shell-model calculation by the construction of level schemes from the experimental and theoretical data sets. Thereby, unpublished mean lifetime information from a recent analysis of a ^{106}Cd(n, $n'\gamma$) data set were combined with γ-ray branching ratios of this work.

Additional shell-model calculations were performed for the even isotopes $^{100-110}$Cd. Rotational invariants were extracted from shell-model $B(E2)$-values for the ground states of these nuclei. The effective deformation parameters β_{eff} and γ_{eff}, including their variances $\sigma(\beta)$ and $\sigma(\gamma)$, were derived for the first time from shell-model data. The results were interpreted in terms of IBM-symmetries. It was found in this context, that the chain of isotopes $^{100-110}$Cd transform from a $U(5)$-like, vibrator structure towards a $O(6)$-like, asymmetric, γ-soft rotor at the middle of the neutron shell.

Contents

1 Introduction **1**

2 γ-transitions in nuclei **5**
2.1 Transition strength 5
2.2 Branching ratios 6

3 (p, p') Experiment on ^{106}Cd **8**
3.1 Motivation 8
3.2 The SONIC@HORUS setup at the FN-Tandem Accelerator Cologne 8
3.2.1 Experimental settings and detector setup 8
3.2.2 Data acquisition and data processing 10
3.3 Calibration 11
3.3.1 Energy Calibration 11
3.3.2 Efficiency Calibration 12
3.4 General data analysis methods 14
3.5 Experimental Results 15

4 Shell-Model Calculations and Comparison to experimental Data **52**
4.1 The Nuclear Shell Model 52
4.2 Shell-Model calculations of cadmium isotopes 53
4.2.1 Comparison of level schemes for ^{106}Cd 54

5 Possible intruder band in ^{106}Cd **58**

6 A shell-model based deformation analysis of even Cd-isotopes **63**
6.1 Deformation parameter 63
6.2 Shape invariants 64
6.3 Convergence study of invariants 66
6.4 Deformation analysis 72

7 Summary, conclusion, outlook **79**

A Addition (p, p')-data analysis **81**

B Addition to convergence study of rotational invariants **84**

C Addition to deformation analysis **87**

1 Introduction

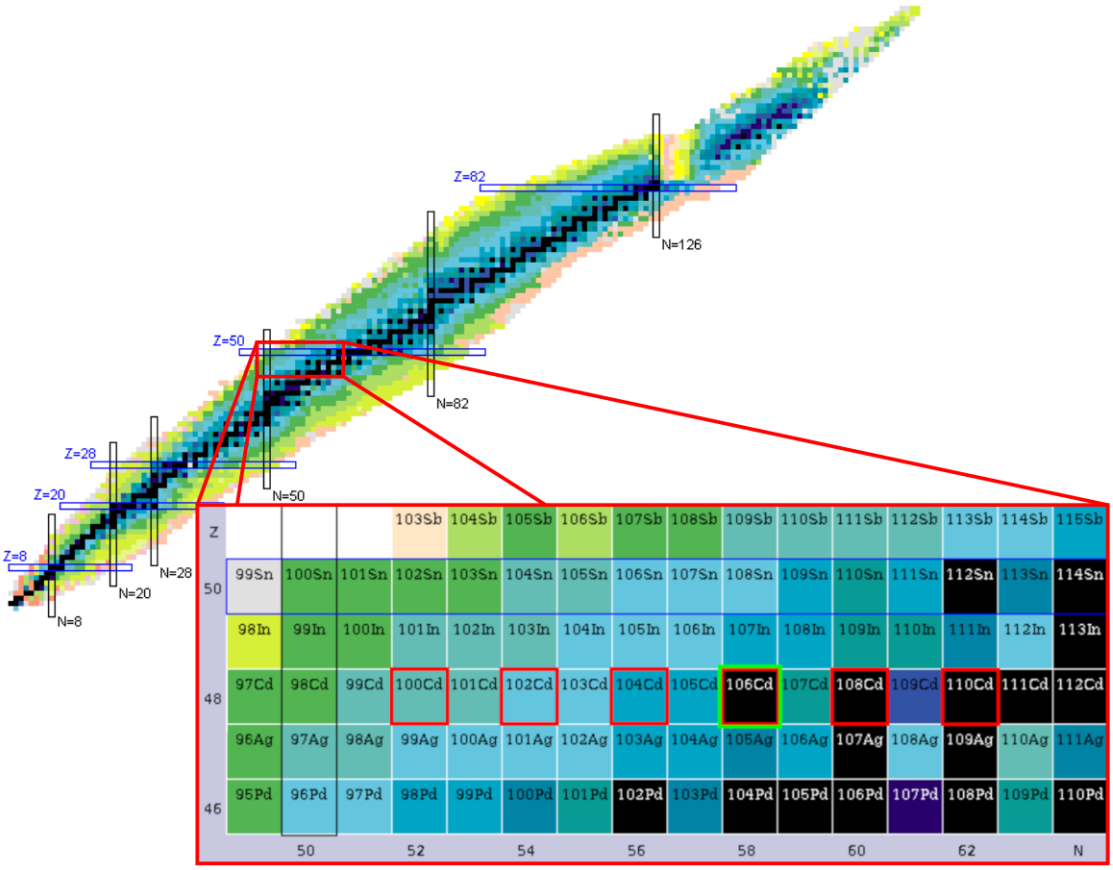

Figure 1.1: The nuclear chart with a magnification of the region of the cadmium isotopes. Nuclei in red squares are part of a deformation analysis. Additionally, in green color ^{106}Cd, which is spectroscopically analyzed by a (p, p') experiment. As can be seen, the cadmium nuclei lie in vicinity of the proton $Z = 50$ shell, while ^{98}Cd closes the neutron $N = 50$ shell. Figure adopted from Ref. [1].

The atomic nucleus is a complex quantum mechanical object. Understanding nuclear structure is still a matter of current research. The fact, that no exact analytical expression for the strong force acting between nucleons is at hand, points to the difficulty of understanding the nuclear system in all its details. To get insights into the nuclear structure, it is crucial to have models of the nuclear system that allow satisfying predictions.

In the very beginning of the field of nuclear physics, the *liquid drop model* of Bethe and Weizesäcker [2] (1935) was derived. In this model the nuclear matter is considered as a fluid-like structure, in which nucleons behave more or less like molecules in a droplet. This model was especially successful in predicting binding energies of the nuclei. From this picture, A. Bohr and B. Mottelson developed their

geometrical collective model [3] (1953) with the concept that the nuclear droplet forms characteristic shapes. Nuclei were classified in vibrator or rotor types in which the nucleons perform collective motions accordingly. This foundational approach allowed the prediction of level energies and transition strength, characteristic for each of the two types of collectivity. As the cadmium nuclei exhibited energy spectra typical for a harmonic vibrator, they became text-book examples for this case of collective motion [4, 5, 6] for many years based mostly on excitation energy information [7]. Figure 1.1 shows a magnification of the section of interest on the nuclear chart, where the light part of the cadmium chain can be seen close to the $Z = 50$ proton shell closure. The vicinity of the closed proton shell led furthermore to the assumption, that the cadmium isotopes exhibit a spherical shape. This additionally supported the picture of a nuclear sphere undergoing harmonic vibrations [8]. The top of Figure 1.2 displays the level scheme of the harmonic vibrator as predicted by the geometrical model. Similarities to the experimental level distribution of ^{112}Cd, shown in the bottom of Figure 1.2, are apparent. Unlike presented in Figure 1.2, the information on transition strengths was very scarce until the 1990s [9, 10]. And as energy levels nicely matched to the predicted pattern of the harmonic vibrator, there was no doubt about the validity of this picture for many years. Deviations in the level distribution and relative transition strengths were explained by anharmonicities of the vibrator [4, 5, 6].

Over time additional 0^+ and 2^+ states where discovered next to the two phonon triplet. These *intruder states* originate from particle hole excitations (2p-2h), where a proton pair (2p) gets placed across the $Z = 50$ major shell gap, leaving 2 proton holes (2h) in the $Z = 28 - 50$ shell. This results in 4 additional valence quasiparticles. The 2p-2h excitations are favored by the attractive quadrupole interaction of valence protons and neutrons, and thus the lowest excitation energies are found in the middle of the $N = 50 - 82$ neutron shell [8]. In the 1980s the idea of configuration mixing between the vibrational structure and the intruder states was introduced [11, 12, 13]. This approach could successfully explain anharmonicities and deviations in the relative transition strengths compared to the ideal vibrator as present in the cadmium isotopes. A rich description of dynamical symmetries in atomic nuclei thereby was founded in the mid 1990s. A, so-called, global coupling could be well established in the cadmium nuclei, in which a vibrational, $U(5)$-like, *normal structure* of states couples to a γ-soft, $O(6)$-like, *intruder structure* [14, 15, 16, 17]. The *interacting boson model* (IBM), which treats the nucleus as a composition of bosons, due to the likeliness of nucleons to couple to pairs of integer spin, is a profound tool for the analysis of this coupling mechanism. Its three symmetry limits provide descriptions for key structures of nuclear configurations, i.e the $U(5)$ limit, the harmonic vibrator, the $SU(3)$ limit, a deformed but rigid rotor and the $O(6)$ limit, describing an asymmetric, γ-soft but rotational nucleus [8]. By analyzing the symmetry properties, a nucleus is placed between these three poles according to the parameters of the IBM-Hamiltonian. Yet the experimental knowledge about transition strengths was restricted mostly to the two-phonon levels.

Around 2010 the set of experimental information had grown, and information about transition strengths for states considered to be three-phonon candidates was available. Strong deviations from the vibrator picture were revealed, as can be

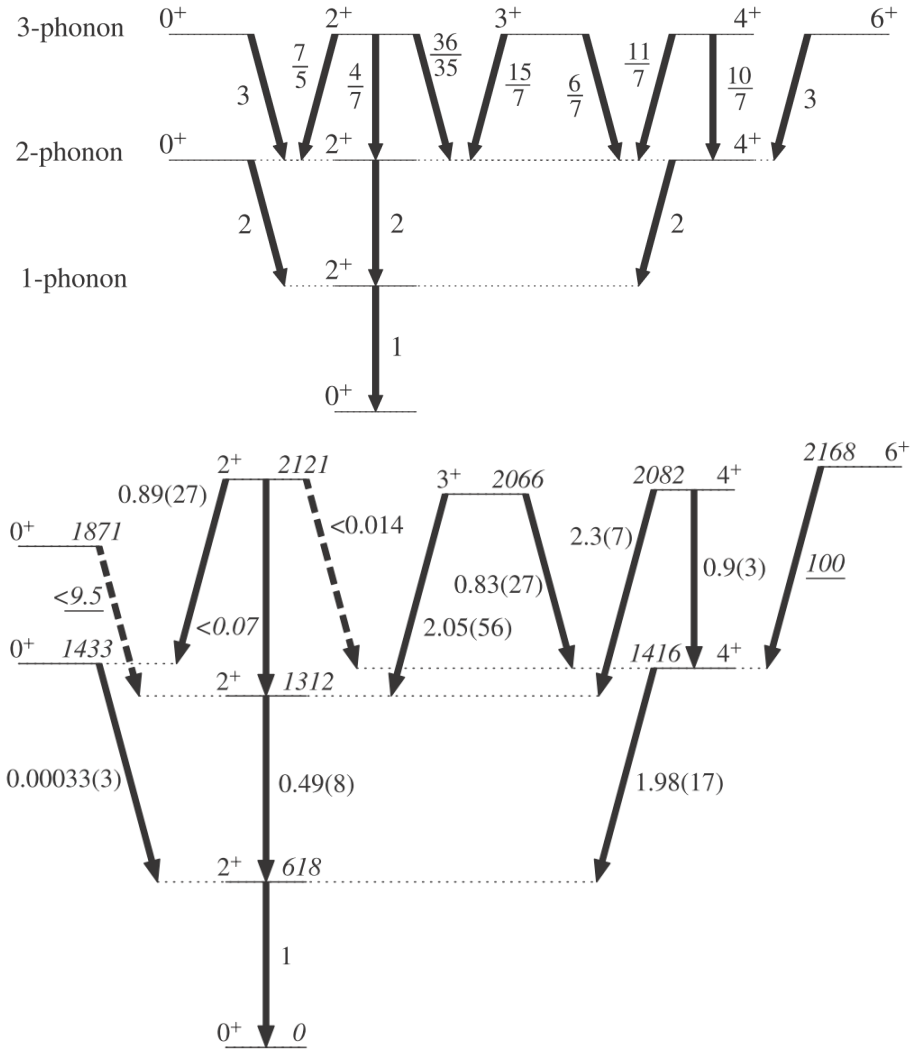

Figure 1.2: Top: The predicted level scheme including transition strengths relative to the $B(E2; 2_1^+ \rightarrow 0_1^+)$ transition. The summed transition strength of a n-phonon level is n times that of the 1-phonon transition.
Bottom: The experimental level scheme of ^{112}Cd with $B(E2)$ values normalized to the $B(E2; 2_1^+ \rightarrow 0_1^+)$ transition. Adopted Figures from [7].

seen by the relative transition strengths of ^{112}Cd [7], as shown in Figure 1.2. The picture of a vibrator configuration ($U(5)$), composed from so-called normal states, that couples with a γ-soft, rotational ($O(6)$) intruder structure was tested for higher-lying states. Garret et al. analyzed the decay patterns of $^{110-116}$Cd [18] (2008) up to the three phonon level. They stated a breakdown of the picture of a strong-mixing between the $U(5)$- and the intruder $O(6)$-structure for 0^+ states at the two phonon level for ^{116}Cd, which casts doubt on the appropriateness of the vibrational interpretation for any of the Cd isotopes. In a following work, Garret and Wood [7] (2010) even rejected the low-energy vibrational modes in the Cd isotopes. They ordered levels of $^{110-116}$Cd in band-like structures based on 0^+ states, resulting in an excitation pattern characteristic of quasi-rational bands. Additionally, newly discovered non-neglectable quadrupole moments gave rise to the assumption that

the cadmium nuclei are not spherical, contradicting the spherical vibrator picture [7]. Heyde and Wood picked up the discussion in a review about shape coexistence [19] (2011), underlining the difficulty in the interpretation of excited 0^+ states in the Cd isotopes. In a detailed spectroscopic analysis of ^{110}Cd Garrett et al. [20] (2012) tested the intruder mixing scenario. They concluded that the non-intruder states are not vibrational in ^{110}Cd, but the decay pattern is strongly suggestive of a γ-soft, or $O(6)$-type, nucleus.

Already in 2002, Gade et al. [21] stated that the nuclei $^{108-112}$Cd form a transitional path between a vibrational, $U(5)$ and a gamma-unstable $O(6)$ dynamical symmetry, although with decreasing neutron number. Meaning a $U(5)$ symmetry is stated at mid-shell. It is important to note, that this argumentation was founded solely on excitation energies of 0^+ states. And, as already mentioned, at that time the picture of a $U(5)$-like symmetry at the middle of the shell was well accepted. In that same work, the first observation of an intruder band in ^{108}Cd was published. Up to now, no intruder band is known in any lighter Cd nuclei.

This work contributes to the discussion, sketch above, by extending the focus from the middle of the shell to the neutron deficient side. The detailed spectroscopy of ^{106}Cd reveals many new results, i.e. γ-rays and levels, as well as branching ratios. Strong hints for an intruder band are found in ^{106}Cd. The shell model analysis in this work extends a former work [22]. The nuclear shape of $^{100-110}$Cd is analyzed with the method of rotational invariants. Higher order invariants are derived from the shell-model data for the first time, allowing a derivation of the softness parameters $\sigma(\beta)$ and $\sigma(\gamma)$. At the same time, a qualitative interpretation about the symmetry development, in terms of the IBM, is possible. Starting from shell-model calculations and deriving deformation parameters originating from the geometrical model, an additional approach is available, that serves as crosscheck on symmetry properties.

2 γ-transitions in nuclei

2.1 Transition strength

Excited nuclei obey the general decay law:

$$N = N_0 e^{-\lambda t}, \tag{2.1}$$

which describes the number of excitations N over time t starting from N_0 excitations. The decay constant λ is related to the mean lifetime τ via $\lambda = 1/\tau = \ln 2/t_{1/2}$. The half life $t_{1/2}$ is the time period after which half the number of initial excitations has decayed.

The constant λ can be determined by

$$\lambda(\sigma l, m) = \frac{8\pi(l+1)}{l\hbar(2l+1)!!}\left(\frac{\omega}{c}\right)^{2l+1} \left|\langle f\left|O(\sigma l, m)\right|i\rangle\right|^2. \tag{2.2}$$

Equation 2.2 describes the *transition probability* of a γ-decay. σ denotes the electric or magnetic character E or M and l is the multipole order or the angular momentum carried by the γ-ray. The difference in magnetic spin projection is $m = m_i - m_f$ between initial and final state. The energy of the γ-ray is related to ω and can be written as $E_\gamma = \hbar\omega$.

As Equation 2.2 gives the probability for a transition of one sub-state $m = m_i - m_f$ to another, the sum over all possible substates m and m_f provides the total transition strength, which determines the lifetime of the initial state. The matrix element in Equation 2.2 is therefore written as[23]:

$$B(\sigma l, j_i \to j_f) = \sum_{m,m_f} \left|\langle j_f m_f\left|O(\sigma l, m)\right|j_i m_i\rangle\right|^2. \tag{2.3}$$

The quantity $B(\sigma l, j_i \to j_f)$ is called the *reduced transition probability* or transition strength. Applying the Wigner-Eckart theorem, Equation 2.3 transforms to its well known form:

$$B(\sigma l, j_i \to j_f) = \frac{1}{2j_i+1}\left|\langle j_f \left\|O(\sigma l)\right\| j_i\rangle\right|^2. \tag{2.4}$$

Values of $B(\sigma l)$ are given in units of $e^2\mathrm{fm}^{2l}$ or $e^2\mathrm{b}^l$ for transitions with electric character and in $\mu_N^2\mathrm{fm}^{2l-2}$ or $\mu_N^2\mathrm{b}^{l-1}$ for magnetic transitions, with b (barn) = $10^{-28}\mathrm{m}^2$. It can be explicitly written [24]:

$$B(El)\downarrow = \frac{\ln 2 \cdot l[(2l+1)!!]^2\hbar}{8\pi(l+1)e^2\mathrm{b}^l}\left(\frac{\hbar c}{E_\gamma}\right)^{2l+1}\frac{1}{t_{1/2}(El)}, \tag{2.5}$$

$$B(Ml)\downarrow = \frac{\ln 2 \cdot l[(2l+1)!!]^2\hbar}{8\pi(l+1)\mu_N^2\mathrm{b}^{l-1}}\left(\frac{\hbar c}{E_\gamma}\right)^{2l+1}\frac{1}{t_{1/2}(Ml)}. \tag{2.6}$$

The downward arrow $\downarrow$ denotes transitions from an energetic higher level to a lower level, $t_{1/2}(\sigma l)$ is the half life related to the decay.

Single particle estimate The operator in the single-particle Equation 2.4 can explicitly be written. For electric transitions the equation forms to [25]:

$$B(El, j_i \to j_f) = \frac{1}{2j_i + 1} \left| \left\langle n_f l_f j_f \left\| r^l \mathbf{Y}_l \right\| n_i l_i j_i \right\rangle \right|^2 \left(\frac{\tilde{e}}{e} \right)^2 . \tag{2.7}$$

The transition operator $O(El)$ consists of a radial part r^l and the spherical harmonics $\mathbf{Y}_l$. The effective charge $\tilde{e}$ can have values differing from the elementary charge e. Nuclear states are denoted by the oscillator quantum number $n_{i,f}$, the orbital spin $l_{i,f}$ and the spin $j_{i,f}$ of the state. Accordingly, the operator of magnetic transitions $O(Ml)$ in Equation 2.4 writes as:

$$O(Ml) = \nabla(r^l \mathbf{Y}_l) \frac{1}{e} \times \left[\frac{1}{l+1} \frac{\widetilde{e}\hbar}{mc} \mathbf{l} + \widetilde{\mu} \mathbf{s} \right], \tag{2.8}$$

including the effective nuclear magnetic momentum $\widetilde{\mu}$. Under the assumptions of a box function for the radial integral $\langle r^l \rangle$ and $j_i = l + \frac{1}{2}$ and $j_f = \frac{1}{2}$ in Equations 2.7 and 2.8, the transition strength can be expressed as [25]:

$$B_{s.p.}(El) = \frac{1.2^{2l}}{4\pi} \cdot \left(\frac{3}{l+3} \right)^2 \cdot A^{2l/3} [e^2 \mathrm{fm}^{2l}] \tag{2.9}$$

for electric transitions. The magnetic single particle estimate is written as:

$$B_{s.p.}(Ml) = \frac{10}{\pi} (1.2)^{2l-2} \cdot \left(\frac{3}{l+3} \right)^2 \cdot A^{(2l-2)/3} [\mu_N^2 \mathrm{fm}^{2l-2}] \tag{2.10}$$

Since the $B_{s.p.}(\sigma l)$ values of Equations 2.9 and 2.10 depend only on the nuclear mass A and the multipole order l, a fixed estimate of the transitions strength originating from a single particle orbit change can be calculated for every nucleus and decay multipolarity.

It is convenient to give transition strength, i.e. $B(El)$- and $B(Ml)$-values, in units of Equations 2.9 and 2.10, in so-called *Weisskopf units* or W.u.. Depending on the structure of a nuclear state, transitions of several hundreds of W.u. can be observed, e.g. in strongly deformed rotational nuclei. Such strong transitions point to collective excitations, in which many nucleons contribute to form a state. The wave function of such states is an admixture of many single particle configurations with fractions of the mean occupation amplitude [25]. In contrast can a weak transition of $\sim$1 W.u. be classified to be of single particle character.

2.2 Branching ratios

By comparing both Equations 2.9 and 2.10, it is obvious that that for one and the same multipolarity the electric transitions are favored by two orders of magnitude relative to magnetic transitions. Complementary to the electromagnetic decay, a state can deexcite by the emission of a conversion electron. Some nuclei can go through complicated decay schemes involving even the emission of α-, β- and γ-radiation as competing decay modes. The relative intensity of each decay channel

is called *branching ratio* [26]. In this work only relative γ-ray intensities have been measured, with the strongest intensity set to 100%, i.e. the sum of relative intensities related to one level exceeds 100%.

Competing decay channels i offer an enhanced ability for a state to get deexcited. The half life of Equations 2.5 and 2.6 has to be corrected by [24]:

$$t_{1/2} = t_{1/2}(\sigma l) \cdot \frac{BR(\gamma_K)}{1 + \alpha_K}, \tag{2.11}$$

where $BR(\gamma_K)$ is the total branching ratio of one γ-ray transition channel K, including conversion electrons and α_K denotes the conversion coefficient. In case of a γ-transition with mixed multipolarity a factor of $1/(1+\delta^2)$ has to be added to the right hand side of Equation 2.11 in case of equal multipole order l or $\delta^2/(1+\delta^2)$ for $l+1$, where δ is the multipole mixing ratio.

3 (p, p') Experiment on ^{106}Cd

3.1 Motivation

In the work of A. Linnemann [27] (2005) several experiments on ^{106}Cd were conducted. Three experiments made use of the HORUS setup in Cologne (see Section 3.2.1) including the reactions: ^{104}Pd(α, $2n$)^{106}Cd, ^{105}Pd(^{3}He, $2n$)^{106}Cd and ^{106}Cd(p, n)^{106}In$\rightarrow^{106}$Cd. Additionally, an inelastic neutron scattering experiment was performed at the University of Kentucky. The Van de Graaff accelerator there was used to produce neutrons via a ^{3}H(p, n)^{3}He reaction with a lower energy limit of 2.6 MeV. Level lifetimes were extracted by the Doppler shift attenuation method (DSAM) from the inelastic scattering reaction (n, n')^{106}Cd. [27, 28].

The experiments of both setups did not yield the same results concerning certain newly discovered γ-rays and energy levels (commented on in Section 3.5). On top of that ^{106}Cd was found to posses some unresolved γ-ray doublets in the post-processing of the neutron scattering data [29]. Due to these inconsistencies in γ-ray associations to levels and uncertainties in the branching ratios, the results of the neutron scattering experiment have not been published in a journal until the time of writing this thesis [29]. Results of other works studying ^{106}Cd, that had been performed even before, could also not resolve these issues. In some cases, different results from literature are unclear or even contradict each other e.g. in stating branching ratios and γ-ray associations (see the discussion in Section 3.5).

The experiments by A. Linnemann [27] mentioned earlier were not equipped with particle detectors and lacked the ability to distinguish between level excitations coincident with the registered γ-rays. A work of Kumpulainen et al. [30] (1992), using a ^{106}Cd(p, p') reaction, includes particle and γ-ray detectors. The study focuses on level energies below 2.5MeV in the even isotopes $^{106-112,116}$Cd. Although the reaction and the ability to determine level excitations via the particle detectors are similar to this work, results of Kumpulainen et al. are not detailed enough to clarify some cases. For energies beyond 2.4 MeV, Ref. [30] can not be consulted. The SONIC [31] particle spectrometer, used in this work, is able to resolve excited levels. Together with the HORUS [27] spectrometer, level excitations and γ-rays can be detected in coincidence. The aim of this work therefore is to achieve a most accurate spectroscopic picture of ^{106}Cd and to solve the previously observed discrepancies.

3.2 The SONIC@HORUS setup at the FN-Tandem Accelerator Cologne

3.2.1 Experimental settings and detector setup

The FN tandem accelerator at the Institute for Nuclear Physics at the Cologne University is capable to establish an accelerating voltage of up to 10MV. A 7.5 MeV proton beam was provided with a mean current of 150mA. The calculated coulomb barrier lies at 7.7 MeV, as predicted by the code CASCADE[32]. The fusion-evaporation and inelastic-scattering reaction channels were calculated to be equally probable with $\sim$ 350 mb at 7.5 MeV. Other reaction channels are predicted to be in the neglectable range of $<$0.7mb. Two self-supporting ^{106}Cd targets were available with a thick-

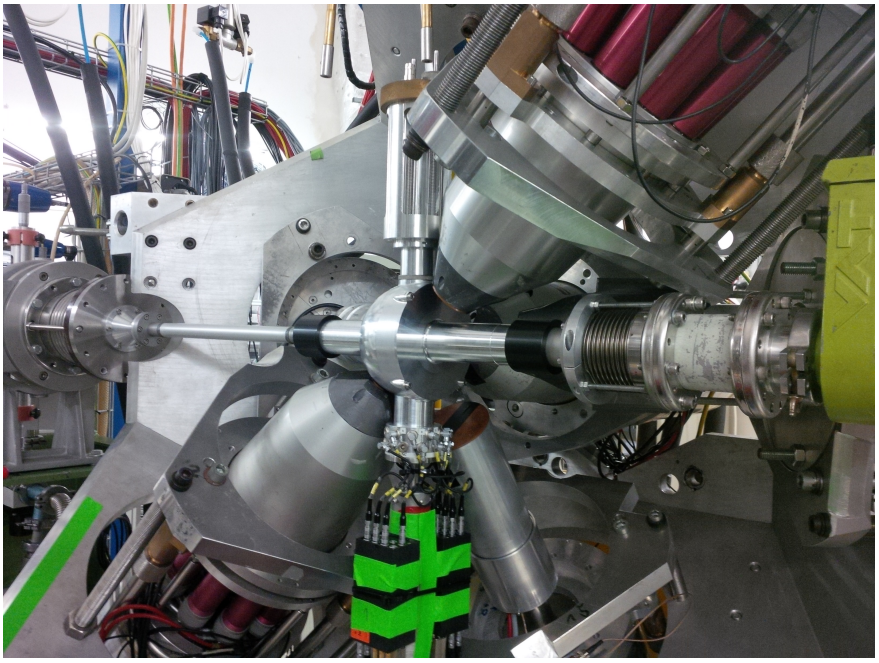

Figure 3.1: Picture of SONIC@HORUS. The setup is opened, only one hemisphere of HORUS is visible carrying half of the 14 HPGe detectors surrounding SONIC in the center. The beam line goes from the left background to the right foreground.

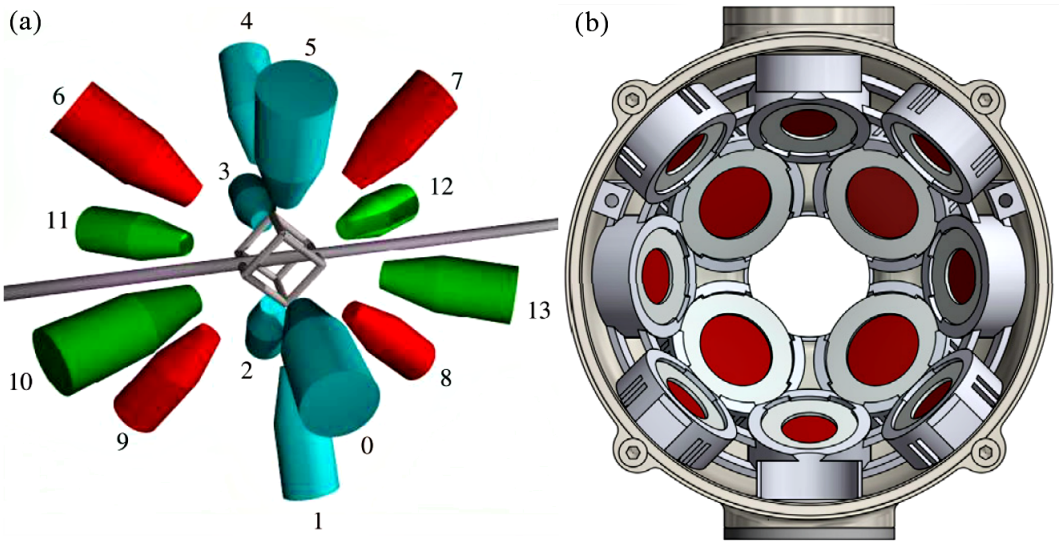

Figure 3.2: (a): Schematic drawing of HORUS hosting 14 HPGe detectors placed at the corners and planes of a cube. Figure taken from [27].
(b): Scheme of SONIC housing 12 Si detectors placed in 3 ring of 4 detectors each. Figure taken from [31].

ness of 0.9mg/cm^2 and 1.2mg/cm^2 and enrichments of above 70% and above 90% respectively. The experiment was performed in August 2016 and lasted 7 days. The targets were swapped in the middle of the beam time.

The γ-rays were registered with the HORUS [27] cube spectrometer (High efficiency Observatory for γ-Ray Unique Spectroscopy), equipped with 14 high purity Germanium (HPGe) detectors. Figure 3.2 (a) shows a scheme of HORUS. Six detectors are facing the planes of an imaginary cube and eight are pointing to the corners of the cube. Six of the detectors were equipped with BGO shields. A detailed description can be found in Ref. [27].

The SONIC [31] spectrometer (Silicon Identification Chamber) contains 12 Silicon detectors placed in 3 rings of 4 detectors each at backwards angles towards the beam line direction. The solid angle coverage in backwards direction is 9%. Figure 3.2 (b) shows a scheme of SONIC. The spectrometer houses the target frame in its center, so that back scattered particles are registered by the Si-detectors.

Figure 3.1 shows a picture of the whole setup. The opened HORUS spectrometer is shown. Only one hemisphere holding 7 HPGe detectors is visible. In the center of HORUS the closed SONIC spectrometer is placed, integrated in the beam line. The beam direction is from left to right.

3.2.2 Data acquisition and data processing

The detector signals are preamplified and processed by Digital Gamma Finder (DGF-4C) modules made by the company XIA LLC [33]. Each module has 4 input channels. Particle and γ-ray detector signals are digitized by the analog to digital converters (ADC) of the DGF modules. Each input channel is associated with a veto channel, which is used to directly reject a signal, if a corresponding BGO shield is attached and triggered. After the digitalization the amplitudes of detector signals correspond to uncalibrated channel numbers. Several DGF modules are synchronized by distributing the clock signal of a master module to the other modules. With this equipment, the data acquisition system (DAQ) is capable of rejecting signals if a required multiplicity of detector signals is not fulfilled. This way single events, that do not involve at least two detector signals necessary for $\gamma\gamma$- and $p\gamma$-coincidence experiments, can be ignored. The multiplicity requirement was set to two during the experiment of this work. A detailed description of the DAQ can be found in Ref. [34].

The listmode files written by the DAQ were processed offline by the code SOCOv2 [35]. A crucial step is setting a time window for coincident detector events. Additionally, a calibration can be handed to the code. Specific detector types can be set as event triggers. In this work, the particle detectors were set as trigger to ensure measured coincidences were stemming from a back scattered particle i.e. events most likely originating from the target material were processed and background noise was reduced. From these input settings, SOCOv2 sorts event files which are then processed in a second step to build two-dimensional matrices. For the analysis, $\gamma\gamma$-, $p\gamma$- and γp-matrices were build. By handing gate parameter for a specific detector type to the code, the process of building the matrices is restrained to events within the gate. An analysis of triple events is possible this way, although the first gate of the building process cannot be background corrected.

3.3 Calibration

3.3.1 Energy Calibration

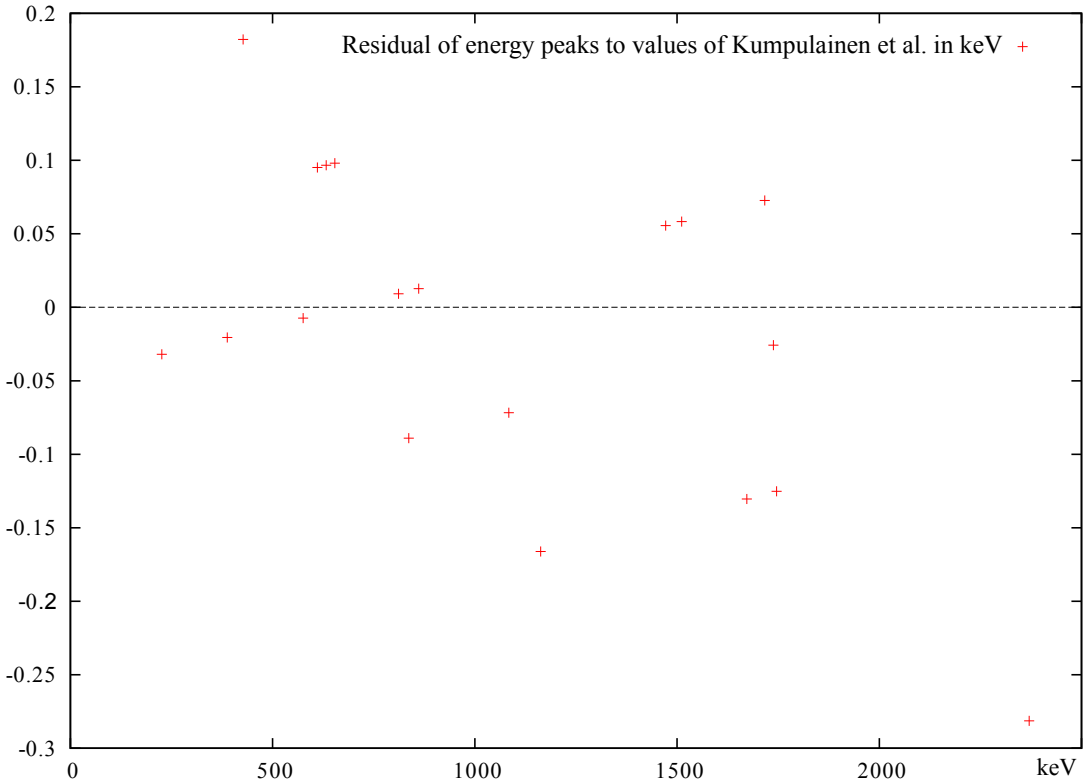

Figure 3.3: Residual of energy values of peaks used for linear calibration to energies given in the work of Kumpulainen et al. [30].

Ge-Detectors A proper calibration of an experimental setup is a vital task for the analysis of γ-ray spectra. A common procedure is the measurement of a calibration source with the used detector setup shortly before or after the conducted experiment. This way energy values can be assigned to the counting channels of the DAQ. In this work, a ^{226}Ra calibration source was used, which is an established standard for this task [36]. ^{226}Ra has a half life of 1600 years before going through an α-decay. It is the starting point of a chain of α- and β^--decays of significantly shorter lifetimes, so that a sufficient amount of γ-rays is provided from the daughter nuclei, spread over an energy range up to 3 MeV. Energy values of ^{226}Ra have been taken from [36], which also provides relative intensities for the decay chain, allowing an efficiency calibration of the detector setup.

A major problem in the calibration procedure, was a gain shifting in the detector electronics over the whole beam time. In such cases, peaks are not present in the same channels in each subrun, but rather shift their channel number, which results in wrong energies and broad peaks after the calibration. This problem can be taken into account by the SOCOv2 [35] sorting code, which provides tracking of peaks separately for each detector starting at a given channel number from subrun to subrun. The resulting shift polynomials from this step are processed during the sorting procedure and are combined with the calibration polynomials handed to the

code. Afterwards the energy peak of each subrun match with those of the previous subruns. Unfortunately, a gain shift also happened in the electronics during the time period between the experiment and the measurement of the calibration source. The conducted energy calibration with the ^{226}Ra source did thus not produce a satisfying assignment of energies to channels for the beam time. The spectra taken during the calibration were shifted about 2-10 keV compared to the spectra taken during the experiment. Therefore, the only detector with a nearly adequate calibration and a deviation to literature values of ^{106}Cd [1] of 0.2 keV - 0.5 keV has been taken as a reference. The quadratic calibration polynomials of the detectors had to be manually modified, so that each detector matches the peak pattern of the reference detector. That way it was possible to obtain a first calibration of the setup. Non-linear energy shifts could be handled by this procedure. To further improve the calibration, energy values have been taken from the work of Kumpulainen et al. [30] and a linear correction has been conducted. Figure 3.3 shows the residual of the final calibration to energy values given in Ref. [30]. The standard deviation of that residual gives an error of 0.09 keV, a value well below the energy uncertainty of 0.3 keV given in Ref. [30]. Therefore, an error of 0.3 keV for energy values has been adopted in this work. Note however that this second calibration was not handed to the sorting code SOCOv2, but was rather applied after the data analysis. Therefore, figures showing γ-spectra in this work may not display the resulting energies presented in Table 3.1.

It is emphasized that the deviation of energy values to the literature is starting to exceed the 0.3 keV energy uncertainty of this work from $\sim$2.3 MeV upwards. As one can see from Figure 3.3, the 2370 keV ground state transition reveals the beginning of this effect by an increasing deviation to the literature. Also, Table 3.1 displays some higher energetic ground state transitions, that do not match with the level energies. Thus, to get the most valid values, γ-rays beyond $\sim$2.3 MeV have not been taken into account in the calculation process of level energies.

Si-Detectors With the Ge-detectors calibrated, the Si-detectors can be calibrated from a pγ-matrix. By gating on γ-rays that can clearly be assigned to certain level energies, a single excitation can be observed in the p-spectra, which can in turn be associated to the level energy. The FWHM of peaks in the p-spectra is typically in the range of 180 keV (Figures 3.7 and 3.10 give an impression of the energy resolution.). After the calibration, peak centroids match with level energies in a range of $\pm$10 keV.

3.3.2 Efficiency Calibration

Germanium-detectors are not equally sensitive to γ-radiation of different energy. As the probability for Compton-scattering increases with energy, the probability for a γ-ray to deploy its full energy in the detector crystal decreases. It is also more likely for a γ-ray to pass through the crystal without interaction, i. e. the detector is less efficient to γ-radiation with increasing energy resulting in an under representation of higher energetic γ-rays in the count rates. Besides this *intrinsic* efficiency, γ-ray detection is also influenced by the geometry of the setup i. e. the coverage of solid angle by detector material, which is called the *geometric* efficiency of the setup. The

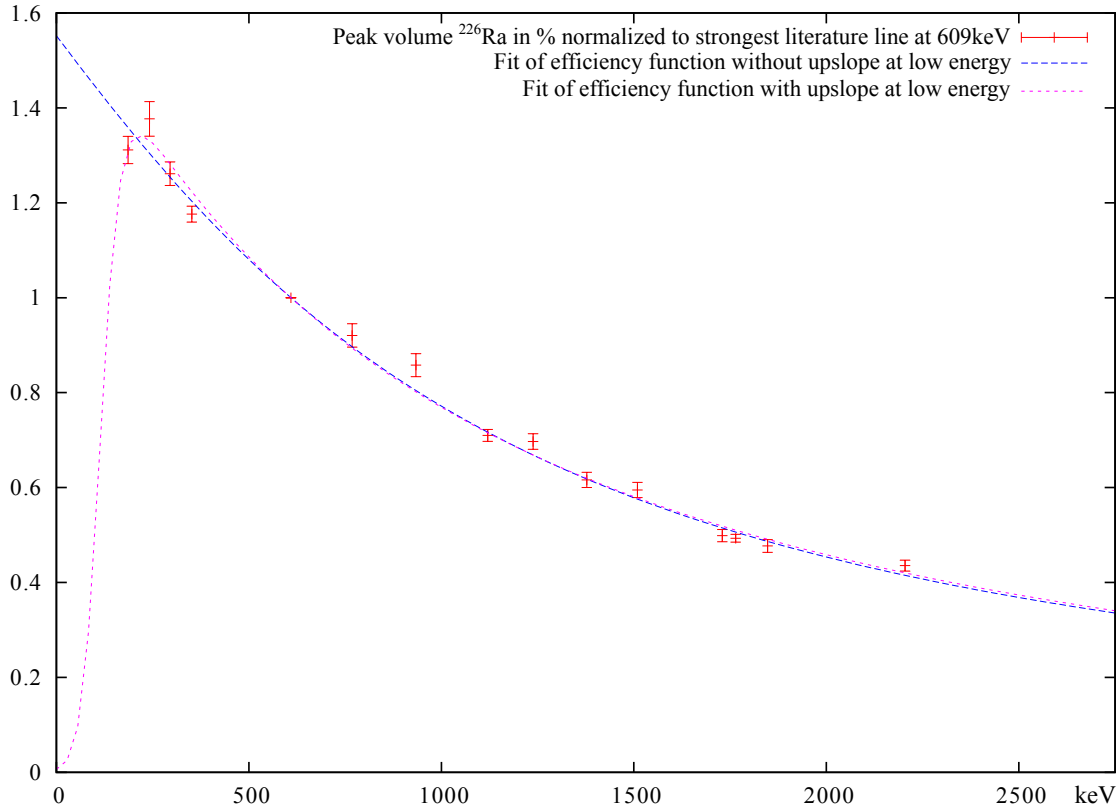

Figure 3.4: Fit of the detector efficiency function given in [37] to peak volumes of the ^{226}Ra calibration source with relative intensities $> 4\%$. The peak volumes have been normalized to the strongest γ-ray at 609 keV and to their relative intensity given in [36].

geometric efficiency strongly influences the overall count rate of γ-radiation. For the determination of branching ratios it is therefore crucial to determine the intrinsic efficiency of the setup.

The relative (intrinsic) efficiency ϵ_{rel} is determined by fitting a proper function to normalized peak volumes of the ^{226}Ra calibration source. Figure 3.4 shows peak volumes (red color) normalized to the strongest line of the source (at 609.3 keV) and at the same time to their relative intensity given in Ref. [36]:

$$\epsilon_{rel}(E_\gamma) = \frac{N(E_\gamma)}{I_{rel,lit} \cdot N(609\ \text{keV})}. \tag{3.1}$$

Efficiency functions from Refs. [37, 38] have been fitted to the data whereas best fit results were achieved with the function stemming from Ref. [37]:

$$\epsilon_{rel}(E_\gamma) = A \cdot \exp(-B \cdot \ln(E_\gamma - C + D \cdot \exp(-E \cdot E_\gamma))). \tag{3.2}$$

As can be seen from Figure 3.4, the expected upslope at low energy values could not clearly be reproduced by the fitting procedure due to the absence of data points in that region. The X-ray shielding added to the detector fronts during the experiment did not reduce the energy values in Figure 3.4 sufficiently. Different starting parameters for the fitting procedure of Equation 3.2 have produced the same outcome. The

blue curve in Figure 3.4 is the result of the fitting process with a reduced $\chi^2 = 1.67$. The residual of the data point at the lowest energy of 186 keV is normally distributed to the blue curve. However, this point could also indicate the maximum of Equation 3.2 if it was lying at the end of the up slope part. The purple curve displays an alternative perspective to the data points. This outcome has been produced by adding a constructed data point at $(0, 0)$. The fit has a $\chi^2 = 1.72$.

As the lowest γ-ray in this work has an energy of 163 keV and other γ-rays are close to the potential maximum of the purple curve at $\sim$220 keV, it is of interest to get an estimate of efficiency uncertainties under the assumption that the alternative fit might be valid. The artificial data point at $(0, 0)$ is not unjustified from a physical point of view, as a low detector efficiency can be expected at very low energy. If, hypothetically, additional X-ray shielding was placed in front of the detectors, the minimum detectable energy would rise. The constructed point of zero efficiency would shift to lower values, resulting in a y-intercept of the curve. Due to the energy dependence of the γ-ray cross section, higher energetic γ-rays would be less shifted resulting in a less steep upslope. The purple curve can thus be considered as an extreme case of steep upslope at low energies.

Intensities of γ-rays have thus been calculated from both curves during the analysis. The errors of the intensities of each curve include the error of the peak fit and the standard deviation of residuals coming from the fit of the efficiency function (1σ confidence level). The law of error propagation has been applied in this step. The curves serve as starting points for upper and lower error limits accordingly. The error of each of this two derived intensities is added or subtracted to the upper and lower value respectively, thereby expanding interval between these error limits. Values for relative intensities of Table 3.1 have been calculated from the arithmetic mean of these upper and lower limits.

3.4 General data analysis methods

From the coincident measurements $\gamma\gamma$-, pγ- and γp-matrices were build. As a general approach to obtain γ-ray energies, a gate was set from below in a $\gamma\gamma$-matrix, i.e, the gate was set on a transition depopulating levels fed by the transition of interest. This yields γ-peak free of contaminating components, that can easily be fitted. Level energies have been derived by summing γ-ray energies of cascades leading to the corresponding final levels, though γ-rays beyond $\sim$2.3 MeV have not been used in the sum, as discussed above. Newly discovered γ-rays have been crosschecked by gating on them in a γp-matrix to derive the corresponding level energy. In return, by setting a p-gate to this level energy a coherent spectrum of transitions belonging to the γ-cascade had to be observed. Figure 3.5 gives an impression of this procedure, when gating in a pγ- or γp-matrix. E.g. a γ-gate set to the 861 keV $4_1 \rightarrow 2_1$ transition in a γp-matrix results in a 1494 keV peak in the p-projection, vise versa gating on the energy of the 4_1 state in a pγ-matrix gives a γ-spectrum containing merely the 861 keV and 633 keV peaks. Some complicated combinations of γ-multiplets made it necessary to build triple events or cubes, further on denoted as p-gated $\gamma\gamma$-matrices or p$\gamma\gamma$-matrices. For the extraction of branching ratios, a p-gate was set to the level energy in a pγ-matrix. The peak of interest was fitted

in the resulting γ-projection. In case of a multiplet peak, the γ-ray energies of all components were determined before and set to fixed values in the fitting procedure. In the following Section 3.5, paragraphs corresponding to level energies describe each new finding and in some cases even more complicated approaches that were made to obtain the shown results.

3.5 Experimental Results

As no $\gamma\gamma$-angular correlation was part of the analysis, literature [1] spin assignments have been adopted in this work. Spin ranges have been assigned to newly discovered levels according to the selection rules of the deexciting γ-transitions related to the spin of the final levels. Thereby, it was assumed, that these γ-rays have preferably an $E2$- or $M1$-multipolarity. Parity changing $E1$-multipolarity transitions are assumed to be possible, but present to lesser extend and only at higher energies, due to the fact, that the negative parity orbital $h^{-}_{11/2}$ has the highest energy within the 50-82 N shell among the single particle orbitals (see Figure 4.1). The same assumption was applied, when ranges of literature spin values have been constricted by classifying newly discovered transitions. Note that, although a $\gamma\gamma$-angular correlation analysis was conducted, only spin ranges were suggested in Ref. [27] instead of concrete spins for many newly discovered levels. It seems, that the same assumptions concerning transition multipolarities, applied in this work, have also been applied in Ref. [27] for the confirmed levels in Table 3.1. In some cases spins different to the literature [1] were derived in Ref. [27], which are discussed shortly in the corresponding level section.

Note that the discussion in this section excludes findings, especially spin assignments coming from a new analysis of the (n, n')-data [28]. These findings are referred to in Section 4.1, where experimental data is compared to the shell model.

In Figure 3.5 total projections of the $\gamma\gamma$- and pγ-coincident data are shown. Some low energetic levels and associated γ-rays are marked in the p- and γ-spectrum respectively. In Appendix A Table A.1 provides results of this work ordered by γ-ray energy. Together with the γ-spectrum of Figure 3.5 an impression about the density of peaks in the γ-spectrum can be gained, which makes the analysis challenging and tedious.

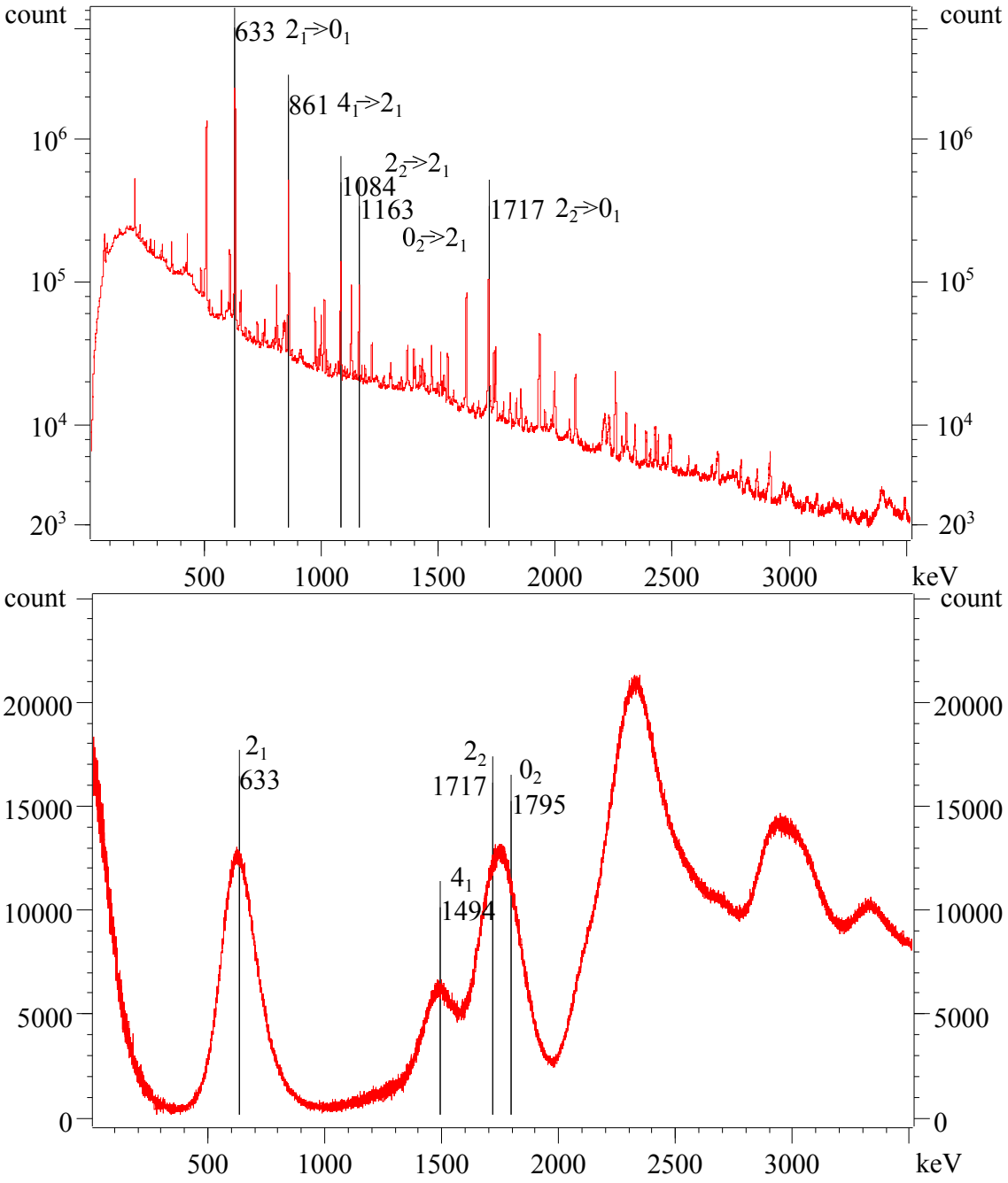

Figure 3.5: Top: Total projection of the $\gamma\gamma$-coincidence data of ^{106}Cd displayed at a logarithmic scale.
Bottom: Total projection of the pγ-coincidence data of ^{106}Cd.

Table 3.1: Results of the $(p, p'\gamma)$-experiment. Energy uncertainties are 0.3 keV. Values marked with ^{C} are confirmed results from experiments conducted in [27], which have been published there for the first time, but can not be found in the literature [1]. ^{N} marked results found newly in this work and are not published elsewhere. Values that differ from the literature [1] are marked with ^{D}.

E_{Level} [keV]	J_i^π [$\hbar$]	E_γ [keV]	I [%]	E_f [keV]	J_f^π [$\hbar$]	Comments & NNDC val. [1]
632.7	2^+	632.7	100	0.0	0^+	
1493.9	4^+	861.2	100	632.7	2^+	
1716.6	2^+	1083.9	100.0(41)^{D}	632.7	2^+	$I_\gamma = 80(20)$
		1716.7	68.6(31)^{D}	0.0	0^+	$I_\gamma = 100(15)$
1795.2	0^+	1162.5	100	632.7	2^+	
2104.7	4^+	388.0	3.12(20)	1716.6	2^+	
		610.8	100.0(41)	1493.9	4^+	
		1472.1	51.2(22)	632.7	2^+	
2144.1	0^+	427.4	37.6(16)	1716.6	2^+	
		1511.5	100.0(41)	632.7	2^+	
2252.3	(4^+)	535.9^{C}	7.7(11)	1716.6	2^+	
		757.8	10.6(11)	1493.9	4^+	
		1620.0	100(5)	632.7	2^+	
2254.1	$(2^+, 3^+)$	1621.4	100.0(42)	632.7	2^+	
2305.1	4^+	811.2	100.0(41)	1493.9	4^+	
		1672.5	10.90(53)	632.7	2^+	
2330.6	5^+	225.9	100.0(42)	2104.7	4^+	
		836.7	37.9(20)	1493.9	4^+	
2347.9	$(2)^+$	1715.2	100	632.7	2^+	
2370.5	2^+	575.3	33.5(15)	1795.2	0^+	
		653.9	33.2(15)	1716.6	2^+	
		1738.0	100.0(41)	632.7	2^+	
		2370.3	4.15(22)	0.0	0^+	
2378.6	3^-	1745.9	100	632.7	2^+	
2468.3	$(4)^+$	163.2^{N}	2.56(29)	2305.1	4^+	
		214.1^{N}	5.53(29)	2254.1	$(2^+,3^+)$	
		751.7^{C}	20.35(83)	1716.6	2^+	
		974.5	100.0(41)	1493.9	4^+	
		1835.8^{N}	24.8(12)	632.7	2^+	
2486.1	$2^+ - 4^+$	381.4^{N}	4.23(33)	2104.7	4^+	
		769.4^{C}	14.52(78)	1716.6	2^+	
		992.2	39.2(19)^{D}	1493.9	4^+	$I_\gamma = 100(30)$
		1853.5	100.0(42)^{D}	632.7	2^+	$I_\gamma = 95(9)$
2491.7	6^+	997.8	100	1493.9	4^+	
2503.4	6^+	1009.5	100	1493.9	4^+	
2561.6	0^+	1928.9	100	632.7	2^+	
2566.3	2^+	771.4^{C}	0.24(7)	1795.2	0^+	
		849.3^{C}	0.79(7)	1716.6	2^+	
		1933.6	100.0(41)	632.7	2^+	

E_{Level} [keV]	J_i^π [$\hbar$]	E_γ [keV]	I [%]	E_f [keV]	J_f^π [$\hbar$]	Comments & NNDC val. [1]
2629.3	5^-	298.7	5.91(76)	2330.6	5^+	
		524.6	100.0(43)	2104.7	4^+	
		1135.4	23.8(12)	1493.9	4^+	
2630.1	2^+	485.6^C	0.46(8)	2144.1	0^+	
		835.2^N	0.54(8)	1795.2	0^+	
		913.4^C	8.94(45)	1716.6	2^+	
		1997.4	100.0(41)	632.7	2^+	
		2629.5	7.01(33)	0.0	0^+	
2710.8^C	$2-6$	1216.9^C	100	1493.9	4^+	
2717.6	2^+, 3	339.2^C	5.4(16)	2378.6	3^-	
		1000.8^C	17.8(53)	1716.6	2^+	
		2084.9	100(40)	632.7	2^+	
2719.4	1, 2^{+D}	2086.7	100(18)	632.7	2^+	$J_i^\pi = 1, 2^+, 3$
		2719.3^C	5.91(79)	0.0	0^+	
2792.5^C	$2-6$	487.3^C	15.58(84)	2305.1	4^+	
		687.8^C	3.83(33)	2104.7	4^+	
		1298.7^C	100.0(42)	1493.9	4^+	
2800.6^C	$2-6$	495.5^C	53.2(29)	2305.1	4^+	
		548.1^C	23.6(18)	2252.3	(4^+)	
		696.0^C	100.0(46)	2104.7	4^+	
		1306.8^C	33.3(24)	1493.9	4^+	
2824.6	1	1029.3^N	5.19(35)	1795.2	0^+	
		2191.1^N	2.87(32)	632.7	2^+	
		2823.4	100.0(42)	0.0	0^+	
2889.3	1, 2^D	518.5^C	1.26(11)	2370.5	2^+	$J_i^\pi = 2, 3^+$
		541.6^C	1.07(11)	2347.9	$(2)^+$	Hints for level
		1094.2^C	3.10(19)	1795.2	0^+	doublet $J_i^+ = 1$
		1172.7^C	1.90(13)	1716.6	2^+	in [27]
		2256.4	100.0(41)	632.7	2^+	
		2888.2^C	12.48(55)	0.0	0^+	
2895.7^C	$2-6$	791.1^N	6.34(50)	2104.7	4^+	
		1401.8^C	100.0(44)	1493.9	4^+	
2914.9^N	$0-4$	2282.2^N	100	632.7	2^+	
2917.7	1	1122.3^C	8.63(58)	1795.2	0^+	
		1201.1^C	9.91(62)	1716.6	2^+	
		2285.4	19.3(10)	632.7	2^+	
		2916.3	100.0(43)	0.0	0^+	
2920.6	5^-	1426.7	100	1493.9	4^+	
2924.6	6^+	432.9	100	2491.7	6^+	
2926.7^N	$2-4$	822.1^N	43.5(20)	2104.7	4^+	
		1210.2^N	9.19(54)	1716.6	2^+	
		1433.0^N	100.0(43)	1493.9	4^+	
		2293.6^N	15.47(95)	632.7	2^+	
2936.2	2^+, 3^+	631.1^N	4.22(89)	2305.1	4^+	

E_{Level} [keV]	J_i^π [$\hbar$]	E_γ [keV]	I [%]	E_f [keV]	J_f^π [$\hbar$]	Comments & NNDC val. [1]
		831.1[N]	7.66(49)	2104.7	4^+	
		1219.5[N]	1.75(36)	1716.6	2^+	
		1442.7[C]	41.2(20)	1493.9	4^+	
		2303.4	100.0(43)	632.7	2^+	
2973.3	2^{D}	1178.0	5.32(34)	1795.2	0^+	$J_i^\pi = 2, 3^+, 4^+$
		2340.3	100.0(42)	632.7	2^+	
3012.6[N]	$2-4$	1518.5[N]	100.0(45)	1493.9	4^+	
		2380.2[N]	23.1(19)	632.7	2^+	
3018.8	3^+, $(5)^+$	640.7[C]	11.74(67)	2378.6	3^-	
		687.9[N]	7.39(46)	2330.6	5^+	
		713.6[N]	4.51(38)	2305.1	4^+	
		766.4[C]	17.43(90)	2252.3	(4^+)	
		1525.0	100.0(43)	1493.9	4^+	
3020.5	2, 3^+	1303.8[N]	8.09(48)	1716.6	2^+	
		2387.5	100.0(42)	632.7	2^+	
3044.2	8^+	541.0	74(18)	2503.4	6^+	
		552.3	100(22)	2491.7	6^+	
3059.5	3	1565.6	38.5(19)	1493.9	4^+	
		2426.7	100.0(44)	632.7	2^+	
3061.2[C]	(1), 2	593.5 [N]	9.05(98)	2468.3	$(4)^+$	
		1344.7[N]	26.3(15)	1716.6	2^+	
		2428.8[C]	100.0(49)	632.7	2^+	
		3060.8[N]	27.3(14)	0.0	0^+	
3073.0	2^{D}	694.2[C]	6.17(40)	2378.6	3^-	$J_i^\pi = 2, 3^+, 4$
		819.1[N]	10.87(63)	2254.1	$(2^+,3^+)$	
		2439.6	100.0(43)	632.7	2^+	
		3071.8[N]	4.39(32)	0.0	0^+	
3084.3	7^+	592.6	100	2491.7	6^+	
3093.0	(2^+)	787.9[N]	20.0(19)	2305.1	4^+	
		1376.3	78.5(48)[D]	1716.6	2^+	$I_\gamma = 100(13)$
		1599.1	71.2(43)[D]	1493.9	4^+	$I_\gamma = 35(5)$
		2459.9	100.0(53)[D]	632.7	2^+	$I_\gamma = 75(5)$
3119.4[C D]	1^{D}	553.0[C]	2.30(35)	2566.3	2^+	Level doublet
		558.0[C]	9.26(64)	2561.6	0^+	[39] questioned:
		748.6[C]	15.7(14)	2370.5	2^+	$J_i^\pi = 2^+, 3^+, 4^+$
		1324.0[C]	3.47(51)	1795.2	0^+	and $J_i^\pi = 1$
		1402.9	20.7(12)[D]	1716.6	2^+	$I_\gamma = 100(13)$
		2486.3	100.0(45)[D]	632.7	2^+	$I_\gamma = 64(9)$
		3118.0	54.3(25)[D]	0.0	0^+	$I_\gamma = 100(9)$
3126.4[N]	$1-4$	747.8[N]	4.22(12)	2378.6	3^-	
		2493.2[N]	100.0(66)	632.7	2^+	
3127.6	7^+	624.2	100	2503.4	6^+	
3132.3[N]	$4-7$	640.6[N]	100.0(47)	2491.7	6^+	
		801.6[N]	58.5(35)	2330.6	5^+	

E_{Level} [keV]	J_i^π [$\hbar$]	E_γ [keV]	I [%]	E_f [keV]	J_f^π [$\hbar$]	Comments & NNDC val. [1]
3198.1[N]	2 − 6	1704.2[N]	100	1493.9	4^+	
3214.3[N]	1 − 4	835.7[N]	21.1(13)	2378.6	3^-	
		1497.7[N]	100.0(43)	1716.6	2^+	
3222.4	1	1427.3[C]	7.8(43)	1795.2	0^+	
		2589.6[C]	19.4(11)	632.7	2^+	
		3220.2	100.0(44)	0.0	0^+	
3235.3	2, 3^+	1518.7	17.0(12)[D]	1716.6	2^+	$I_\gamma = 100(13)$
		2601.8	100.0(46)[D]	632.7	2^+	$I_\gamma = 19(4)$
3245.5	(2^+)	992.8[N]	100.0(58)	2252.3	(4^+)	
		1141.1	13.2(15)[D]	2104.7	4^+	$I_\gamma = 63(12)$
		1528.8	68.9(41)	1716.6	2^+	
		3244.0	93.9(63)	0.0	0^+	
3283.6	4 − 8[D]	780.2	100	2503.4	6^+	$J_i^\pi = ^+$ only
3285.5[N]	1 − 4	567.7[N]	47.7(29)	2717.6	2^+,3	
		907.2[N]	100.0(50)	2378.6	3^-	
3320.4	6^-	691.2	100(13)	2629.3	5^-	
		828.6	41.4(77)	2491.7	6^+	
3323.0	2^+, 3[D]	604.9[N]	6.08(87)	2717.6	2^+,3	$J_i^\pi = 1^+, 2^+, 3$
		1829.6[N]	14.3(18)	1493.9	4^+	
		2689.0	100(15)	632.7	2^+	
3328.2	2^+[D]	438.8[N]	7.16(86)	2889.3	2,3^+	$J_i^\pi = 1, 2^+$
		766.8[N]	10.4(12)	2561.6	0^+	
		859.7[N]	67.5(71)	2468.3	$(4)^+$	
		980.5	56.0(59)	2347.9	$(2)^+$	
		1074.3[N]	28.4(29)	2254.1	$(2^+,3^+)$	
		1833.8[N]	62.3(70)	1493.9	4^+	
		2694.9	100(12)	632.7	2^+	
		3326.9	19.3(19)[D]	0.0	0^+	$I_\gamma = 50(9)$
3333.2[N]	2 − 6	1027.9[N]	46.6(57)	2305.1	4^+	
		1839.4[N]	100.0(66)	1493.9	4^+	
3357.5	3 − 7	1026.9	100	2330.6	5^+	
3366.5	8^+	874.8	100	2491.7	6^+	
3371.9[N]	1 − 4	482.4[N]	73.8(50)	2889.3	2,3^+	
		654.1[N]	82.8(88)	2717.6	2^+,3	
		1024.3[N]	100.0(65)	2347.9	$(2)^+$	
3392.6	1, 2^+[D]	1676.0[C]	30.9(21)	1716.6	2^+	$J_i^\pi = 2^+$
		2757.9[C]	60.1(30)	632.7	2^+	$J_i^\pi = 1$ Adopt.
		3391.4	100.0(48)	0.0	0^+	from [27]
3427.8	2, 3^+ ,4^+	1933.9[N]	43.6(59)	1493.9	4^+	
		2793.2	100.0(44)	632.7	2^+	
3461.2	(6^-)	831.9	100	2629.3	5^-	
3483.2[N]	2 − 4	1112.7[N]	100.0(45)	2370.5	2+	
		1989.3[N]	31.8(20)	1493.9	4^+	
3489.4[N]	2 − 4	771.7[N]	32.6(22)	2717.6	2^+,3	

E_{Level} [keV]	J_i^π [$\hbar$]	E_γ [keV]	I [%]	E_f [keV]	J_f^π [$\hbar$]	Comments & NNDC val. [1]
		1995.6[N]	100.0(51)	1493.9	4^+	
3495.6	1, 2^+	929.2[C]	8.0(10)	2566.3	2^+	
		1148.0[C]	63.4(39)	2347.9	$(2)^+$	
		1243.3[N]	65.5(40)	2252.3	(4^+)	
		1778.7[C]	57.3(35)	1716.6	2^+	
		2861.2	100.0(51)	632.7	2^+	
		3492.1	87.9(45)	0.0	0^+	
3497.5[N]	$2-6$	2003.6[N]	100	1493.9	4^+	
3539.1[N]	$0-4$	908.8[N]	100.0(81)	2630.1	2^+	
		1822.6[N]	74.3(66)	1716.6	2^+	
3547.3	$3-7$[D]	1216.7	100	2330.6	5^+	$J_i^\pi = ^+$ only
3725.2[N]	$0-4$	1377.1[N]	100	2347.9	$(2)^+$	
3829.8[N]	$2-6$	1577.5[N]	100	2252.3	(4^+)	
3916.5[N]	$1-5$	1538.0[N]	100	2378.6	3^-	
4000.7[N]	$1-4$	1746.6[N]	100	2254.1	$(2^+,3^+)$	
4045.6[N]	$1-5$	1667.1[N]	100	2378.6	3^-	
4075.2[N]	$1-4$	1821.1[N]	100	2254.1	$(2^+,3^+)$	

The 1717 keV Level The branching ratio found for this state differs to the literature. In [1] (NNDC) the relative intensities for the depopulating γ-rays 1084 keV : 1717 keV are stated as 80(20) % : 100(15) %. This result is covered by the Coulomb excitation experiments in [40] with a branching ratio of 70(9) % : 100 % and the study of the ^{106}In $\rightarrow^{106}$ Cd β-decay in [41], where the ratio is 70(7) % : 100(10) %. Ref. [42, 43] state the 1717 keV γ-ray to be even more intense, with branching ratios of 16(4) % : 100(6) % and 17(1) % : 100(5) %, respectively. Other works have seen the two γ-rays nearly equally strong. From the (n,n')-data of [39] the result 100(13) % : 98(13) % was derived. In [30] a (p,p')-reaction as well as a ^{107}Ag$(p,2n)^{106}$Cd reaction where used to determine a branching of 100(15) % : 85(13) % and 91(14) % : 100(15) % respectively. γ-gated proton spectra have been used to confirm branching rations in that work (see also Figure 3.10 for the 1715/1717 keV gated proton spectra from [30]). From the β-decay examination of ^{106}In$\rightarrow^{106}$Cd [44] intensities were found to be 94(10) % : 100(10) %. In contrast to these findings some works found this level to be stronger depopulated by the 1084 keV γ-ray. From the (n,n')-experiment of [27] for the γ-rays 1084 keV : 1717 keV a ratio of 100(23) : 87.3(23) was derived. Ref. [45] states a γ-branching of 100(21) : 60(21). High energy heavy-ion (xn) reactions have been used in that work.

In this work relative intensities for the γ-rays 1084 keV : 1717 keV are found to be 100.0(41) % : 68.6(31) %. This result was determined by a p-gated γ-spectrum set to the 1717 keV level energy. The proton energy gate width of 100 keV was sufficient to avoid a contamination from the 1715 keV γ-doublet component from the 2348 keV level. The existence of the 1715/1717 keV doublet can explain an overestimation of the 1717 keV γ-ray in the ratios of other works, as e.g. in the single spectra in this work the intensities of the peaks 1084 keV : 1715/1717 keV (doublet) give the false ratio of 59.1(27) % : 100.0(41) %. However, the agreement between the branching

ratio derived here and the one from [45] is reasonable, if one considers, that in fusion evaporation reactions Yrast-states are preferably populated. Therefore the (2^+_{3-4})-state at 2348 keV is not observed in Ref. [45], which results in a 1717 keV peak, that is assumable free of doublet contamination from higher levels. The results of Ref. [30] differ to this work. The discrepancy is however moderate when focusing on the (p, p')-results therein alone, even though the results could not be confirmed within the error limits. As one can see from Figure 3.10 the 1715/1717 keV γ-doublet components could be separated in [30], which makes the (p, p')-results of that work the more valid values compared to the outcome of the ^{107}Ag$(p, 2n)^{106}$Cd reaction therein.

The 2252 keV & 2254 keV Levels In the experiments already mentioned about ^{106}Cd [27] the 536 keV γ-ray was assigned to the 2252 keV level, contradictory to the literature (NNDC) [1].

As there were no feeders known to these levels, the first attempt to solve this situation was to compare the cross sections of the two levels at 2252 keV and 2254 keV, respectively the number of counted γ-rays. Therefore it was made use of the information coming from the three particle detector rings of the SONIC setup with backward angles at 107°, 123°, 145° [31]. Back scattered particles, that are detected under a larger backwards angle have the ability to transfer a higher amount of angular momentum to the target, than back scattered events detected under a smaller angle. Since the 2252 keV level has a spin assignment of 4^+ and the 2254 keV level spin 2^+, 3^+, different values in the ratio of counts, e.g. counts$(E_{536\,\mathrm{keV}})$/counts$(E_{759\,\mathrm{keV}})$, are expected, when separate $\gamma\gamma$-matrices are build from back scattered events from each particle detector ring. The same characteristic in the ratios should be observed for the counts$(E_{536\,\mathrm{keV}})$/counts$(E_{759\,\mathrm{keV}})$ ratio and for the counts$(E_{1621\,\mathrm{keV}})$/counts$(E_{1620\,\mathrm{keV}})$ ratio over the three rings, if the 758 keV and 1620 keV γ-ray depopulate the 2252 keV level and the 536 keV and 1621 keV γ-ray depopulate the 2254 keV level, as stated in the literature. For direct reactions the angle of the main maximum of the back scattered particle distribution can be calculated from [46, (eq 7.78)]: $\cos\vartheta = [(k_p^2 + k_{p'}^2) - l(l+1)/R^2_{^{106}Cd}](2k_p k_{p'})$. (For this formula it is presumed, that the target nucleus is heavy enough compared to the projectile, that lab- and CM-system are practical the same. An assumption well applicable for this experiment.) The back scattering maxima are expected at 44.9° for 2^+-states, 66.4° for 3^+-states and 90.5° for 4^+-states. A 100 keV wide particle gate (p-gate) was set to 2253 keV for each event matrix of the rings. Since the γ-rays at 1620.1 keV and 1621.5 keV form a doublet, the energies have been fixed to literature values in the peak fitting procedure. The results in Figure 3.6 reveal a quite constant behavior in the ratio counts$(E_{536\,\mathrm{keV}})$/counts$(E_{759\,\mathrm{keV}})$ within the error bars. Indicating the two γ-rays have a constant branching ratio and thus stem from the same state. Whereas the increased count rate of $E_\gamma = 1621$ keV compared to $E_\gamma = 1620$ keV in ring 1 indicates both γ-rays have origins in different states.

However, these results are not satisfying, as the quotient counts$(E_{1621\,\mathrm{keV}})$/counts $(E_{1620\,\mathrm{keV}})$ of ring 1 is contradictory to the initial considerations involving the maximum angle of back scattering for certain level spins. It is thus more likely, that the increased count rate of $E_\gamma = 1621$ keV in Ring 1, according to a spin (2+, 3+) level,

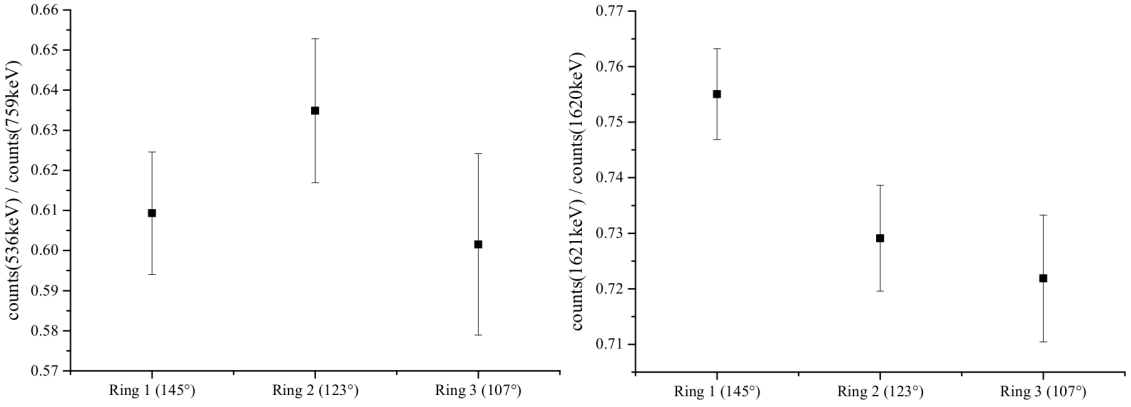

Figure 3.6: Ratio $counts(E_{536\,keV})/counts(E_{759\,keV})$ (left hand side) and $counts(E_{1621\,keV})/counts(E_{1620\,keV})$ (right hand side) for the three particle detector rings of SONIC. A 100 keV wide p-gate was set at 2253 keV.

could as well result from a maximum of second or higher order in the back scattered particle distribution. On top of that only the weak overlap of the error bars allow the assumption of a constant behavior in the ratio counts($E_{536\,\mathrm{keV}}$)/counts($E_{759\,\mathrm{keV}}$). Therefore an intensive search for unknown feeders to the 2252 keV and 2254 keV levels has been conducted to resolve the situation.

For the 2252 keV level five feeding transitions 2800 keV $\overset{548\,\mathrm{keV}}{\rightarrow}$ 2252 keV, 3019 keV $\overset{766\,\mathrm{keV}}{\rightarrow}$ 2252 keV, 3246 keV $\overset{993\,\mathrm{keV}}{\rightarrow}$ 2252 keV, 3496 keV $\overset{1243\,\mathrm{keV}}{\rightarrow}$ 2252 keV, 3830 keV $\overset{1578\,\mathrm{keV}}{\rightarrow}$ 2252 keV could be identified. These transitions are determined for the first time, except the first two of these feeders, which were already (but solely) found in the HORUS experiments [27] and could thereby be confirmed. Although the statistics resulting from the gate on each feeder were to weak to make a clear assignment for the 536 keV line, it was possible to associate the 536 keV line to the 2252 keV level via adding up the spectra without setting an additional particle gate. The extracted level branching ratios are given in Table 3.1.

For the 2254 keV level another five feeders where found, all of which were unknown before: 2468 keV $\overset{214\,\mathrm{keV}}{\rightarrow}$ 2254 keV, 3073 keV $\overset{819\,\mathrm{keV}}{\rightarrow}$ 2254 keV, 3328 keV $\overset{1074\,\mathrm{keV}}{\rightarrow}$ 2254 keV, 4001 keV $\overset{1747\,\mathrm{keV}}{\rightarrow}$ 2254 keV, 4075 keV $\overset{1821\,\mathrm{keV}}{\rightarrow}$ 2254 keV. Again the gated spectra of these feeders were summed up, showing no 536 keV line.

The 2331 keV Level The 837 keV transition of this level has not been seen in the $(n, n'\gamma)$-experiment in Ref. [27]. Making use of a p$\gamma\gamma$-matrix and setting a particle gate to the newly discovered 3132 keV feeder level and a γ-ray gate to the feeding 802 keV γ-ray, the 837 keV transition could clearly be assigned to depopulate the 2331 keV Level. Besides the known feeding transitions two new feeders have been identified, which can be found in Table 3.1.

The 2339 keV Level, given in the literature The conclusion of this work is, that this level does not exist. A γ-gate from below set to the 861 keV transition (belonging to the 1494 keV level), did not show the 845 keV line. Although this γ-ray exists in the singles spectra, after gating on the 845 keV peak in a γp-matrix, the

particle spectrum shows a flat line with no level excitations. This is a clear indication, that this γ-ray stems not from the target material and thus is a background line. A γ-gate set to this peak in a $\gamma\gamma$-matrix only shows lines of ^{27}Al. It is thus assumed, that this line is the lowest transition in ^{27}Al, which is of 844 keV according to the literature [1]. This transition is solely stated by Ref. [45] to belong to ^{106}Cd.

The 1704 keV line is placed wrong in NNDC [1] and Ref. [45]. Gating on the 2339 keV energy in the particle spectrum the 1704 keV line is not visible in the γ-ray spectrum. Setting a p-gate to ~3200 keV and a γ-gate to 1704 keV in a p$\gamma\gamma$-matrix one observes the 861 keV line (stemming from the 1494 keV level) and 633 keV line (stemming from the 633 keV level), proving this transition stands on top of the 1494 keV level. Thus a new level at 3198 keV was found in this work. In Ref. [45], where this level was observed, only one γ-ray of the Yrast-cascade $6_1^+ \overset{998\,\mathrm{keV}}{\rightarrow} 4_1^+ \overset{861\,\mathrm{keV}}{\rightarrow} 2_1^+ \overset{633\,\mathrm{keV}}{\rightarrow} 0_1^+$ were used as requirement of coincidence to identify lines of ^{106}Cd. This simple coincidence requirement can lead to a wrong placement of the γ-ray without the information of level excitations.

The 2468 keV Level Three new depopulating transitions were found for this level. One transition already published in [27] was confirmed. Results can be taken from Table 3.1.

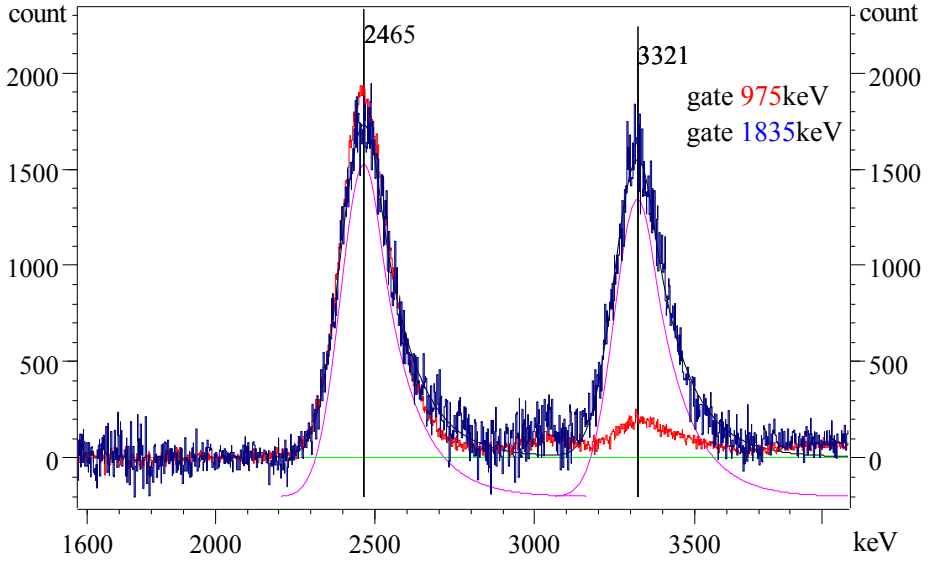

Figure 3.7: The back scattered particle spectra of the 975 keV peak (red) and the 1835 keV peak (blue) normalized, that the counts of the level excitations at 2468 keV are equal. (Energy uncertainty ±10 keV.)

One interesting case of these transitions is the 2468 keV $\overset{1836\,\mathrm{keV}}{\rightarrow}$ 633 keV transition. It could be proven, that the association of this γ-ray to a level at 3329 keV in the literature [1] (NNDC) is not correct. The known literature values for that transition are stemming solely from Ref. [39]. In this work it was found, that the particle spectra gated on the 975 keV (red color) and 1836 keV transition (blue color) in Figure 3.7 show level excitations at approximately 2470 keV and 3330 keV, proving the 1836 keV line belongs to the 2468 keV level with a possible doublet γ-transition stemming from a level at ~3330 keV. However, another explanation for

the bump at ∼3330 keV is a possible γ-ray of approximately 860 keV depopulating a level at ∼3330 keV, which is feeding the 2468 keV level. The particle spectrum gated on the 1836 keV transition has therefore been normalized to the 2468 keV level excitation bump of the 975 keV γ-gate to account for the different γ-ray intensities and the weaker γ-ray efficiency at higher energies in the germanium detectors. This way, one can see from the comparison of both spectra in Figure 3.7, that the 1836 keV line has a higher amount of coincident level excitations at ∼3330 keV than the 975 keV line. This difference in the particle count rate leads to the conclusion, that the 1836 keV line is a doublet, as for a single feeding γ-ray coming from a ∼3330 keV level both p-spectra should show the same amount of excitation from the feeding level (after normalization). The non-zero level excitation at ∼3330 keV in the 975 keV gated spectrum (red color) however reveals, that there also has to be a feeder from a ∼3330 keV level to the 2468 keV level. This challenging situation is shown in the level scheme in Figure 3.8. With a γ-ray gate set to the 752 keV line (green color) combined with a particle gate set to ∼3330 keV in a p$\gamma\gamma$-matrix the energy of the unknown feeder (860 keV) to the 2468 keV level could clearly be extracted (see Figure 3.9) due to the fact, that this cascade circumvents the 861 keV line of the 4_1^+ state, contributing to this doublet. These findings, shown in Figure 3.8, result in the complex situation that two γ-ray doublets at 860 keV/861 keV (red color) and 1836 keV/1834 keV (red color) stack crosswise on top of each other in two separated cascades. The energy of the 1836 keV line stemming from the 2468 keV level could easily be extracted by setting a particle gate to that level and fitting the γ-peak. To find the energy of the 1834 keV line belonging to the level at 3328 keV a particle gate was set to that higher level and the peak was fitted as a doublet with one of the two energies set fixed to the recently extracted value. See also Figure 3.20 and the discussion about the 3328 keV level. Besides these findings, there is also evidence for a 1836 keV transition belonging to the 2468 keV level in the data of the $(n, n'\gamma)$-experiment [29].

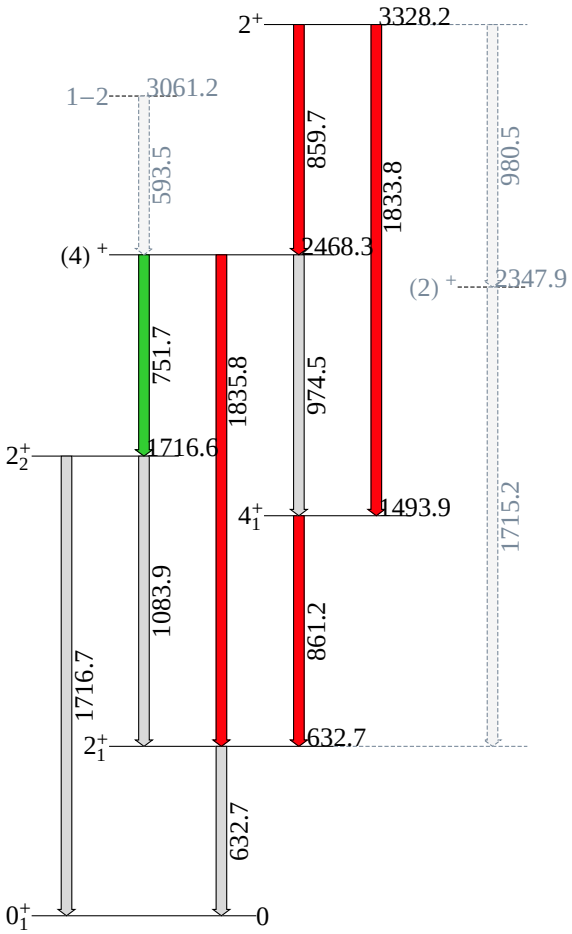

Figure 3.8: The γ-ray cascades of the 1836 keV and the 860 keV doublet and part of the level scheme of the $1^+, 2^+$ -level at 3328 keV and the (4^+)-level at 2486 keV. Red color indicates the two doublets. Green color marks the gate to resolve the two doublets.

Note that the small bump at ∼3050 keV in the p-spectrum stems from the newly discovered feeding 3061 keV $\overset{594\,\mathrm{keV}}{\rightarrow}$ 2468 keV transition to this level.

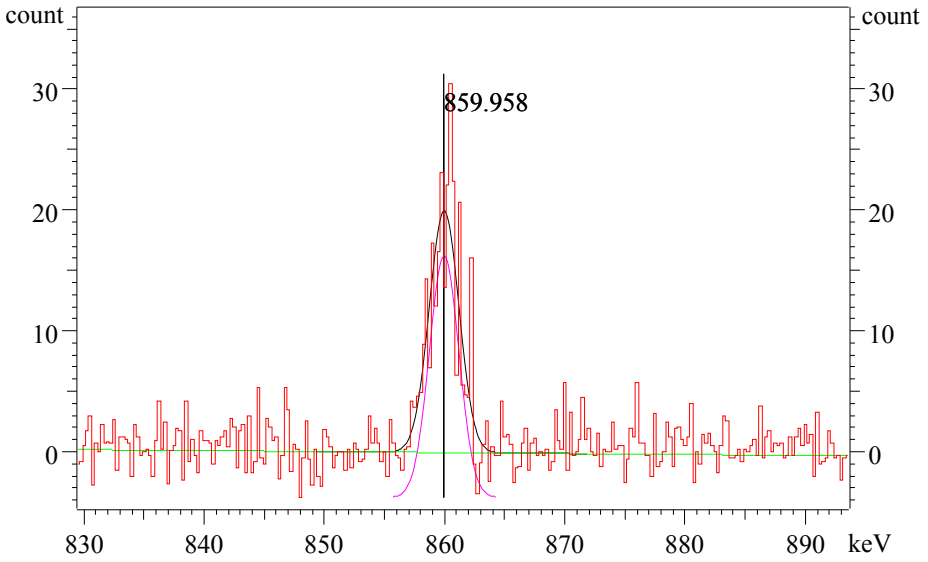

Figure 3.9: Fit of the 860 keV line after setting a 100 keV p-gate to an energy of 3330 keV and a γ-gate to the 752 keV peak.

J. Kumpulainen et al. [30] conducted a similar $(p, p'\gamma)$-experiment on ^{106}Cd, where γ-rays were measured in coincidence with scattered protons. The Top of Figure 3.10 shows a particle spectrum taken from [30] with a γ-gate set to the 1715 keV/1717 keV doublet-peak. The bottom of Figure 3.10 shows the same spectrum with the same gate set in this work. The similarities in both spectra are apparent. (Note, that energies are descending from left to right.) As one can see from the top of Figure 3.10, a level excitation at roughly ∼3300-3400 keV is visible in the p-spectrum, which can be related to the excitation of the 3328 keV level, when comparing both spectra. However this is not a proof for the 3328 keV $\overset{860\,\mathrm{keV}}{\rightarrow}$ 2468 keV transition as part of the cascade 3328 keV $\overset{860\,\mathrm{keV}}{\rightarrow}$ 2468 keV$\overset{752\,\mathrm{keV}}{\rightarrow}$ 1717 keV$\overset{1717\,\mathrm{keV}}{\rightarrow}$ 0 keV, as the already known 3328 keV $\overset{981\,\mathrm{keV}}{\rightarrow}$ 2348 keV$\overset{1715\,\mathrm{keV}}{\rightarrow}$ 633 keV cascade also deexcites the 3328 keV level. Thus, as already mentioned, only a gate set to the 752 keV γ-ray gives a final proof for the 3328 keV $\overset{860\,\mathrm{keV}}{\rightarrow}$ 2468 keV transition and the γ-energy as the 1494 keV $\overset{861\,\mathrm{keV}}{\rightarrow}$ 633 keV transition is circumvented. Figure 3.11 shows the p-spectrum after gating on the 752 keV γ-ray, revealing the excitations of the 3061 keV and 3328 keV level (compare with the level scheme in Figure 3.8). Note that the 3328 keV $\overset{860\,\mathrm{keV}}{\rightarrow}$ 2468 keV$\overset{214\,\mathrm{keV}}{\rightarrow}$ 2254 keV$\overset{1621\,\mathrm{keV}}{\rightarrow}$ 633 keV cascade also circumvents the 1494 keV $\overset{861\,\mathrm{keV}}{\rightarrow}$ 633 keV transition, but contains too low statistic according to the relative γ-intensities of the 2468 keV level.

As the analysis of J. Kumpulainen et al. did not exceed 2.4 MeV, this situation, concerning the 860 keV/861 keV and 1834 keV/1836 keV doublet, is solved here for the first time.

The 2486 keV Level For this level the 769 keV transition to the 2_2^+state, first found in Ref. [27], could be confirmed. It was also found in this work, that

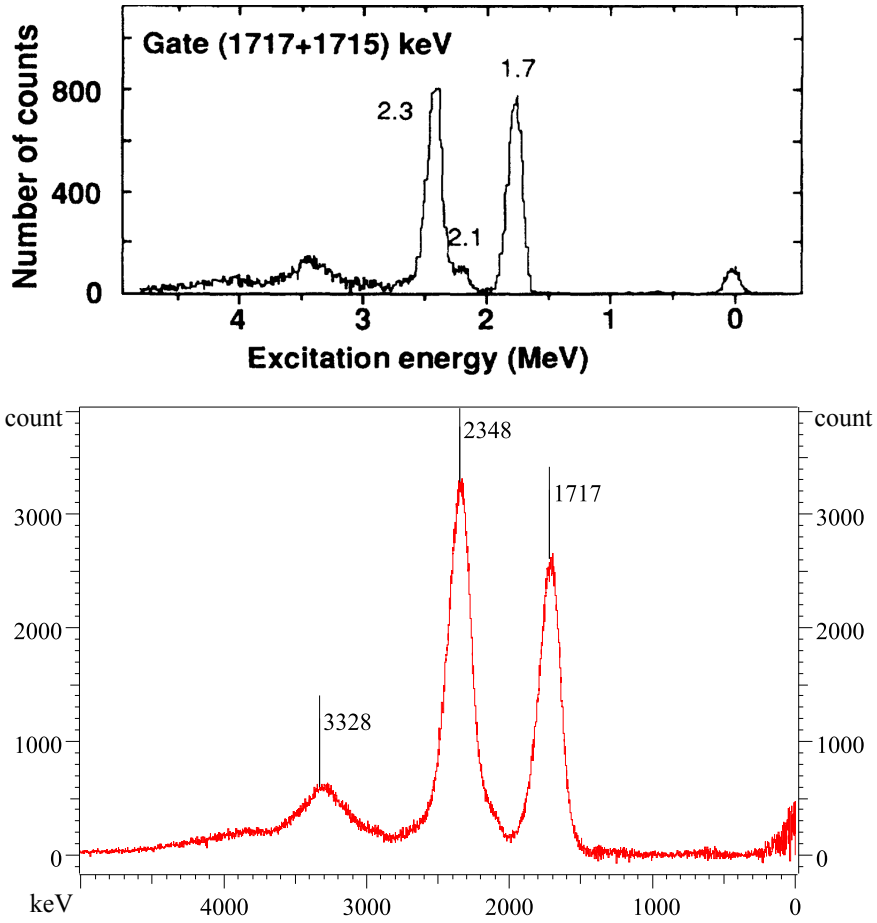

Figure 3.10: Top: Particle spectrum, taken from Kumpulainen et al. [30]. A γ-gate was set to the 1715 keV/1717 keV doublet-peak in the $(p, p'\gamma)$-experiment in that work.
Bottom: The same gate was set to the 1715 keV/1717 keV doublet-peak in this work, energies have been rescaled to descend from right to left to match with the upper figure. Vertical lines indicate certain energy levels.

this peak is a doublet with the involved transitions 3489 keV $\overset{772\,\mathrm{keV}}{\rightarrow}$ 2717 keV and 2486 keV $\overset{769\,\mathrm{keV}}{\rightarrow}$ 1717 keV. Besides that, it was found, that the 992 keV line is a doublet too, with the already mentioned feeder to the 2252 keV level, 3246 keV $\overset{993\,\mathrm{keV}}{\rightarrow}$ 2252 keV and the 2486 keV $\overset{992\,\mathrm{keV}}{\rightarrow}$ 1494 keV transition. These new findings result in a different branching ratio than given in the literature [1], where the branching for 992 keV : 1854 keV is 95(9) % : 100(30) %. In this work the branching ratio for 382 keV : 769 keV : 992 keV : 1854 keV was derived as 4.23(58) % : 14.52(78) % : 39.2(19) % : 100.0(42) %. This is a confirmation of the findings in [27] conducted with the HORUS-experiments in Cologne, which reported for 769 keV : 992 keV : 1854 keV ratios of 12.1(30) % : 34.4(50) % : 100(10) %, whereas the results derived from the $(n, n'\gamma)$-experiment in Kentucky in that same work differ from this work [27], with a branching ratio for 769 keV : 992 keV : 1854 keV given as 28.6(20) % : 35.0(13) % : 100.0(17) %.

Due to the newly discovered doublets the branching ratios of this work are con-

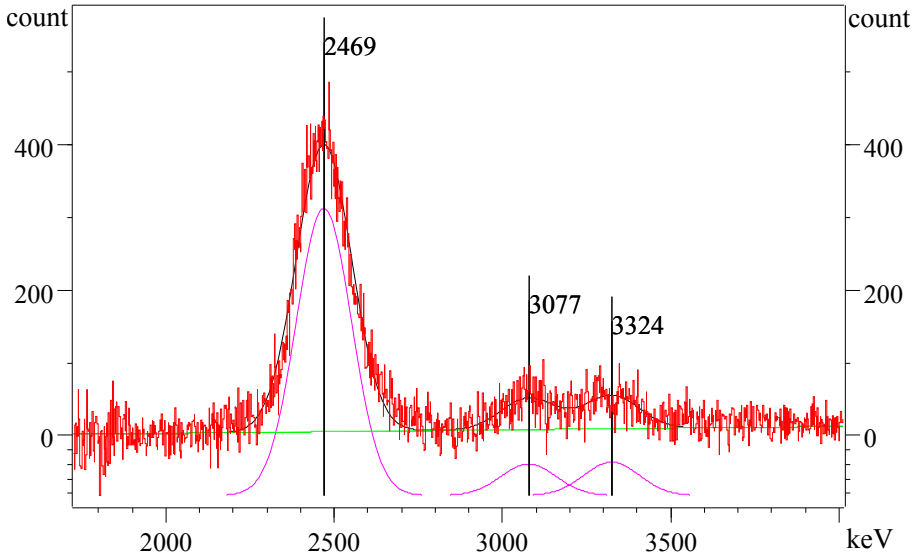

Figure 3.11: Particle spectrum after setting a γ-gate to the 752 keV peak depopulating the 2468 keV level. The excitation of the 3328 keV level via the 3328 keV $\overset{860\,\mathrm{keV}}{\rightarrow}$ 2468 keV transition is clearly observable within the energy resolution of the Si-detectors. (Energy uncertainty $\pm$10 keV.)

sidered be the more valid values.

The 2492 keV Level The 161 keV transition to the 2330 keV level quoted in the literature [1], but only seen in [47], could not be confirmed in agreement with [27]. Instead a γ-ray with a similar energy value of 163 keV was assigned to the 2468 keV level.

The 2522 keV Level, given in the literature It was found, that the 1028 keV γ-ray is placed wrong in the literature [1], depopulating a 2522 keV level. As this is the only stated transition of that level in the literature, this level is not existent. In the work of L. E. Samuelson et. al. [45], where this transition is reported, only a single coincidence with any of the γ-rays of the Yrast-cascade $6_1^+ \overset{998\,\mathrm{keV}}{\rightarrow} 4_1^+ \overset{861\,\mathrm{keV}}{\rightarrow} 2_1^+ \overset{633\,\mathrm{keV}}{\rightarrow} 0_1^+$ was used as requirement to identify lines of ^{106}Cd. This method without any information about coincident level excitations from particle detectors for the examined peak can lead to false placements of transitions in the level scheme. However, within the 4 MeV level energy range of this work, it was found that the 1028 keV peak is a triplet with the contributing transitions 2825 keV $\overset{1029\,\mathrm{keV}}{\rightarrow}$ 1795 keV, 3333 keV $\overset{1028\,\mathrm{keV}}{\rightarrow}$ 2305 keV, 3358 keV $\overset{1027\,\mathrm{keV}}{\rightarrow}$ 2330 keV. If one also includes the information given in the literature [1] about the 4816 keV and 5822 keV level, the 1028 keV peak might also be considered as a quintuplet.

The 2566 keV Level From Ref. [27] it was not clear if the 772 keV and 849 keV γ-rays really depopulate this level, as these were seen in the HORUS-experiments in Cologne with rather weak intensities, but not in the $(n, n'\gamma)$-experiment in Kentucky. These transitions could be confirmed in this work. The branching ratio in [27] for the

γ-rays 772 keV : 849 keV : 1934 keV was 0.2(1) % : 0.4(1) % : 100(10) %. These weak intensities could nearly be reproduced in this work, as a ratio 0.24(7) % : 0.79(7) % : 100.0(42) % was found.

The 2630 keV Level The same controversy of uncertain γ-rays as in the case of the 2566 keV level occurred here respective the 486 keV and 914 keV lines. The existences of these transitions was confirmed. The 835 keV transition can also be observed in the $(n, n'\gamma)$-experiment [29].

Together with the 837 keV line of the 2331 keV level and the 837 keV line of the 3198 keV level, the 835 keV line of this level is a triplet. Such situations can be resolved clearly by setting a p-gate to the level exciatation energy and a γ-gate from below, to extract the transition energy. However, branching ratios are extracted with only a p-gate set, from the resulting γ-singles spectrum. For the extraction of count rates of certain lines in a multiplet peak, energies have been fixed to the energy values extracted using a γ-gate from below. Such a procedure is of course only necessary, when the p-gate includes one or more levels of the γ-multiplet. Figure 3.12 shows this case as an example for the procedure. The p-gate has been set to the 2630 keV level with a width of 200 keV, γ-energies have been fixed to their extracted values, as described. The χ^2-value of this fit was $\sim$1.8.

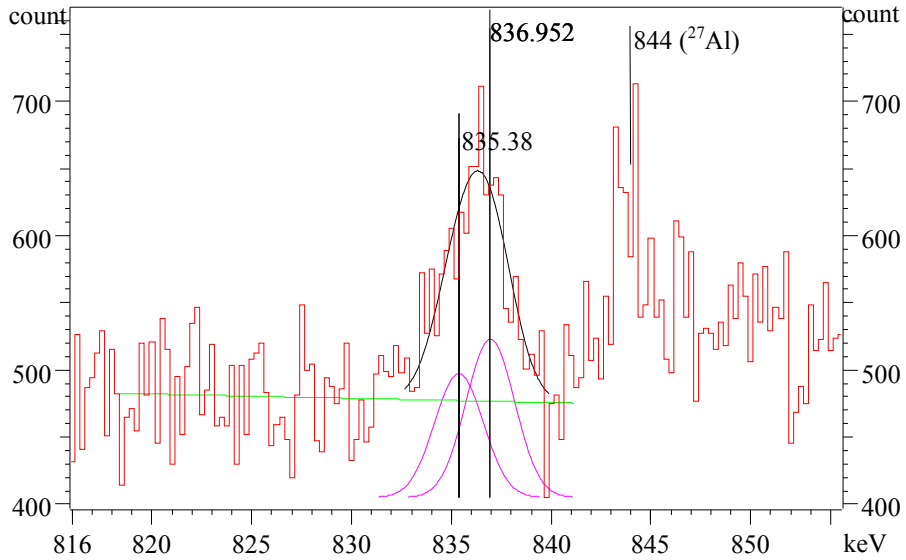

Figure 3.12: Fit of the 837 keV line of the 2331 keV level and the 835 keV line of the 2630 keV level with a p-gate of 200 keV width set to 2630 keV. Energies for this doublet fit have been fixed to values extracted separately, with a γ-gate from below. The 844 keV peak of ^{27}Al is also present in the spectrum.

The 2711 keV Level This level with a transition to the 4_1^+-state, discovered in [27] could be confirmed by a gate from below. A spin range of $2-6$ has been assigned to this level.

The 2718 keV Level The 339 keV and 1001 keV transitions of this level found for the first time in [27] could be confirmed by gates from below.

The 2719 keV Level The ground state transition first reported in [27], was seen in the $(n, n'\gamma)$-experiment in Kentucky but not in the HORUS-experiments in Cologne. That transition has also been observed in this work. Spin 3 was thus canceled from the literature [1] spins 1, 2^+, 3.

The 2793 keV This level was reported in [27] and could be confirmed with all stated γ-rays therein, see Table 3.1. A spin range of $2-6$ was set here. A level with this energy has already been reported in [48] even though it can not be found in [1]. Nevertheless the 2793 keV $\overset{225\,\mathrm{keV}}{\rightarrow}$ 2567 keV and 2793 keV $\overset{2795\,\mathrm{keV}}{\rightarrow}$ 0 keV transitions stated in [48] could not be observed in this work.

One interesting case here is the 2793 keV $\overset{1299\,\mathrm{keV}}{\rightarrow}$ 1494 keV transition, which is misplaced in the literature [1] by associating this γ-ray to the 3015 keV level. This misplacement was proposed by [39]. However, as Figure 3.13 shows, this γ-ray is coincident to the 633 keV and 861 keV line by applying a gate to the 1299 keV γ-ray combined with a p-gate ranging from 2900 keV to 3100 keV in a p$\gamma\gamma$-matrix. This proves, that this γ-ray stands on top the 4_1^+-state.

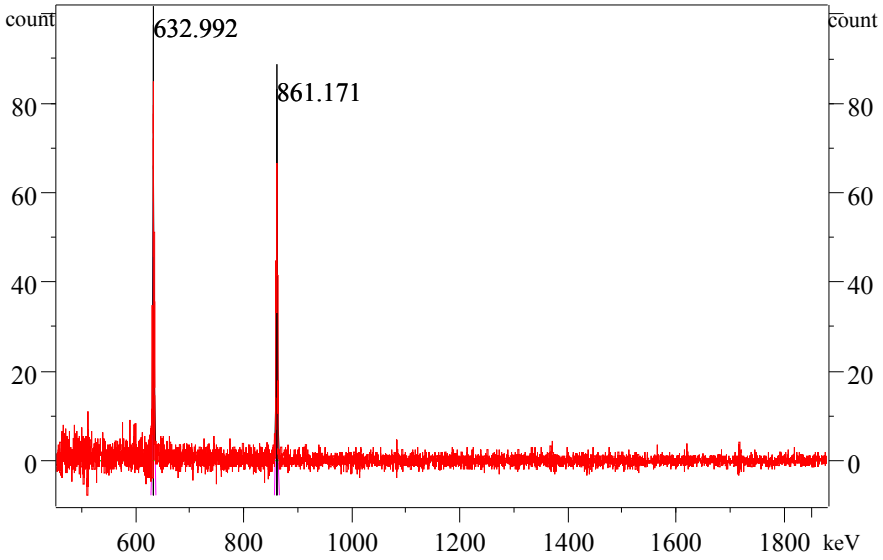

Figure 3.13: Gated spectrum with a γ-gate on 1299 keV combined with a particle gate ranging from 2900 keV to 3100 keV, set in a p$\gamma\gamma$-matrix.

The 2801 keV Level This level and its transitions were first seen in [27], but only in the results of the HORUS-experiments. All γ-rays of this level could be remeasured and associated to this level. Possible level spin range from 2 to 6.

The 2825 keV Level Two new γ-rays depopulating this level were discovered. Within the 4 MeV level energy range of this work the 2825 keV $\overset{1029\,\mathrm{keV}}{\rightarrow}$ 1795 keV transition a triplet together with the transitions 2825 keV $\overset{1029\,\mathrm{keV}}{\rightarrow}$ 1795 keV, 3333 keV $\overset{1028\,\mathrm{keV}}{\rightarrow}$ 2305 keV and 3358 keV $\overset{1027\,\mathrm{keV}}{\rightarrow}$ 2330 keV (see also the discussion about this peak in the paragraph about the 2522 keV level). The 2191 keV line could also be observed in the Kentucky $(n, n'\gamma)$-experiment [29].

The 2889 keV Level This level is assigned with spin 2,3$^+$ in the literature [1]. However in the work of Linnemann [27] there are signs for a level doublet at this energy with a possible spin assignment of $J = 1$ for the new level. Although two new feeders to this level were found, 3328 keV $\overset{439\,\mathrm{keV}}{\rightarrow}$ 2889 keV and 3372 keV $\overset{482\,\mathrm{keV}}{\rightarrow}$ 2889 keV, the statistics are too weak to verify a level doublet. As a $\gamma\gamma$-angular correlation analysis was not part of this work, a crosscheck for two different spins at this level energy is not possible. Thus the assumption of a level doublet was neglected. Nevertheless all γ-rays, already found in [27] according to this level energy could be remeasured. Branching ratios have been estimated, assuming a single level at this energy. The 3$^+$ spin has been canceled from the literature values, due to the observation of a ground state transition. Incorporating findings of [27] for transitions from a $J = 1$ state, a spin range of $1 - 2$ was assigned to this level.

The 2896 keV Level The depopulating transition with an energy of 1402 keV to the 4_1^+-state first observed in [27] was confirmed. A new 791 keV transition depopulating this level could be found in this work, which was misplaced at the 3284 keV level in the literature [41]. A γ-gate from below on the 611 keV line of the 2105 keV level proofs the 2896 keV $\overset{791\,\mathrm{keV}}{\rightarrow}$ 2105 keV transition. According to these depopulating transitions, level spins of $2 - 6$ have been assigned to this level.

The 2915 keV Level This new level was discovered due to the transition 2915 keV $\overset{2282\,\mathrm{keV}}{\rightarrow}$ 633 keV. Level spins have been set to $0 - 4$. Due to a non-observed ground state transition the spins $J = 1$, 2 are more improbable.

The 2918 keV Level The two γ-rays 1123 keV and 1201 keV were first seen in [27], but only found with the HORUS-experiments in Cologne. These findings could be confirmed.

The 2921 keV Level In [27] this level has an additional 542 keV transition only seen with the HORUS-experiments. It was found that this γ-ray is mistakenly placed depopulating this level. When gating on this peak in a $\gamma\gamma$-matrix only the 1715 keV from the (2$^+$)-state at 2348 keV is visible, plus lines stemming from lower energetic levels. Also a gate from below on the 1746 keV peak of the 2379 keV level did not show a 542 keV line. Thus this peak can only be associated to the 2889 keV level.

The 2925 keV Level This level was not observed in [27] during the $(n, n'\gamma)$-experiment in Kentucky but with the HORUS-experiments. The 433 keV γ-ray could be associated to this level energy in this work. However the 1431 keV line, suggested in [41, 49] was not observed. In these works this line is stated to be a transition to the 4_1^+-state. In this work a γ-gate set to the 861 keV line (of the 4_1^+-state) from below combined with a particle gate set to this level energy, revealed a 1433 keV peak instead. See Figure 3.14 for details. This same situation occurs with the depopulating 820 keV transition, which is reported in [41], but can not be found in [1]. This line was not observed in this work. Instead a 2927 keV $\overset{822\,\mathrm{keV}}{\rightarrow}$ 2105 keV

transition was found by the same means as the 2927 keV $\overset{1433\,\mathrm{keV}}{\rightarrow}$ 1494 keV transition. Thus these γ-rays are associated to the newly discovered 2927 keV level.

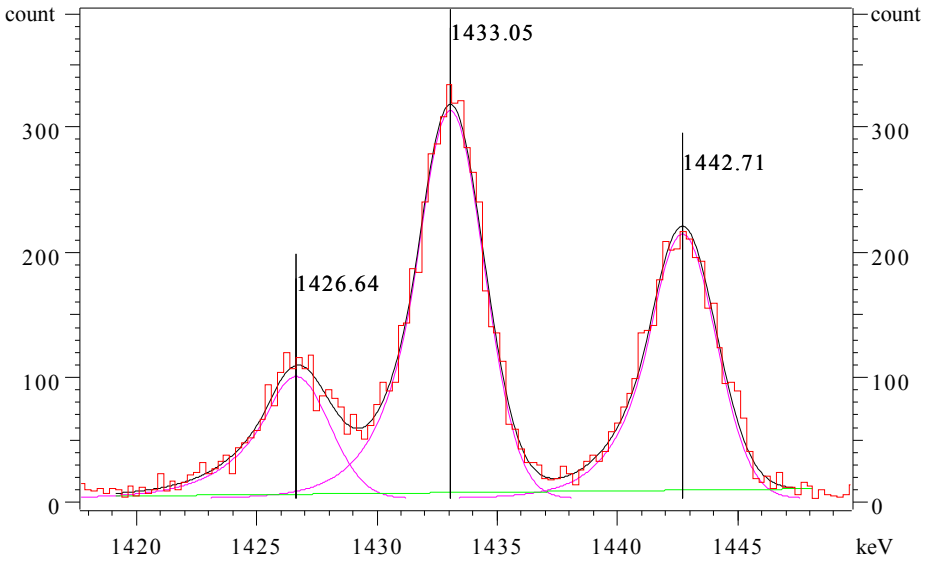

Figure 3.14: γ-ray spectrum with a fit of the 1433 keV line after applying a γ-ray gate on the 861 keV line of the 4_1^+-state combined with a 100 keV wide particle gate on a level energy of 2920 keV.

The 2927 keV Level Four γ-rays were found depopulating this new level (see Table 3.1). The 1433 keV line among these γ-rays was previously associated to the 2925 keV level in the literature [1], which was found to be a misplacement. See also the discussion about the 2925 keV level and Figure 3.14 for the association of the 1433 keV γ-ray to the 2927 keV. Note that, the 822 keV, the 1433 keV and the 2294 keV transitions can also be observed by the $(n, n'\gamma)$-experiment, according to a newer review of the data [29] (N. Warr, priv. comm.). A spin range of $2-4$ has been assigned to this level.

The 2933 keV Level, given in the literature In common with the findings in [27], there is no evidence for this level, reported by Ref. [39]. The single 1217 keV transition suggested to depopulate this state was proven to belong to the 2711 keV level, in coincidence to the level excitations in the p-spectrum.

The 2936 keV Level The 1443 keV transition depopulating this level found in [27] was remeasured, see Figure 3.14. Three new transitions were found (see Table 3.1). The 831 keV transition among these new findings was also observed in the $(n, n'\gamma)$-experiment, although it was not published yet [29]. The 631 keV transition could not directly be observed, but could be associated to this level by analyzing a 631-634 keV multiplet. See the discussion about the 3128 keV level for further details about the procedure.

The 2973 keV Level This level was not observed in the $(n, n'\gamma)$-experiment in [27], but with the HORUS-experiments a new 1178 keV γ-ray was observed. The association of this γ-ray to this level could be confirmed. Due to this confirmed transition to a 0^+-state, spins 3^+ and 4^+ have been canceled out of the proposed literature spins 2, 3^+, 4^+ [1].

The 3013 keV Level This new level was discovered via a 1519 keV transition to the 4_1^+-state and a 2380 keV transition to the 2_1^+-state. A spin value of $2-4$ has been assigned to this level. As no ground state transition was observed, $J = 2$ is less probable.

The 3015 keV Level, given in the literature The 1299 keV line could not be observed with this level energy in the particle spectrum. It was found to be misplaced at this level energy in [39]. This γ-ray was shifted to the 2793 keV level, see discussion there. Thus it is assumed, that this level does not exist.

The 3018 keV Level In the $(n, n'\gamma)$-experiment of Ref. [27] this levels was not observed, but with the HORUS-setup in Cologne 2 new transitions were discovered in that work. These two new transitions could be confirmed, two additional transitions were discovered in this work. See Table 3.1 for details.

The 3020 keV Level This state was not observed in the $(n, n'\gamma)$-experiment of Ref. [27]. In this work, in addition to the known 2388 keV line feeding the 2_1^+ state, a new 1304 keV transition to the 2_2^+ state with a branching of 8.09(48)% was discovered.

The 3061 keV Level This level, first discovered in [27], was only observed with the HORUS-experiments via the 2429 keV transition to the 2_1^+-state. This result could be confirmed. Additionally three new transitions 3061 keV $\overset{594\,\mathrm{keV}}{\rightarrow}$ (4), 3061 keV $\overset{1345\,\mathrm{keV}}{\rightarrow}$ 2_2^+ and 3061 keV $\overset{3061\,\mathrm{keV}}{\rightarrow}$ 0_1^+ were discovered. The spin of this level is stated as $J = (1), 2$. Spin $J = (1)$ has not been canceled out, due to the tentative value $J_f = (4)$ of the final state of the 593.5 keV transition. On top of this, that line forms a doublet with the 592.8 keV line belonging to the 3084 keV level.

The 3073 keV Level In [27], this level was not reported in the analysis of the $(n, n'\gamma)$-experiment, but it was seen in the HORUS-experiments with a newly discovered 694 keV γ-ray there. This transition could be confirmed and two new transitions were found, see Table 3.1. The ground state transition however can also be observed in a new data analysis of the $(n, n'\gamma)$-experiment [29]. The literature [1] gives spins 2, 3^+, 4 for this level. Due to the newly discovered and confirmed transitions, the spin is set to 2.

The 3084 keV Level By seperately gating from below to see the three depopulating γ-rays stated in [1] only the 3084 keV $\overset{593\,\mathrm{keV}}{\rightarrow}$ 2492 keV transition was observed with very weak statistics (γ-gate at 998 keV). The 581 keV and 754 keV γ-rays were

not observable. This agrees the literature in the sense, that the 583 keV γ-ray is supposed to be the strongest line of this level. But it was weekly populated in this experiment, due to its relativly high spin ($J = 7^+$) for a (p, p') reaction. In [43, 41, 49, 47, 50, 51, 45] the 3084 keV $\overset{581\,\mathrm{keV}}{\rightarrow}$ 2503 keV (38(4) % [1]) and the 3084 keV $\overset{754\,\mathrm{keV}}{\rightarrow}$ 2331 keV (71(5) % [1]) transitions have been observed in coincidence with the most intensive lines of each final level, i.e. 1010 keV and the 226 keV γ-rays respectively.

In [43, 41, 49] the β^+/EC decay of ^{106}In is studied, where this level was directly populated from the ^{106}In ground state [49]. In [47] high energy $(\alpha, 2n)$ and in [47, 50, 51, 45] heavy ion fusion evaporation reactions are used. It can be seen in [50, 51] that the 3084 keV level is fed by two band heads. In support, this level is more favorly to be populated by other reaction channels, than by the $(p, p'\gamma)$-reaction used in this work.

The 3093 keV Level This state was not observed in [27]. In this work a new transition from this level was discovered, 3093 keV $\overset{788\,\mathrm{keV}}{\rightarrow}$ 2305 keV with a branching ratio of 20.0(19) %. Whereas the 3093 keV ground state transition, stated in [39], could not be observed with a p-gate set to this level energy. In the literature the branching ratios for the γ-rays 1376 keV : 1599 keV : 2460 keV, stemming from [39], are given as 100(13) % : 35(5) % : 75(5) %. Whereas the branching in this work was distinguished as 78.5(48) % : 71.2(43) % : 100.0(53) %.

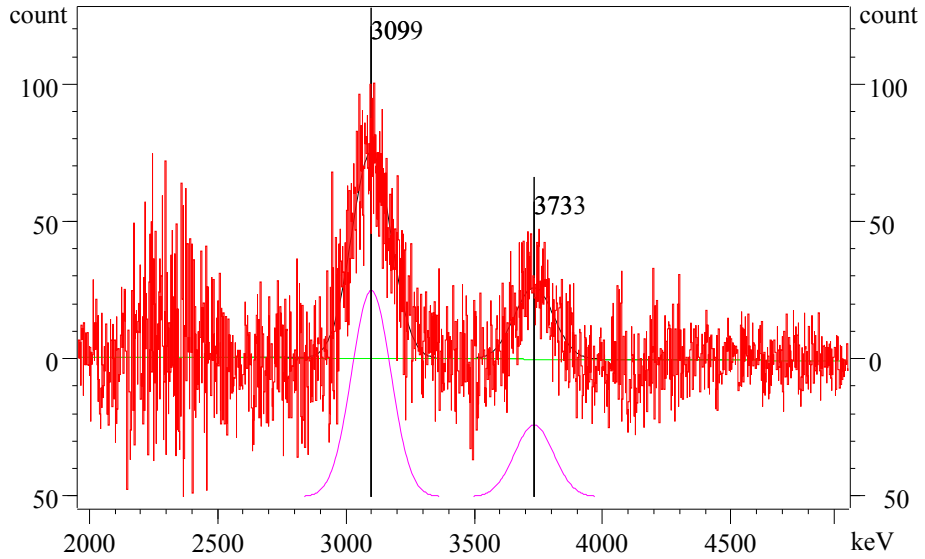

Figure 3.15: Particle spectrum with fits of level excitation enrgies after gating on the 1376 keV peak. (Energy uncertainty ±10 keV.)

An explanation for these differences in relative intensities, can be found in the level scheme of ^{107}Cd, which has a 1377 keV$(J = \frac{7}{2}^+)$ $\overset{1377\,\mathrm{keV}}{\rightarrow}$ 0 keV$(J = \frac{5}{2}^+)$ transition [1]. It is thus possible that ^{107}Cd has been observed unnoticed as a product of a neutron capture reaction during the (n, n')-experiment conducted in [39]. This in turn would result in an enhanced count rate of 1377 keV.

On top of that, it was found, that the 1376 keV/1377 keV peak is a doublet. Figure 3.15 shows the p-spectrum after gating on this peak in the γ-spectrum. The spectrum reveals, that there is eigther a doublet in this peak or a feeder from a level at ∼3730 keV to the 3093 keV level. The energy distance between both excitations is ∼633 keV, which also opens the possibility for a ∼633 keV transition to be a feeder. (Note that the $2_1^+ \rightarrow 0_1^+$transition also has an 633 keV energy thus resultig in a doublet.) Figure 3.16, displaying a partial level scheme of the findings to guide the discussion.With the use of a p$\gamma\gamma$-matrix and a p-gate of 100 keV width set to the 3725 keV level and a γ-gate set to the 1084 keV line (green) no 1376 keV peak (red) could be observed. This finding ensured no feeding to the 3093 keV level. On the other hand shifting the $\gamma-$gate to the 1715 keV/1717 keV doublet resulted in a 1377 keV peak (blue) free of contributions from the 1376 keV component, which made the extraction of transition energy value possible for that line. At the same time it was proven, that a 1377 keV line is standing on top of the 2348 keV level instead of a ∼633 keV line on top of the 3093 keV level. By that the new 3725 keV level was discovered.

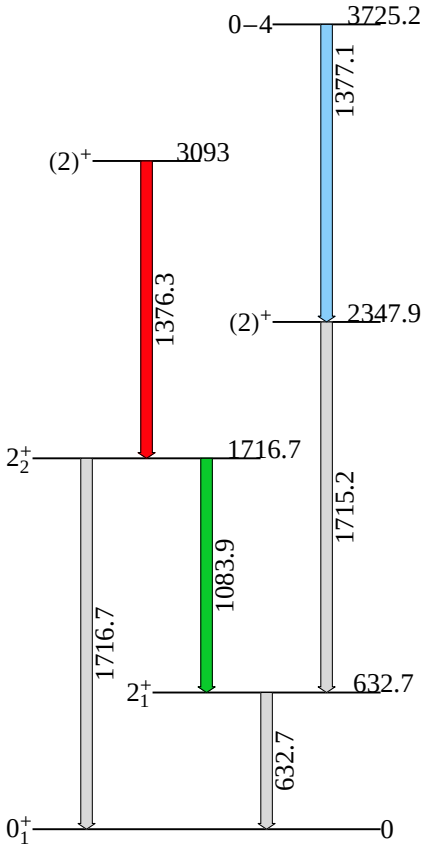

Figure 3.16: Partial level scheme showing γ-rays following the 1376 keV/1377 keV doublet. (Note, that the 3093 keV level is also depopulated by a 788 keV, 1599 keV and 2460 keV line, which are not displayed to keep a clear arrangement.)

The 3094 keV Level, given in the literature This level is only observed in [52], but could not be confirmed in this work. A gate from below on the 998 keV γ-ray reveals only a flat background at the position of the expected 602 keV coincidence line in a $\gamma\gamma$-matrix. A flat background is also observed at this position after gating on this level energy in a pγ-matrix. It is thus assumed, that this level does not exist.

The 3119 keV Level There are two levels at this energy according to the literature [1]. One at 3118.8 keV with a spin assignment of 2+, 3+ ,4+ and one at 3119.7 keV with a spin of 1. However in [27, 44] these levels were merged to a single spin 1 state. Reference [41] also states only one level without giving a spin value. The 3119 keV $\overset{1625\,\mathrm{keV}}{\rightarrow}$ 4_1^+ transition, which was only observed in [39] could not be confirmed in this work, by gating from below on the 861 keV peak. That particular reference [39] also solely states the second level with spin 2+, 3+ ,4+. The non-

observation of the 3119 keV $\overset{1625\,\mathrm{keV}}{\rightarrow}$ 4_1^+ transition sugests there is a single level with a spin $J = 1, 2$ assignment in agrement with [27, 44, 41], as all other transitions of this single level go to 0^+- and 2^+-states. A spin $J = 1$ was adopted from [27, 44, 41]. By remeasuring all transitions, including those discovered in [27, 44] for the first time, the variation in the level energy according to each depopulating γ-ray was found to be of max 0.2 keV around 3119.4 keV. This in turn makes the picture of only one single level even more reliable, as this variation is significantly smaller than the 1 keV energy difference between the two levels given in the literature. Reference [48] first reported the 3119 keV $\overset{553\,\mathrm{keV}}{\rightarrow}$ 2566 keV transition, although it was not included in NNDC [1], whereas the 3119 keV $\overset{1622\,\mathrm{keV}}{\rightarrow}$ 1494 keV transition reported in [48] was not observed in this work.

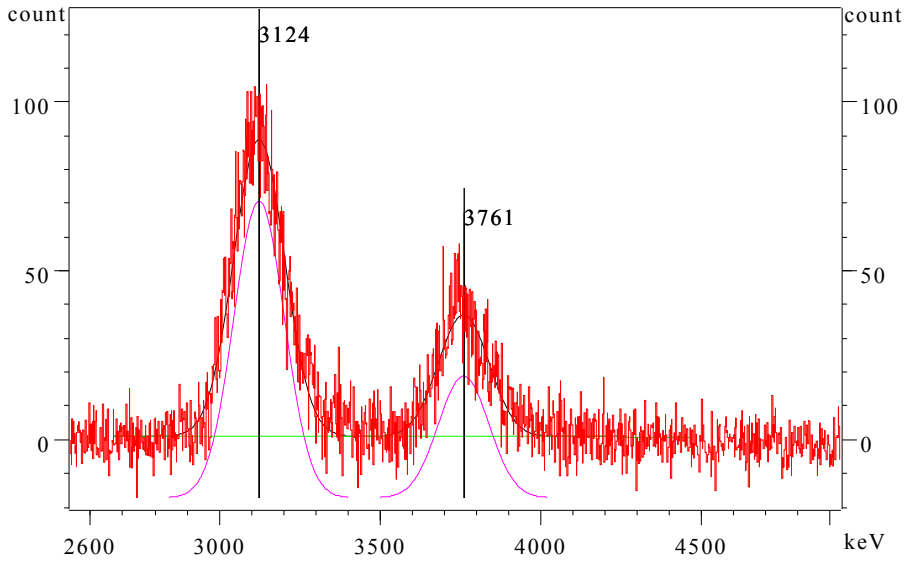

Figure 3.17: Particle spectrum with fits of level excitations after gating on the 3118 keV peak. (Energy uncertainty ±10 keV.)

The major difference in branching ratios between [39], [27, 44] and this work occurs between the 2486 keV and 3118 keV lines. In [39] the relative branching ratio is given respectively as 64(9) % : 100(9) %, whereas in [27, 44] those values are 100(10) % : 96(10) %. In [41] intensities were measured relative to the most intense 633 keV $\overset{633\,\mathrm{keV}}{\rightarrow}$ 0 keV transition. The intensities of the 2486 keV and 3118 keV lines are given there as 0.18 % : 0.18 %. In this work a branching ratio of 100.0(45) % : 54.3(25) % was derived, which agrees within the error bars with the findings in [27, 44] with the 2486 keV line being the strongest. Nevertheless, the intensity of the 3118 keV γ-ray seems underestimated compared to other works.

An explanation for the differences in branching ratios relative to [27, 44] can be found in Figure 3.17. It shows the level excitations in the p-spectrum coincident with the 3118 keV line, revealing that a higher energy component is also present, which is a hint, that the 3118 keV peak is a doublet. Figure 3.18 shows a γ-spectrum after setting a p-gate from 3.6 MeV up to 4.2 MeV and a γ-gate to the 633 keV peak of the 2_1^+-state (in a p$\gamma\gamma$-matrix). Although the energy calibration in the shown region is approximately 2-5 keV too low, one can see that certain high energy γ-rays are

standing on the 2_1^+-state. One of these γ-rays matches with an energy of $\sim 3119\,\mathrm{keV}$, which explains the higher energy component in Figure 3.17 and proves this line is a doublet, which can lead to an "over counting" of the 3118 keV line in other works. (Note that no peak fits are shown in Figure 3.18, the vertical line only mark certain energy values.) As one can see from figure 3.17, a p-gate of 100 keV width set to the level energy of 3119 keV will produce a clean peak fit in the resulting γ-spectrum without any contribution from the higher component. Thus, the branching ratio derived here is considered more reliable than previous values.

Due to the mentioned deficiency in the energy calibration in this region, this newly discovered $\sim 3752\,\mathrm{keV} \xrightarrow{\sim 3119\,\mathrm{keV}} 633\,\mathrm{keV}$ transition as well as the according new level is not part of the results of Table 3.1. It is only used to justify the branching ratio found in this work. It is emphasized, that only γ-rays below $\sim$2.3 MeV, where the energy calibration is reliable, have been taken for the calculation of level energies.

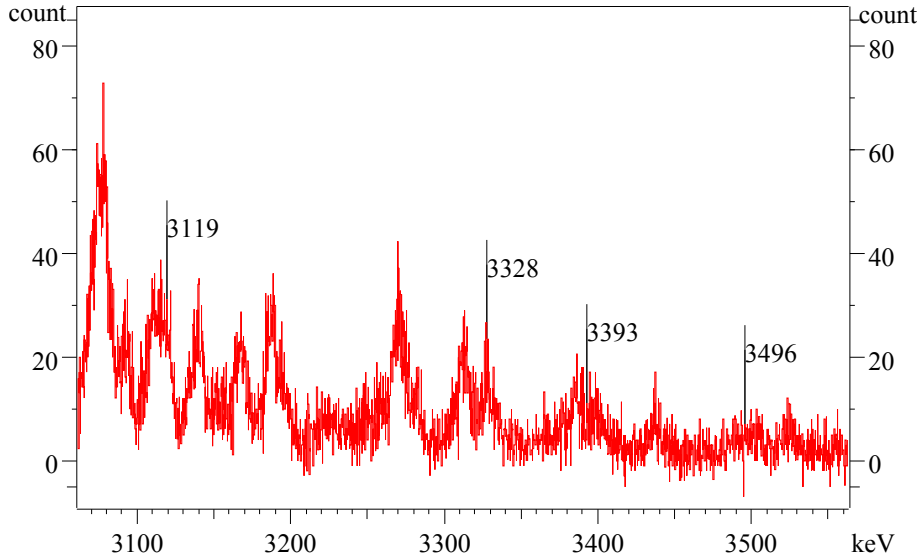

Figure 3.18: γ-spectrum in the energy range between 3.1 MeV and 3.5 MeV after applying a p-gate from 3.6 MeV up to 4.2 MeV together with a γ-gate on the 633 keV peak of the 2_1^+-state. Note, that no peak fits are shown, as the energy calibration in this region is extrapolated and results in deviations. The vertical lines thus only mark certain energy values of γ-rays which are believed to stand on the 2_1^+-state.

The 3126 keV Level Two new transitions were found, which initially were associated to the 3128 keV level in this work. A $3126\,\mathrm{keV} \xrightarrow{2493\,\mathrm{keV}} 2^+$transition and a $3126\,\mathrm{keV} \xrightarrow{748\,\mathrm{keV}} 3^-$ transition (see Table 3.1). The 2493 keV γ-ray can also be observed in the $(n, n'\gamma)$-experiment, but is published nowhere [29].

However the 3128 keV level has a spin assignment of 7^+, according to [41]. That work examined the β^+/EC decay of ^{106}In where multipolarities in ^{106}Cd have been determined according to the best match of conversion electron coefficients to theoretical values. In [49], it was found, that the 3126 keV level is directly fed from the 7^+ ground state of ^{106}In by the β-decay. A negative parity spin of 7^- was assigned to this level in that work. In [45] γ-ray angular distributions were examined. In

common with the other works a positive parity spin of 7^+ was found there. Thus a spin of 7^+ can be considered as valid for the 3128 keV level. This in turn implies a $7^+ \overset{2493\,keV}{\rightarrow} 2^+$ and $7^+ \overset{748\,keV}{\rightarrow} 3^-$ for the newly found transitions, which is very unlikely according to the γ-transition selection rules.

Therefor it is assumed, that a level doublet exists with a slightly lower energy value. A spin range of $1-4$ has been assigned to this newly discovered 3126 keV level.

The 3128 keV Level Two transitions, 624 keV and 634 keV, are stated to depopulate this level [1]. The 634 keV transition, given in the literature, could not directly be observed. This transition is only given in [49], where the level scheme was determined on the basis of energy and intensity balance arguments, whereas information about $\gamma\gamma$-coincidences were taken from other references therein.

As the $2_1^+ \overset{633\,keV}{\rightarrow} 0_1^+$ transition is the depopulating transition of the lowest excited 2_1^+ level in ^{106}Cd, it is part of many γ-cascades. In the γ-spectra of ^{106}Cd fractions of this peak are almost always present and nearly impossible to clear from the γ-spectrum by a p-gate. Therefore the 633 keV line covers completely a possible 634 keV line, making it impossible to fit a 633 keV/634 keV doublet directly. A combination of a p-gate with a gate on an intermediate γ-ray in any cascade involving the 633 keV/634 keV doublet does not resolve this issue. Thus no energy value could be extracted. Anyhow an existing 634 keV line will produce some self-coincident counts in the gated γ-spectrum, when a gate is set to the 633 keV peak. These counts in turn represent the relative intensity of the 634 keV transition, which serves as a proof for existence of that transition. To check that, a p$\gamma\gamma$-matrix was used, with a p-gate of 100 keV width set to the level energy of 3128 keV. Combined with a γ-gate set to 633 keV the relative intensity of a possible 634 keV transition could be extracted. Whereas for the branching ratio the intensity of the 624 keV transition could directly be gained from the p-gate alone. The extracted branching ratio for the γ-rays 624 keV : 634 keV is 100.0(70) % : 55.0(41) %. This is in excellent agreement to the literature values of 100(10) % : 55(6) % [1].

Anyhow, even without the existence of a 633 keV/634 keV doublet some self-coincident counts of 633 keV are expected to be present, stemming from random coincidences registered in the DAQ, due to a high rate of 633 keV events. When a back scattered particle triggers an event in the Si-detectors, a time window is opened in the DAQ. This supplies some probability for a γ-ray, stemming from a different scattering event to be falsely associated to the initial trigger event. This probability of random coincidence is expected to be not neglectable for $2_1^+ \overset{633\,\mathrm{keV}}{\rightarrow} 0_1^+$transition, as this is, as already mentioned, the most dominant transition in this reaction. Therefore the 633 keV level, as the lowest exited state in ^{106}Cd, is expected to be excited even when particles are not scattered to backwards directions, as it is most probable for a scattering particle to supply sufficient energy and angular momentum to the target nucleus to meet the conditions for this level excitation. It has thus to be taken account of this effect when a γ-gate is set to a doublet at 633 keV. To get an estimate of such random self-coincidences of the $2_1^+ \overset{633\,\mathrm{keV}}{\rightarrow} 0_1^+$ transition, the 633 keV peak has been self-gated combined with a particle gate of 100 keV set to

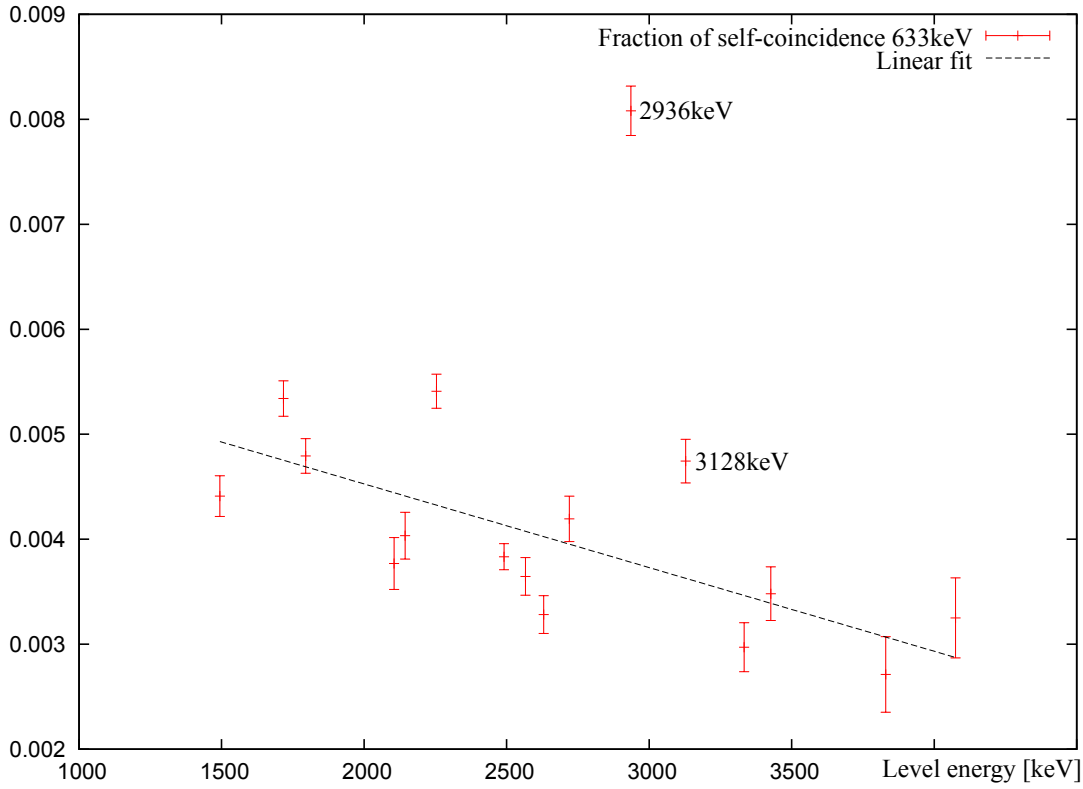

Figure 3.19: The fraction of self-coincidence of the 633 keV peak followed over some selected level energies.

some selected level energies. It is mentioned as a side note, that it is not applicable to measure the self-coincidence of the 633 keV peak with a p-gate set directly to the 633 keV level. As a multiplicity of 2 γ-rays is required for the p$\gamma\gamma$-matrix, the amount of background γ-rays in the matrix is enhanced when a p-gate is set to the lowest energy level as the nucleus can only deexcite via 1 γ-ray. It can be seen from Figure 3.19, that the fraction of self-coincidence of the 633 keV peak shows a trend of linear regression with increasing level energy. One can also see from Figure 3.19, that the p-gate set to 2936 keV breaks that trend and reveals some extra self-coincident counts, whereas the p-gate set to the 3128 keV level obeys the general trend of linear regression. Therefore it is assumed, that the depopulating 634 keV transition of the 3128 keV level, stated in [49], does not exist. It is rather assumed that the 2936 keV has a deexciting 631 keV transition. The relative intensity of this transition can be obtained by the fraction of counts of the 633 keV peak stemming from the self-gate, shown in Figure 3.19, subtracted by the random coincident counts of the $2_1^+ \overset{633\,\mathrm{keV}}{\rightarrow} 0_1^+$transition, which are approximated by the linear fit. The error of the approximated value stems from the standard derivation of the residuals to the linear fit (1σ confidence level). The error of the counts for the 2936 keV $\overset{631\,\mathrm{keV}}{\rightarrow}$ 2305 keV transition are obtained from the law of error propagation combined with the error of the linear approximation and the error of the fit of the self-gate. The results can be seen in Table 3.1. Note that the energy value of this transition was not directly measured, it is instead calculated from the energy difference of the involved levels.

As a crosscheck for the existence of the 2936 keV $\overset{631\,\mathrm{keV}}{\rightarrow}$ 2305 keV transition the intensity balance of some cascades have been studied and compared to the 2936 keV $\overset{631\,\mathrm{keV}}{\rightarrow}$ 2305 keV$\overset{811\,\mathrm{keV}}{\rightarrow}$ 1495 keV$\overset{861\,\mathrm{keV}}{\rightarrow}$ 633 keV$\overset{633\,\mathrm{keV}}{\rightarrow}$ 0 keV cascade. The other cascades have to involve the $2_1^+ \overset{633\,\mathrm{keV}}{\rightarrow} 0_1^+$transition and two feeding transitions stacked on top of each other. The upper transition of such three γ-rays of each cascade, was used for the γ-gate, so that for the following two γ-rays the intensities have to be equal to each other after efficiency correction. Three cascades were found, where the upper γ-ray was sufficiently clear to gate on, i. e. no doublet and clearly visible in the singles. For the cascade 3073 keV $\overset{819\,\mathrm{keV}}{\rightarrow}$ 2254 keV$\overset{1621\,\mathrm{keV}}{\rightarrow}$ 633 keV$\overset{633\,\mathrm{keV}}{\rightarrow}$ 0 keV and a γ-gate set to 819 keV the relative intensities of the γ-rays 1621 keV : 633 keV were found to be 98(12) % : 100(14) %. For the cascades 3328 keV $\overset{1074\,\mathrm{keV}}{\rightarrow}$ 2254 keV$\overset{1621\,\mathrm{keV}}{\rightarrow}$ 633 keV$\overset{633\,\mathrm{keV}}{\rightarrow}$ 0 keV and 3372 keV $\overset{1024\,\mathrm{keV}}{\rightarrow}$ 2348 keV$\overset{1715\,\mathrm{keV}}{\rightarrow}$ 633 keV$\overset{633\,\mathrm{keV}}{\rightarrow}$ 0 keV and γ-gates set to 1074 keV and 1024 keV the relative intensities of the γ-rays 1621 keV : 633 keV and 1715 keV : 633 keV were found to be 95.5(78) % : 100.0(79) % and 100(12) % : 99(13) % respectively. These intensities agree with each other as expected. For the initially mentioned cascade starting at the 2936 keV level and a γ-gate set to the 811 keV peak it was found, that the relative intensities of the γ-rays 861 keV : 633 keV are 73.1(46) % : 100.0(61) %, reveling an increased intensity of the 633 keV peak, which is a clear hint for a doublet of that peak. This in turn proofs that a 631 keV γ-ray is standing on top of the 2305 keV level.

The 3132 keV Level This level was newly discovered in this work, see Table 3.1 for details. Note that the 641 keV line forms a doublet with the one associated to the 3019 keV level. The FWHM of level excitations in the p-spectra is in the order of $\sim$100 keV, resulting in difficulties in level assignments of γ-rays from the p-spectra alone. A clear identification of a doublet in such cases is possible via a γ-gate set to the proper γ-ray from below, i. e. the 998 keV line in the cascade 3132 keV $\overset{641\,\mathrm{keV}}{\rightarrow}$ 2492 keV$\overset{998\,\mathrm{keV}}{\rightarrow}$. The spin of this level is assumed to be $4-7$.

The 3198 keV Level The 3198 keV $\overset{1704\,\mathrm{keV}}{\rightarrow}$ 1494 keV transition has been observed for the first time in this work, proving, that the former placement of the 1704 keV transition in the literature [1, 45] was wrong. See the discussion about the 2339 keV level. The possible spin of this level ranges from 2 to 6.

The 3214 keV Level Besides the 1498 keV transition, the 836 keV transition was discovered, belonging to this new level. Together with the 837 keV line of the 2331 keV level and the 835 keV line of the 2630 keV level, the 836 keV line of this level forms a triplet in the γ-singles spectrum. See also the discussion about the 2630 keV level. The spin of this level is $1-4$ according to the selection rules.

The 3222 keV Level In [27, 44] the 1427 keV and the 2590 keV transition have been published for the first time. These transitions could be confirmed in this work. See Table 3.1. Note, that the 1427 keV line forms a doublet with the 1426 keV line of the 2920 keV state.

The 3235 keV Level A similar issue as with the 3093 keV level occurs here with respect to the branching ratios. The findings of this work are twisted relative to that of [39], where NNDC values are stemming from. In this work the branching ratio for the γ-rays 1519 keV : 2602 keV is 17.0(12) % : 100.0(46) %, whereas in [39] it is 100(13) % : 19(4) %. A search for extra components in the peaks has been conducted, in the same way as for the 3093 keV level, by looking for level excitations coincident to the γ-rays. No hints for doublet components could been found.

However the 2994 keV($J = (0^+)$) $\overset{1518\,\mathrm{keV}}{\rightarrow}$ 1476 keV($J = 2^+$) in ^{110}Cd has a γ-ray of similar energy [1]. The target composition used in [39] is given as 77.3 % for ^{106}Cd and 0.6 %; 3.9 %; 3.3 %; 5.6 %; 2.6 %; 5.7 %; 1.0 % for the heavier isotopes $^{108,110-114,116}$Cd. It is thus likely, that the 3.9% of ^{110}Cd in that target have been excited in the (n, n')-reaction used in [39], which led to the extra amount of intensity for the 1519 keV γ-ray.

The 3245 keV Level For this level a new depopulating line was discovered. The 3245 keV $\overset{993\,\mathrm{keV}}{\rightarrow}$ 2522 keV transition was found due to the feeder search of the 2252 keV level and forms a γ-doublet with the 992 keV line of the 2486 keV level. It was found, that this newly discovered 993 keV γ-ray is the most intensive line of this level. In the literature [39] the branching ratio is given as 63(12) % : 69(13) % : 100(16) % for the γ-rays 1141 keV : 1529 keV : 3244 keV. In this work relative intensities for 993 keV : 1141 keV : 1529 keV : 3244 keV were derived as 100.0(58) % : 13.2(15) % : 68.9(41) % : 93.9(63) %. The main deviation between these results concerns the 1141 keV transition.

In the discussion about the 3235 keV level the target composition used in the experiment of [39] was already mentioned. In ^{107}Cd a 1646 keV($J = n.a.$) $\overset{1140\,\mathrm{keV}}{\rightarrow}$ 505 keV($J = \frac{7}{2}^+$) transition (g.s. $J = \frac{5}{2}^+$) and in ^{111}Cd a 1972 keV($J = \frac{7}{2}^-$) $\overset{1141\,\mathrm{keV}}{\rightarrow}$ 831 keV($J = \frac{7}{2}^-$) transition (g.s. $J = \frac{1}{2}^+$) are known [1], which are likely to be excited in the (n, n')-reaction of Ref. [39]. (Note that ^{107}Cd is unstable but can be produced from ^{106}Cd via neutron capture. Note also, that for ^{108}Cd and ^{109}Cd each a γ-ray of 1142 keV is known, although less likely excitable in a (n, n')-reaction due to necessary higher spin spin transfer.) As argued before, it is assumed, that γ-rays stemming from other cadmium isotopes have been falsely added to the intensities of lines in ^{106}Cd in Ref. [39].

The 3284 keV Level The 793 keV transition stated in the literature [41], could not be observed. It was found, that this γ-ray was misplaced. Instead a 791 keV transition could be associated to the 2896 keV level, see also the discussion there. No spin is given for this level in the literature, which is here assumed to be $1-4$ on the basis of selection rules.

The 3286 keV Level This new level has been deduced via the observation of a 568 keV and a 907 keV transitions. The latter forms a doublet with the 909 keV line of the 3539 keV level. There is also evidence for a level at 3286 keV in the data of the $(n, n'\gamma)$-experiment, which has not been published yet [29], though a different

deexciting transition has been observed there. A spin of $1-4$ is assumed for this level.

The 3320 keV Level In Ref. [45] a 400 keV transition ($I_\gamma = 6.1(13)$ [1]) to the 2921 keV level is listed for this level. This line could not be observed with a γ-gate from below on the 1427 keV peak. It is likely, that this state was not populated sufficiently by the (p,p')-reaction, due to the relative high spin of $J = 6^-$ [1]. The other two known depopulating transitions were observed (see Table 3.1)

The 3323 keV Level For this level two new transitions were observed. See Table 3.1 for details. Due to the observation of the 3323 keV $\overset{1829\,\mathrm{keV}}{\rightarrow}$ 4_1^+ transition the spin assignment of 1^+, 2^+, 3^+ given in the literature [1] can unambiguously be reduced to 2^+, 3^+ .

The 3328 keV Level 5 new transitions have been observed for this level (see Table 3.1). The 1834 keV transition among these forms a doublet with the 1836 keV line of the 2468 keV level. The new 860 keV transition forms a doublet with the 861 keV line decaying from the 4_1^+-state. This situation is described in detail in the paragraph about the 2468 keV level, see also the discussion there. Due to the newly discovered transitions to 4^+-states, the literature spin range of 1, 2^+ has been reduced to 2^+.

As can be seen from Figure 3.8, the 1834 keV transition of this level is standing on the 4_1^+-state. A gate from below on the 861 keV peak, thus does not result in an exact energy value for the 1834 keV transition, as in that case the 860 keV peak of this level is within the gate, which in turn is standing on the 1836 keV line of the 2468 keV level. A gate set to the 860 keV/861 keV peak, therefore is a gate on a doublet, which in turn produces the 1834 keV/1836 keV doublet in the resulting spectrum. One way to solve this situation is to extract the γ-energies of the lower energy components of the doublets by setting a p-gate to each of the lower levels and a γ-gate from below in a p$\gamma\gamma$-matrix. These initially extracted values can then be set fixed in the doublet fit with the unknown energy of the higher component left as a free parameter. Figure 3.20 shows as, an example for this method, the extraction of the γ-energy of the 1834 keV peak, which is left as the only free parameter in that fit. The spectrum was generated by a p-gate of 100 keV width set to a level energy of 3330 keV. The energies of the 1830 keV line (3323 keV level) and the 1840 keV line (3333 keV level), could be extracted before via a γ-gate from below on the 861 keV peak. The same way was the energy of the 1836 keV line extracted before, by gating from below on the 633 keV peak with a p-gate set to the 2468 keV level. This fit has also been used to extract the count rate of the 1834 keV line for the determination of relative intensities. (The FWHM were all fitted by the same value for each peak by the fitting program.)

The literature branching ratio in NNDC is stemming from [39]. For the γ-rays 981 keV : 2695 keV : 3327 keV it is given as: 65(11) % : 100(14) % : 50(9) %, whereas in this work it was found to be 56.0(59) % : 100(12) % : 19.3(19) % . (Keep in mind the calibration deficiencies above 2.3 MeV, e.g. for the 3327 keV g.s. transition.) The main deviation occurs in the intensity of the 3327 keV γ-ray. Figure 3.21 shows, that there is a higher level excitation coincident to this γ-ray. Together with the

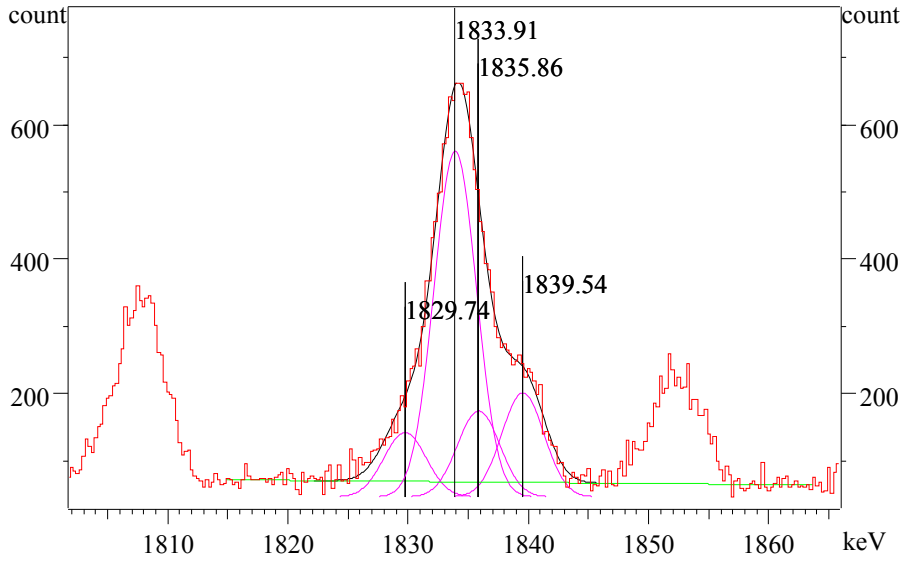

Figure 3.20: Fit of the 1834/1836 keV doublet and neighboring lines. The 1834 keV peak has been left as the only free parameter for an extraction of the γ-energy as well as the count rate.

information of Figure 3.18, where certain γ-rays are indicated that have been found coincident to the $2_1^+ \rightarrow 0_1^+$ transition, it is proven, that a $\sim 3961\,\mathrm{keV} \overset{\sim 3328\,\mathrm{keV}}{\rightarrow} 633\,\mathrm{keV}$ transition exists, which forms a doublet with the 3327 keV ground state transition. If this higher component is not separated, like done in this work with a p-gate set to the 3328 keV level energy, the intensity of the 3327 keV γ-ray of this level will be overestimated. (Note, that a $3842\,\mathrm{keV}(J = n.a. \overset{3328\,\mathrm{keV}}{\rightarrow} 513\,\mathrm{keV}(J = 2^+)$ is also present in ^{116}Cd, which is present in the target of [39] with an abundance of 1% and can be excited via a (n, n')-reaction.)

The$\sim 3961\,\mathrm{keV} \overset{\sim 3328\,\mathrm{keV}}{\rightarrow} 633\,\mathrm{keV}$ transition is not part of the results of Table 3.1, as discrepancies in the energy calibration above ~2.3 MeV do not provide reliable energy values in this case (see also the discussion about the 3119 keV level).

The 3329 keV Level, given in the literature Due to the difficulties in the γ -spectroscopy resulting from the 860/861 keV and the 1834/1836 keV doublets, described in the former paragraph, it is not unlikely to assume, there is a single 1835 keV γ-ray standing on the 4_1^+-state, when only γ-coincidences are taken into account, as stated in [39]. In this work it could be proven, that there is no singlet 1835 keV line in ^{106}Cd. Thus it is assumed, that the 3329 keV level formerly given in the literature [1], stemming from [39], does not exist.

The 3333 keV Level Two γ-rays were observed depopulating this newly discovered level, see Table 3.1. There is also evidence for the 1839 keV γ-ray in the $(n, n'\gamma)$-experiment data [29]. Figure 3.20 shows a fit of this line together with neighboring γ-rays. The 1028 keV line forms a triplet together with the 1029 keV line from 2825 keV level and the 1027 keV line of the 3358 keV level within the 4 MeV level energy range of this work. This deexciting transition of this level could clearly be

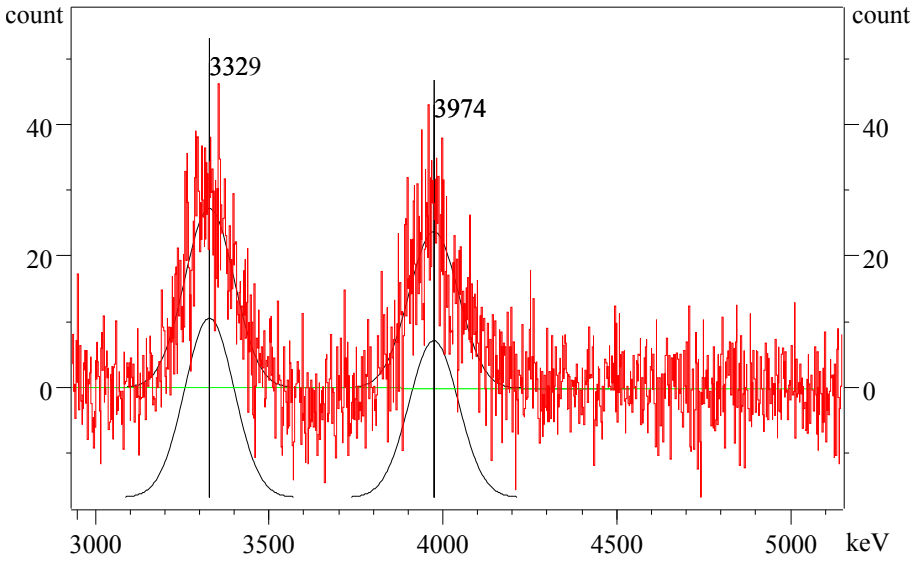

Figure 3.21: Particle spectrum with fits of level excitations after gating on the 3327 keV γ-peak. (Energy uncertainty $\pm$10 keV.)

identified via a p-gate set to 3000 keV - 3600 keV and a γ-gate set to the 811 keV γ-transition from below. With the information given in the literature [1] about similar energy depopulation transitions from the 4816 keV and 5822 keV levels, the 1028 keV peak might also be considered as a quintuplet. Of course depending on the population of these levels in the reaction. The spin of this level is assumed to be $2-6$.

The 3354 keV Level, given in the literature With a p-gate set to a range of 3200 keV - 3500 keV combined with a γ-gate from below on the 998 keV peak in a p$\gamma\gamma$-matrix, only the 861 keV line of the 4_1^+-state could be observed with its exact energy value. It is thus possible that the 862 keV transition to the 2492 keV level and therfore the 3354 keV level do not exist as predicted in [50, 51, 53]. In [53] a 3354 keV $\overset{851\,\mathrm{keV}}{\rightarrow}$ 2503 keV transition was reported, which is not found in NNDC [1]. This transition was also not observed in this work.

The works [50, 51, 53] aim to study high spin states and make use of fusion evaporation reactions (^{94}Zr(^{17}O, $5n$)^{106}Cd@80&92 MeV, ^{76}Ge(^{34}S, $4n$)^{106}Cd@148 MeV and ^{98}Mo(^{12}C, $4n$)^{106}Cd@60 MeV) to obtain a compound nucleus with large angular momentum. Another explanation for the "absence" of this state in this data set is therefore, that this state is part of a γ-decay band and is thus more likely be populated from above, rather than directly excitated in the ^{106}Cd$(p,p')^{106}$Cd reaction studied here.

The 3358 keV Level The 1027 keV transition to the 2330 keV level is not listed in [1], but was already stated in [41] and could be confirmed here. Note that the 1027 keV line forms a triplet together with the 1029 keV line from 2825 keV level and the 1028 keV line of the 3333 keV level within the 4 MeV level energy range of this work. See also the discussion about the other relevant levels. A spin of $3-7$ is assigned to this state.

The 3367 keV Level Only the 875 keV transition to the 2492 keV level could be observed for this state. For maximum statistics a p-gate of 200 keV width was set in a pγ-matrix. A γ-gate from below on the 998 keV peak, set in a $\gamma\gamma$-matrix, however did not show the 875 keV line. According to the predicted branching ratios in [1] this is the strongest line. It is thus assumed, that the population probability via a $(p, p'\gamma)$-reaction is too low for a sufficient spectroscopy, as publications, which observed this state used the β-decay of ^{106}In [41] or compound reaction like ^{104}Pd$(\alpha, 2n\gamma)^{106}$Cd [47] or (HI, xn) [51, 45] for the observation of the 283 keV (12.7(9) %), 323 keV (15.4(7) %) and 864 keV (23(9) %) γ-rays [1].

The 3372 keV Level Three γ-rays were found for this newly discovered level, see Table 3.1 for details. The data of the $(n, n'\gamma)$-experiment provide evidence for a level at this energy, although a different γ-ray was observed there [29]. The spin of this level was set to $1 - 4$.

The 3372 keV $\xrightarrow{654.1\,\text{keV}}$ 2718 keV transition forms a doublet with the 2371 keV $\xrightarrow{653.9\,\text{keV}}$ 1717 keV transition. Due to the close energy values of these γ-rays, the usual method used in this work for the extraction of branching ratios via a p-gate set to the level energy combined with a multiplet fit with fixed energy values was not applicable. As the typical FWHMs of level excitations in the p-spectra are in the range of ~180 keV, a p-gate of 100 keV width set centered on the 3372 keV level will also contain contributions stemming from the 3482 keV and 3119 keV levels. It can be seen from Figure 3.22, that this "p-gate contamination" results in feeding to the 2371 keV level, which produces a non-neglectable amount of the 2371 keV $\xrightarrow{653.9\,\text{keV}}$ 1717 keV transition in the doublet peak. Thus, to get an estimate of the fraction of the lower energetic component in the 653.9/654.1 keV doublet peak (red color), the 1738 keV line (I_γ = 100.0(41) %) (green color) of the 2371 keV level was fitted in the p-gated γ-spectrum. Together with the known branching ratios of the 2371 keV level it was possible to reproduce the related amount of counts of the 2371 keV $\xrightarrow{653.9\,\text{keV}}$ 1717 keV transition (I_γ = 33.2(15)%) within that peak. The for-

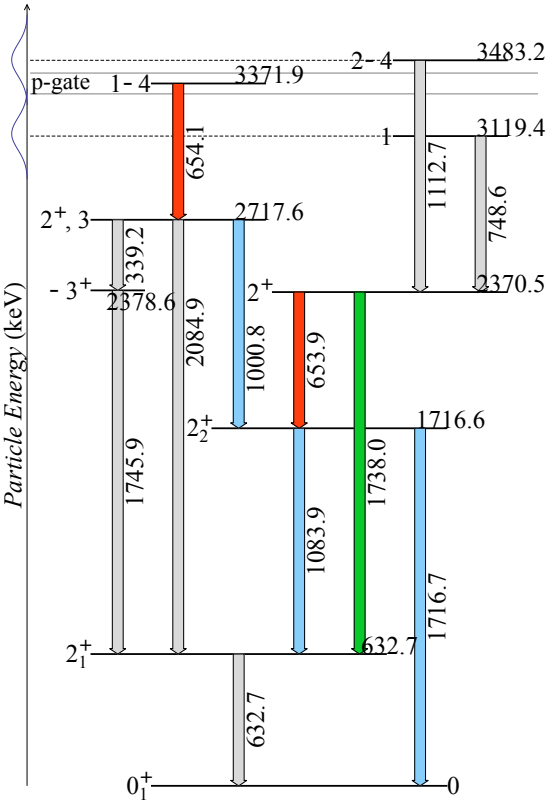

Figure 3.22: Partial level scheme with a focus on levels involved in depopulating via the 654 keV doublet. (Note that the depopulating 483 keV and 1024 keV transitions of the 3372 keV level are not shown, to keep the picture more clear.)

mula used to calculate these counts is:

$$\text{Counts}(653.9) = I_\gamma(653.9)\cdot\text{Counts}(1738)\cdot\text{Efficiency}(653.9)/\text{Efficiency}(1738)\,. \quad (3.3)$$

Whereas errors were calculated from the law of error propagation. Afterwards the calculated 653.9-component was subtracted from the 653.9/654.1 keV doublet peak intensity in the p-gated γ-spectrum. The same p-gated γ-spectrum was then used to fit the 483 keV and 1025 keV γ-ray of this level for the calculation of branching ratios.

It should be mentioned as a side note, that a γ-gate set from below for the measurement of the 2371 keV $\overset{653.9\,\text{keV}}{\rightarrow}$ 1717 keV transition energy value will result in a contribution of 3372 keV $\overset{654.1\,\text{keV}}{\rightarrow}$ 2718 keV transition, as one can see from the blue colored transitions in Figure 3.22. Setting a p-gate to the 2371 keV level is thus important.

The 3393 keV Level This level, only stated in Ref. [39] with just one ground state transition, was also observed with the HORUS-experiments in [27], where two additional transitions from this level were observed. These transitions could be confirmed in this work. However the energy values for these lines extracted here are slightly lower than quoted in Ref. [27]. The deviation of energy values for high energy γ-rays due to deficiencies in the energy calibration above ∼2.3 MeV have already been discussed in the beginning of this section. Nevertheless a discrepancy of ∼1 keV was still found for the γ-ray of the 3393 keV $\overset{1676\,\text{keV}}{\rightarrow}$ 1717 keV transition, which in turn leads to a slightly lower energy value for this level in this work, as only γ-rays below ∼2.3 MeV were considered for the calculation of level energies. The branching ratios extracted here also show some discrepancies to Ref. [27], where those values were found to be I_γ =7(3) % : 14(3) % : 100(3) % for the γ-rays 1677.0 keV : 2761.0 keV : 3393.7 keV, whereas here they are I_γ =30.9(21) % : 60.1 (30)% : 100.0(48) % for 1676.0 keV : 2757.9 keV : 3391.4 keV.

Similar to the situation with the 3119 keV level, it was found that the 3393 keV ground state transition forms a doublet with a transition standing on the 2_1^+-state (see also the discussion about the 3119 keV level). Figure 3.23 shows the higher component of the 3393 keV peak in the p-spectrum after putting a γ-gate to the 3393 keV peak. Together with the information already shown in Figure 3.18 it was found that a ∼ 4026 keV $\overset{\sim 3393\,\text{keV}}{\rightarrow}$ 633 keV transition exists, which can lead to an "over counting" of the 3393 keV line, if the higher energetic component is not separated from the lower one in the γ-peak fit. Thus, the same arguments as already mentioned in the discussion of the 3119 keV level hold here too. An overestimation in the count rate of the 3393 keV line will result in lower relative intensities of the other depopulating γ-rays, which explains the discrepancies in the branching ratios to [27].

Note, that the∼ 4026 keV $\overset{\sim 3393\,\text{keV}}{\rightarrow}$ 633 keV transition is not part of the results of Table 3.1, due to deficiencies in the energy calibration above ∼2.3 MeV (see also the discussion about the 3119 keV level).

In Ref. [27] the 3393 keV level is marked as a $J = 1$ state, whereas in the literature [1] it is $J = 2^+$. Therefore this state is denoted here as a spin $J = 1,\ 2^+$ state.

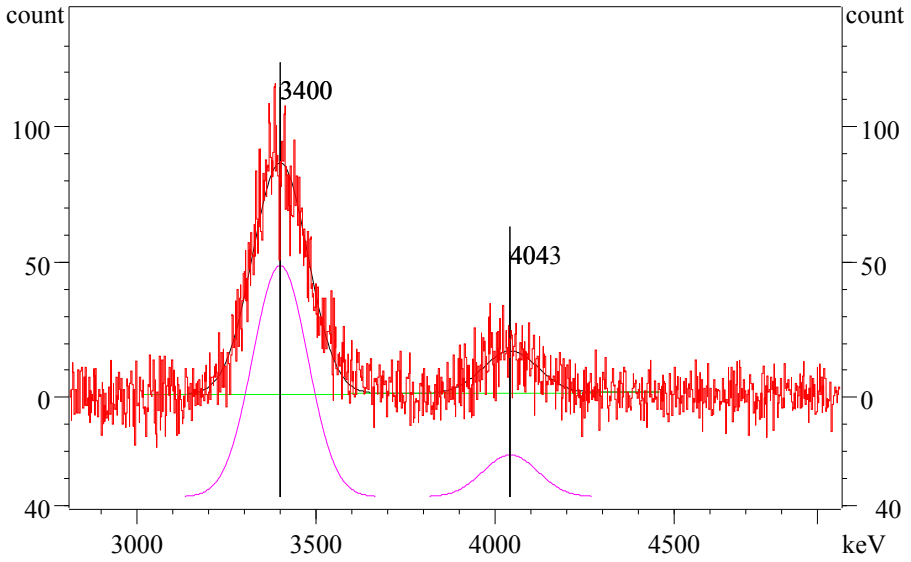

Figure 3.23: Particle spectrum with fits of level excitations after gating on the 3393 keV peak. (Energy uncertainty ±10 keV.)

The 3410 keV Level, given in the literature Although this level is stated in the literature several times [47, 51, 45], it could not be observed in this work. Each of the γ-rays 488 keV, 780 keV, 908 keV and 918 keV stated for this level, could not be observed with an appropriate γ-gate from below. Moreover, it could be shown, that the 488 keV γ-ray is depopulating the 2793 keV level and the 907 keV/909 keV doublet belongs to the 3286 keV and the 3539 keV level respectively (see the corresponding discussion paragraphs). The 780 keV line has very weak statistics in the singles spectra and could only be associated to the 3284 keV level in common with the literature [1], whereas the 918 keV line could not even be observed in the singles. It is thus concluded, that this level does not exist, or has not been populated sufficiently in the (p, p')-reaction, due to the relatively high $J = 7^-$ [1] spin.

The 3428 keV Level The 3428 keV $\overset{1933.9\,\mathrm{keV}}{\rightarrow}$ 1494 keV transition was newly discovered for this level. However, for the extraction of branching ratios, this line is very close to the 1933.6 keV transition depopulating the 2566 keV level. Since side feeding to the 2566 keV level from within a p-gate can not be excluded, it has to be accounted for a possible contribution from this γ-doublet to this peak. A p-gate of 100 keV width set to the 3428 keV level does also not eliminate the 1929 keV peak from the resulting γ-spectrum, which makes a proper fit even more complicated. As other transitions depopulating the 2566 keV level are too low in statistics due to weak relative intensities (see Table 3.1), the method of fitting a competing depopulating transition to the 1933.6 keV line and making use of known branching ratios of the 2566 keV level from which in turn the lower energy doublet component could be calculated, was not possible here. (See the paragraph of the 3372 keV level, where this method is applied to the 654 keV line).

Figure 3.24 gives an overview of the relevant partial level scheme. It can be seen, that a γ-gate from below for each component of the 1933.6 keV/1933.9 keV doublet i.e. gating on the 633 keV (green color) and the 861 keV peak (green color),

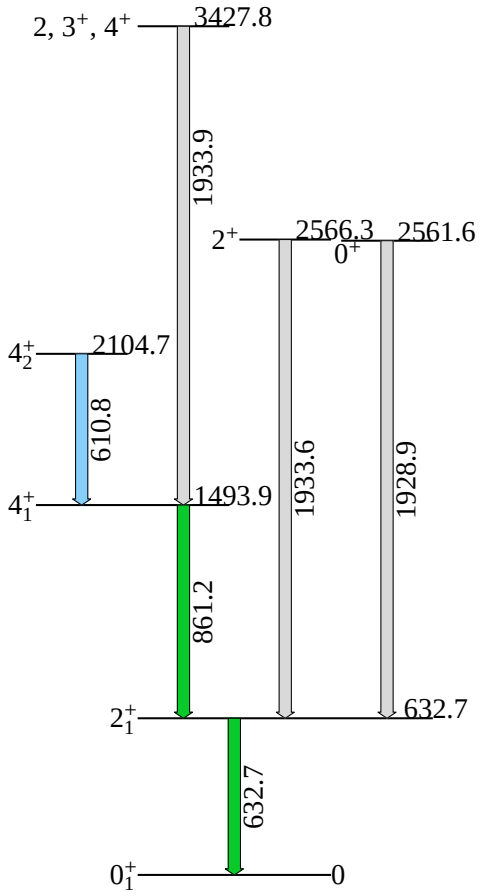

Figure 3.24: Partial level scheme of the 3428 keV and the 2562 keV, 2566 keV levels, to sketch the γ-cascades of the 1934 keV doublet.

will, in both cases, result in the presence of the 611 keV line (blue color) of the 2105 keV level. Since no line between the 3428 keV and the 2105 keV states was observed, the feeding to the 2105 keV level must be due to the 3245 keV $\overset{1141\,\mathrm{keV}}{\rightarrow}$ 2105 keV transition (and possible other unknown side feeding), as this line is still observed after setting a p-gate to the 3428 keV level combined with the described γ-gates from below within a p$\gamma\gamma$-matrix. Thus, using the same p-gate, the 611 keV peak is considered an "uninvolved spectator" to both cascades and it can be used to normalize the pγ-gated spectra of both doublet components. This way, it is taken account for the change of count rates stemming from the γ-gate, while at the same time the Q-value is preserved. After normalization, the fraction of the higher energy component within the doublet can directly be measured from the 861 keV gated spectrum. By keeping the same p-gate for the extraction of branching ratios, the measured lower energy doublet component can then simply be subtracted from the 1933.9 keV peak fit. See the results in Table 3.1.

The 3473 keV Level, given in the literature This level only stated in [41] with depopulating γ-ray of 981 keV, 1142 keV and 1979 keV could not be observed here. A γ-gate from below set to the 998 keV peak of the 2491 keV level did not show the 981 keV line. The 981 keV γ-ray could only be associated to the 3328 keV level (according to the literature [1]). The same situation occurs with the previously reported 1979 keV line, which is not visible in the γ-singles spectrum, as well as in the γ-spectrum after setting a γ-gate to the 861 keV line of the 4^+_1-state from below. Repeating this procedure of gating from below with a γ-gate set to the 226 keV peak ($I_\gamma = 100.0(42)\%$) of the 2331 keV level there is a weak coincidence with a 1142 keV line, as can be seen from Figure 3.25. Figure 3.25 also shows, that there is no coincidence with the 837 keV γ-ray ($I_\gamma = 37.9(20)\%$) of the same 2331 keV level. This result suggests, that no 3473 keV $\overset{1142\,\mathrm{keV}}{\rightarrow}$ 2331 keV transition exists, although the 837 keV line could simply miss statistics due to the lesser intensity. On top of that it was found, that the coincidence of the 226 keV peak to the 1142 keV peak stems from a Compton-scattering event of a 1369 keV γ-ray from one detector to another. After

setting a γ-gate to that 1369 keV line, the p-spectrum did not show level excitations coincident with this peak, revealing, that this line does not stem from the target material. The origin of this 1369 keV peak however could not be identified, although a similar energy is seen in $^{55,56,57}Fe$ and ^{55}Co according to the literature [1]. (A $^{56}\mathrm{Fe}(p,2n)^{55}\mathrm{Co}\xrightarrow{\beta}{}^{55}\mathrm{Fe}$ reaction is possible, if the proton beam hits steal of the beam line.) Note, that the 3245 keV $\overset{1141\,\mathrm{keV}}{\rightarrow}$ 2105 keV and the 3328 keV $\overset{981\,\mathrm{keV}}{\rightarrow}$ 2348 keV are proven to belong to ^{106}Cd in this work. It is thus assumed, that these transitions are misplaced in Ref. [41], due to missleading $\gamma\gamma$-coincidence measurements.

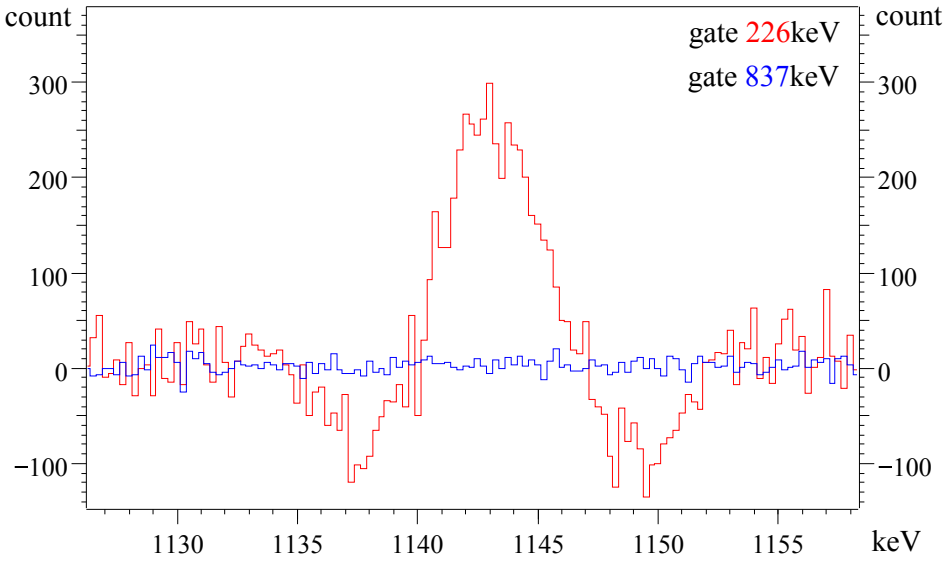

Figure 3.25: Overlay of the 226 keV (red) and 837 keV (blue) γ-gated γ-spectra. Only the 226 keV gate shows a coincidence to a 1142 keV peak, which is Compton-scattering of a 1369 keV.

The 3483 keV Level The 3483 keV $\overset{1113\,\mathrm{keV}}{\rightarrow}$ 2371 keV as well as the 3483 keV $\overset{1989\,\mathrm{keV}}{\rightarrow}$ 1494 keV transitions were newly observed, which justify the existence of this new level (see Table 3.1). The suggested spin is $2-4$.

The 3489 keV Level This new level was observed via the newly discovered 3489 keV $\overset{772\,\mathrm{keV}}{\rightarrow}$ 2717 keV and 3489 keV $\overset{1996\,\mathrm{keV}}{\rightarrow}$ 1494 keV transitions (see Table 3.1). A spin of $2-4$ is assumed.

The 3496 keV Level In the literature [41, 43] only a ground state transition and a transition to the 2_1^+-state were known about this level. In [27] four new γ-rays were observed for this level. Three of them could be confirmed here, whereas the depopulating 1699 keV transition ($I_\gamma = 0.7(3)$ [27]) was not observed. On the other hand, a new 3493 keV $\overset{1243\,\mathrm{keV}}{\rightarrow}$ 2252 keV depopulating transition was discovered in this work. Similar issues as with the 3393 keV level occur here concerning γ-ray energies. Whereas γ-rays of the 3393 keV level were $\sim$1 keV lower in this work compared to [27], they are $\sim$1 keV higher for the 3496 keV level here, compared to [27], which also

results in a higher energy value for this level in this work. (It is again emphasized, that only γ-rays below $\sim$2.3 MeV have been considered for the calculation of level energies.) In Ref. [27] the spin is assigned as $J = 1$, whereas the literature value is $J = 1, 2^+$. Due to the newly discovered 3496 keV $\overset{1243\,\mathrm{keV}}{\rightarrow}$ $3^+, (4^+)$ transition (3^+-assignment stems from [27]), the spin is kept as $J = 1, 2^+$.

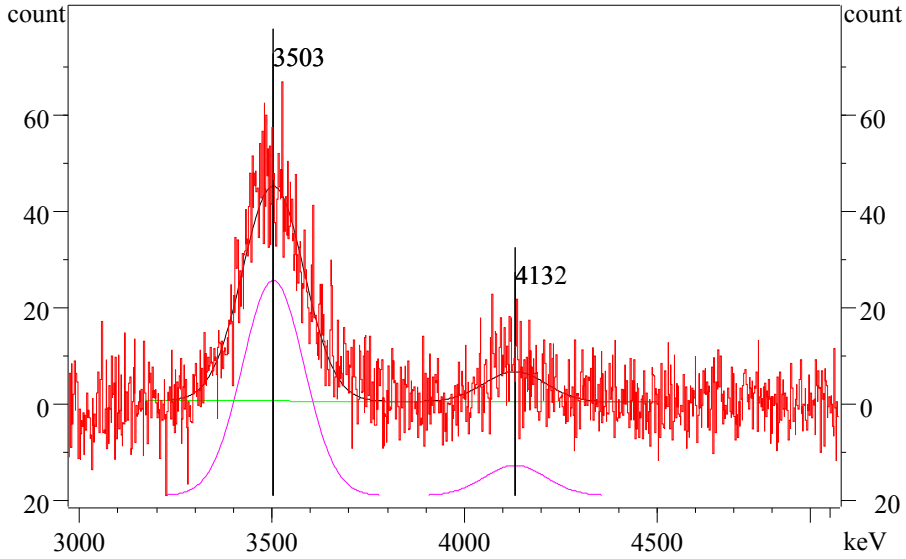

Figure 3.26: Particle spectrum with fits of level excitation energies after gating on the 3496 keV γ-peak. (Energy uncertainty $\pm$10 keV.)

The branching ratios given in the literature [1], stemming from [43] for the γ-rays 2862 keV : 3495 keV are 70(4) % : 100(4) %. In [27] the branching ratios for the 5 γ-rays 928.3 keV : 1147.2 keV : 1778.0 keV : 2861.7 keV : 3494.3 keV are given as 2(1) % : 6(2) % : 15(4) % : 58(3) % : 100(3) %. These results differ to the findings of this work, where for the 6 γ-rays 929.3 keV : 1148.0 keV : 1243.3 keV : 1778.7 keV : 2861.2 keV : 3492.1 keV branching ratios as 8.0(10) % : 63.4(39) % : 65.5(40) % : 57.3(35) % : 100.0(51) % : 87.9(45) % were derived. The main discrepancy in these results surely concerns the question about the most intense γ-ray, as in the other works this is considered the 3495 keV line, but in this work the 2861 keV line has a relative intensity of 100.0(51) %.

Similar to the 3119 keV and the 3393 keV levels, these discrepancies can be explained by an unregistered higher energy component of the 3496 keV peak in the other works (see also the discussions about the 3119 keV and 3393 keV level). Figure 3.26 shows the p-spectrum after gating on the 3492 keV γ-peak, revealing that this peak is coincident with an excitation of a higher energetic level. Together with the information of Figure 3.18, it is obvious, that a $\sim$ 4129 keV $\overset{\sim 3496\,\mathrm{keV}}{\rightarrow}$ 633 keV transition exists. Thus the 3496 keV peak is a doublet, which leads to an over estimation in the intensity for this line in the other works.

Similar to the situation of the 3119 keV and 3383 keV level, the$\sim$ 4129 keV $\overset{\sim 3496\,\mathrm{keV}}{\rightarrow}$ 633 keV transition is not part of the results of Table 3.1, as discrepancies in the energy calibration above $\sim$2.3 MeV do not provide reliable energy values in this case (see also the discussion about the 3119 keV level).

The 3498 keV Level The observation of the 3498 keV $\overset{2004\,\mathrm{keV}}{\rightarrow}$ 1494 keV transition led to the discovery of this new level. The spin of this state is stated as $J = 2 - 4$.

The 3507 keV up to the 3902 keV Levels, given in the literature Each depopulating transition of the levels in the energy region from 3.5 MeV up to 4 MeV, stated in the literature [1], has been checked by an appropriate γ-gate from below, to extract an energy value of the γ-ray. Only the 3547 keV $\overset{1217\,\mathrm{keV}}{\rightarrow}$ 2331 keV transition could be observed by this method (see Table 3.1), but no evidence for the 3508 keV, 3544 keV, 3642 keV, 3679 keV, 3679 keV, 3698 keV, 3787 keV and 3902 keV. A deeper examination for reasons for this discrepancy to the findings in the literature (be it possible misplacements or the observation of background lines in other works or the lack of sufficient population of these levels with the used (p, p')-reaction) was beyond the scope of this work.

The 3539 keV Level Two new transitions have been discovered and established for this new level. Note, that the 908.8 keV line forms a doublet with the 907.2 keV line of the 3286 keV level, whereas the 1822.6 keV line forms a doublet with the 1821.1 keV (see Table 3.1 for details). In the data of the $(n, n'\gamma)$-experiment, there is also evidence for a level at this energy, although other γ-rays have been observed there [29]. The level spin is $J = 1 - 2$.

The 3725 keV Level This level was newly discovered via the 3725 keV $\overset{1377\,\mathrm{keV}}{\rightarrow}$ 2348 keV transition during the examination of the 1376 keV/1377 keV doublet. See also the discussion about the 3093 keV level for further details.

The 3830 keV Level The 3830 keV $\overset{1578\,\mathrm{keV}}{\rightarrow}$ 2252 keV transition was newly discovered, leading to the observation of this new level, with a spin of $J = 2 - 6$.

The 3917 keV Level This new level was discovered via the 3917 keV $\overset{1538\,\mathrm{keV}}{\rightarrow}$ 2379 keV transition for the first time in this work. A spin range of $J = 1 - 5$ was found for this state.

The 4001 keV Level The 1746.6 keV γ-ray of the 4001 keV $\overset{1748\,\mathrm{keV}}{\rightarrow}$ 2254 keV transition of this new level forms a doublet with the 1745.9 keV line of the 2379 keV level. The suggested spin range is $J = 1 - 4$.

The 4046 keV Level The γ-ray of the 4046 keV $\overset{1667\,\mathrm{keV}}{\rightarrow}$ 2379 keV transition could be associated to this new level. A spin of $J = 1 - 5$ is assigned to this state.

The 4075 keV Level As already stated, the 4075 keV $\overset{1821\,\mathrm{keV}}{\rightarrow}$ 2254 keV transition of this newly discovered level forms a doublet with the 1823 keV γ-ray depopulating the 3539 keV level. This level thus has spin $J = 1 - 4$.

4 Shell-Model Calculations and Comparison to experimental Data

4.1 The Nuclear Shell Model

The atomic nucleus is a quantum mechanical system consisting of nucleons, namely protons and neutrons, which attract each other by the strong nuclear force. This force is short ranged, predominantly of two-body character and strong enough to overcome the Coulomb repulsion of the protons.

As the nucleons are fermions, they obey the Pauli principle and thus distribute in the configuration space by distinguishing in one or more quantum numbers. These circumstances naturally lead to a system that forms shell structures for protons and neutrons separately. Due to the lack of a central field, like the nuclear core provides the Coulomb field for the atomic electron shell, the nuclear system is rather complex. Any particle excitation from one orbit to another directly influences the center of attraction for the other nucleons. To account for this fact, the nuclear Hamiltonian for A nucleons can be written as [25]:

$$H = \sum_{i=1}^{A} [T_i + U(r_i)] + \left(\frac{1}{2} \sum_{i,j=1}^{A} V_{i,j} - \sum_{i=1}^{A} U(r_i) \right) = H_0 + H_{res}. \tag{4.1}$$

This way, a central potential or mean field $U(r_i)$ is introduced and a one-body part H_0 of the Hamiltonian can be separated. The two-body potential $V_{i,j}$ is contained in the residual Hamiltonian H_{res}, which is considered a small perturbation of the independent particle Hamiltonian H_0.

The *Independent Particle Model* neglects H_{res}. By solving the Schrödinger equation $H_0\psi(r) = E_{nl}\psi(r)$ and assuming an harmonic oscillator potential or an even more realistic Wood-Saxon potential for $U(r_i)$ and demanding a spin orbit coupling, a grouping of orbitals by principal quantum number n and orbital spin l results, as shown in Figure 4.1. From this approach, the magic numbers 2,8, 20, 28, 50, 82, 126, after which a shell gaps occur, are well reproduced. However, for a more realistic reproduction of the conditions within a nucleus, it is essential to account for the *residual interaction* H_{res}, that all valence nucleons apply on each other.

The task of the *Nuclear Shell Model* is thus a most realistic microscopic description of the condition within a nucleus. Different approaches are at hand to account for the residual interaction H_{res} [25]. *Realistic interactions* attempt to determine the inter nuclear force from nuclear scattering events. However, these findings can not be directly incorporated into shell model calculations as they lack effects of the nuclear medium. The free nucleon-nucleon potential exhibits a strong repulsive core, which requires a renormalization or a cutt-off procedure, like the *Schematic interactions* are descriptions of radial part of the nuclear potential by most appropriate analytical expressions. The most common approach in computational shell-model calculations is however the use of *effective interactions*. The Schrödinger equation $H\psi(r) = E_{nl}\psi(r)$ with the Hamiltonian H from Equation 4.1 can be solved, when single particle energies $\varepsilon(j_i)$, eigenvalues of H_0, and two-body matrix elements $\langle j_1 j_2 | V_{12} | j_1 j_2 \rangle$, eigenvalues of H_{res}, are known parameters. The single particle and

the two-body matrix elements are usually best fits to experimental data or directly extracted from nucleon separation energies.

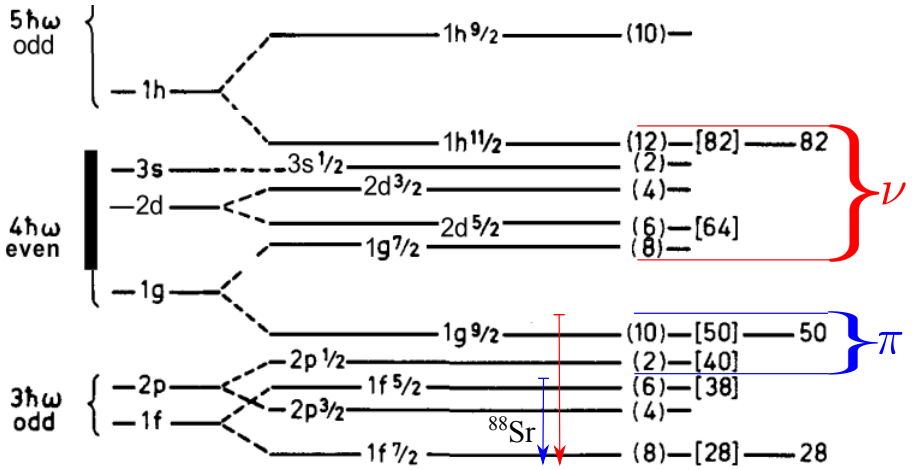

Figure 4.1: Partial energy scheme of single particle orbits ordered by relative energies, derived from the Independent Particle Model (modified figure adopted from [54]). Orbitals within brackets form the model space of the conducted shell-model calculations of this work, blue protons and red neutrons. Downward arrows indicate orbitals of the inert ^{88}Sr core with the same color code.

4.2 Shell-Model calculations of cadmium isotopes

Large-scale shell-model calculations (LSSM) of cadmium isotopes have been performed for $^{100-110}$Cd in this work using the code KSHELL [55], which makes use of the Lanczos iteration process described in Ref. [56]. The neutron model space ($N = 50$–82) consisted of the $2d_{5/2}$, $3s_{1/2}$,$2d_{3/2}$, $1g_{7/2}$, and $1h_{11/2}$ orbitals in which 2 neutrons for ^{100}Cd and up to 12 neutrons for ^{110}Cd distribute. Ten protons ($Z = 48$) remain in the $2p_{1/2}$ and $1g_{9/2}$ orbitals forming the proton model space ($Z = 38$–50). This way ^{88}Sr acts as an inert core of the model space, i.e., no interaction between the valence particles in the model space and the inert core is assumed. Figure 4.1 shows the model space for protons within the blue bracket and the neutron model space within the red bracket. Consequently downward arrows indicate the inner ^{88}Sr core with the same color code.

The used interaction *v3sbm* has been adjusted by N. Boelaert et al. [57]. The interaction is originating from the CD-Bonn potential [58] with slight adjustments in the monopole part of the Hamiltonian (mean field), this way the correct propagation of the single-particle neutron energies moving from $N = 51$ (^{89}Sr) towards the end of the shell at $N = 81$ (^{131}Sn) can be reproduced. Some changes in the effective *pp*, *np*, and *nn* matrix elements result from a fit of the force to 189 data points (excitation energies) in the mass region. The right choice of effective charges e_π, e_ν for protons and neutrons is crucial for the theoretical reproduction of $B(E2)$ values. Thus the proton effective charge e_π was fitted for a best match of the theoretical $B(E2)$ value of the $8_1^+ \rightarrow 6_1^+$ transition to the known experimental value in ^{98}Cd. With this fixed proton effective charge, the neutron effective charge e_ν was fitted to reproduce the

experimentally known B($E2$) values of the $2_1^+ \rightarrow 0_1^+$ transitions in ^{102,104}Cd within the shell model. The effective charges are thus $e_\pi = 1.7e$ and $e_\nu = 1.1e$, as in former shell-model calculations [57, 59, 22] performed with the same interaction.

4.2.1 Comparison of level schemes for ^{106}Cd

For a comparison of experiment and theory, level schemes have been build from experimental and shell-model data for ^{106}Cd. Figure 4.2a shows the experimental scheme up to a level energy of ∼2.5 MeV. Levels have been ordered with ascending spin from left to right. In cases of spin ranges in the results of Table 3.1, spin assignments have been taken from unpublished results stemming from a recent reanalysis of the $(n, n'\gamma)$-experiment [28]. This way, uncertainties in the level spins could be minimized. Therefore, certain level spins differ to findings of Table 3.1. $B(E2)$ values have been calculated from unpublished mean lifetimes (τ) [28] and multipolarity mixing ratios (δ) [28], using the code TRANSNUCULAR [60]. Branching ratios have been taken from this work (Table 3.1). The legend in Figure 4.2a shows the color code for different kinds of transitions, where i.e., multipolarity mixing ratios δ are known, unknown or have more than one value, due a second minimum in the least square fit procedure of the data analysis [28]. In the last mentioned case, the lower δ has been chosen, so that the higher $B(E2)$ value is displayed in Figure 4.2a. Red color indicates findings listed in Table 3.1, i.e. new γ-transitions and branching ratios differing from the literature [1].

Taking Figure 4.2a as a starting point, results of the shell-model calculation have been taken for a best reproduction of the level structure and transition probabilities of the experimental findings, considering solely $E2$ transitions . Levels colored in blue account for the two spin cases (2^+, 3^+) of the experimental level at 2254 keV. This results in the situation, that the experimental 2348 keV level might be represented by the shell-model 2_3^+ or the 2_4^+ state and the experimental 2371 keV level might be represented by the 2_4^+ or the 2_5^+ level within the shell model. Therefore the transition pattern of the 2371 keV level of the experiment is shown for the 2_4^+ and the 2_5^+ level in the shell model, whereas the transition of the experimental 2348 keV level is ether included in the transitions of the 2_4^+ state or by the blue colored 2_3^+ state.

Discussion of the shell-model results The amount of data displayed in Figure 4.2a and 4.2b opens a wide range for discussions on the ability of the shell model to reproduce the experimental situation. Nevertheless the comparison of both figures will be reduced to a more general view and only a few cases of interest are picked out for discussion.

A general challenge of the shell model is the proper reproduction of level energies. The used interaction *v3sbm* has been adapted to experimental data in this mass region as described above. From a comparison of both figures it is obvious, that the shell model calculates energies generally lower than in the experimental case. However, the reproduction is satisfying, especially in the lower energy region. Going higher in level energies, the energy deviation is increasing though. Focusing on the higher energy levels it is obvious, that the shell model is not able to reproduce

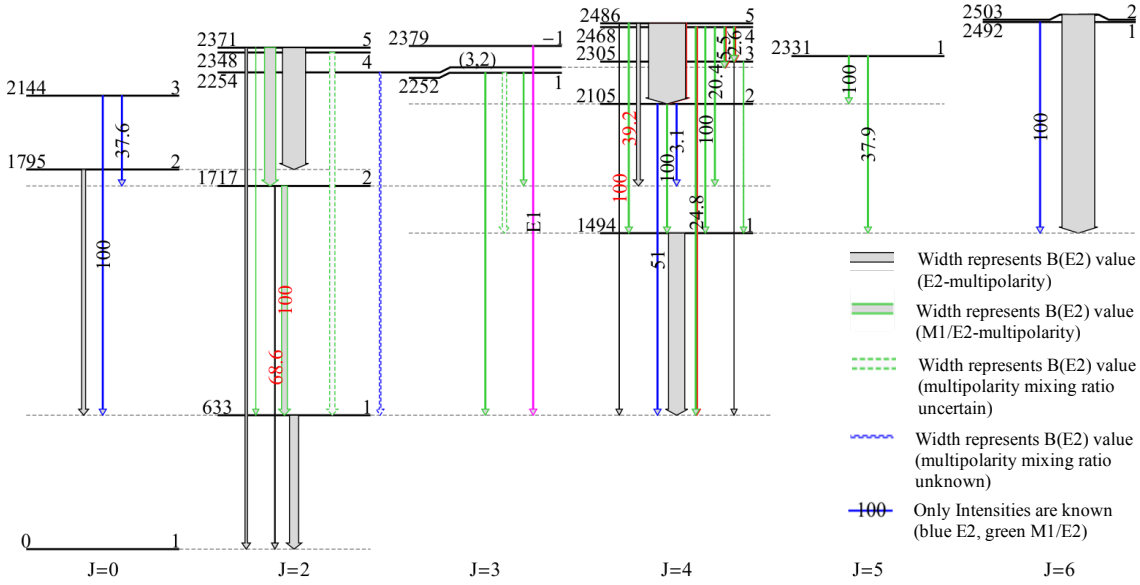

^{106}Cd (Experiment)

(a) Level scheme of the experimental situation below ~2.5 MeV. Branching ratios have been taken from this work. Mean level lifetimes, level spins and transition multipolarities are taken from [28]. New results of this work are marked with red color. Left level labels give the excitation energy in keV, right level labels give level indexes. (Note: The 2379 keV$\xrightarrow{1746\,\mathrm{keV}}$633 keVtransition is the only parity changing transition, denoted by the negative index -1. All other levels have positive parity.)

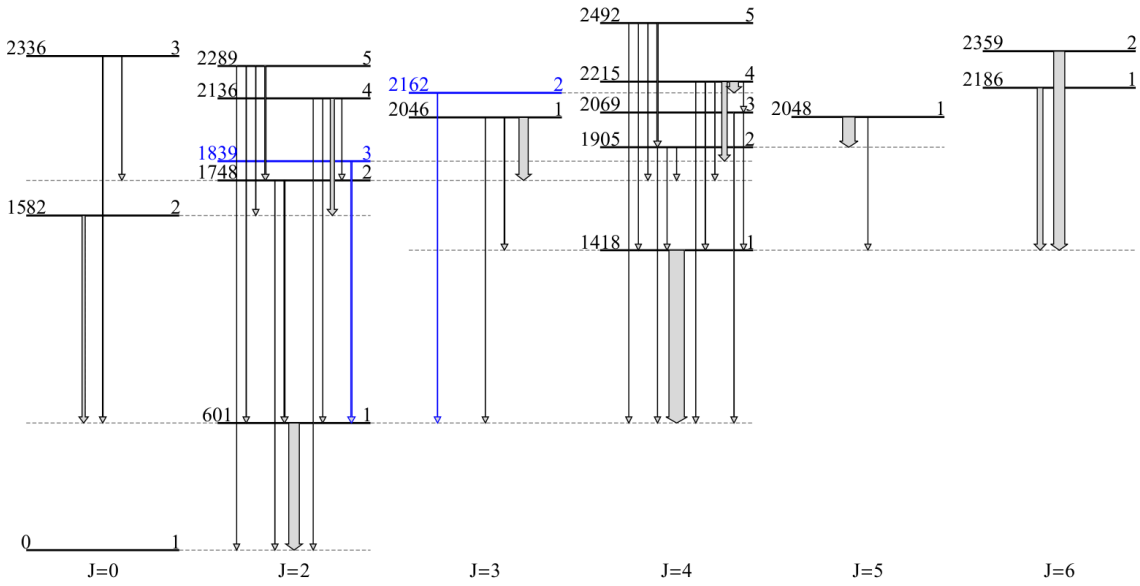

^{106}Cd (Shell–Model)

(b) Rebuild of the experimental level scheme from shell-model results. Blue colored levels account for the spin uncertainty of the experimental (2^+, 3^+) level at 2254 keV. Left level labels give the excitation energy in keV, right level labels give level indexes.

Figure 4.2: Comparison of the experimental and the shell-model level scheme

J_i^π	J_f^π	$B(E2)_{exp}$ [W.u.]	$B(E2)_{SM}$ [W.u.]	Comment
2_1^+	0_1^+	$25.7^{+0.3}_{-0.3}$	29.7	Yrast
4_1^+	2_1^+	$45.9^{+6.7}_{-5.2}$	43.3	Yrast
6_1^+	4_1^+	-	27.5	Yrast
2_2^+	2_1^+	$16.2^{+6.5}_{-12.2}$	2.8	
2_2^+	0_1^+	$1.6^{+0.3}_{-0.2}$	0.6	
4_5^+	4_2^+	104^{+90}_{-68}	3.6	
6_2^+	4_1^+	92^{+66}_{-56}	5.8	
0_2^+	2_1^+	$11.1^{+6.6}_{-5.6}$	8.9	
2^+_{4-5} (2371 keV)	0_2^+	66^{+39}_{-35}	$11.4(J_i^+ = 2_4^+)$	exp. Intruder
			$0.8\ (J_i^+ = 2_5^+)$	exp. Intruder
2^+_{4-5} (2371 keV)	2_2^+	31^{+21}_{-17}	$0.2\ (J_i^+ = 2_4^+)$	exp. Intruder
			$3.6\ (J_i^+ = 2_5^+)$	exp. Intruder

Table 4.1: Comparison of $B(E2)$ values from experiment and shell model

the small energy spacing between some states of equal spin. An expected effect in such cases is level repulsion due to level mixing. When unperturbed levels are close to each other or are even degenerated, the influence of the residual interaction between both states increases the energy gap and forces degenerate states to be non degenerate [25]. The shell model accounts for this effect with level spacings not below ∼90 keV in Figure 4.2b. However, the corresponding experimental cases do not show the same level repulsion. The $J = 2$ levels at 2348 keV and 2371 keV, the $J = 4$ levels at 2468 keV and 2486 keV, the $J = 6$ levels at 2492 keV and 2503 keV, all lie unusually close to each other (in case the 2254 keV level is a $J = 3$ state, the 2252 keV and the 2254 keV levels are to be considered too).

Comparing the transition rates between experiment and theory, a satisfying agreement for the Yrast-transitions can be found. Table 4.1 shows $B(E2)$ values of the shell model and experiment for a detailed comparison. However an experimental $B(E2)$ value for the $6_1^+ \to 4_1^+$ transition is not known.

The best agreement between the shell model and experimental values is expected in the low energy region. The 2_2^+-level is therefore a case of interest, as new experimental $B(E2)$-values for the $2_2^+ \to 2_1^+$ and $2_2^+ \to 0_1^+$ transitions, were derived from the branching ratio of this work and the mean lifetime stemming from the (n, n')-experiment [28]. As compared in Table 4.1, the experimental $B(E2)$-values are about an order of magnitude larger than the shell model, with however a very large experimental error bar for the $2_2^+ \to 2_1^+$ $B(E2)$. The branching ratio of the 2_2^+ has been calculated from the shell-model $E2$- and $M1$-matrix elements of the $2_2^+ \to 2_1^+$: $2_2^+ \to 0_1^+$ transitions. As described before the effective charges were $e_\pi = 1.7e$ and $e_\nu = 1.1e$, whereas the effective g-factors, determining the $B(M1)$-strength, were $g_{l,\pi/\nu} = 1.0/0.0$ and $g_{s,\pi/\nu} = 3.910/-2.678$, i.e. the effective $g_{s,eff} = 0.7 \cdot g_{s,free}$. To account for the inaccurate reproduction of transition energies of the shell model, these values have been taken from the experiment. The shell-model branching ratio for the $2_2^+ \to 2_1^+ : 2_2^+ \to 0_1^+$ transition is 100 : 38.5, whereas the experimental values are 100.0(41) : 68.6(31). These latter results indicate, that although the reproduction of the $B(E2)$-values is unsatisfying in case of the 2_2^+-level, the wave function

overlap of the shell model is in acceptable agreement to the experimental findings, as the branch of the $2_2^+ \rightarrow 0_1^+$ transition is less than a factor of 2 underestimated. The shell model supports the branching ratio of this work in the sense, that the $2_2^+ \rightarrow 2_1^+$ transition is the dominant branch in depopulating the 1717 keV level, contradictory to the literature [1], where the branching is given as 80(20) : 100(15) for the transitions $2_2^+ \rightarrow 2_1^+ : 2_2^+ \rightarrow 0_1^+$ (see also the discussion about the 1717 keV level in Section 3.5) .

It is obvious by a comparison of the results in Table 4.1 and Figure 4.2, that especially some strong, higher lying transitions can not be reproduced by the shell model. Although the $B(E3)$-values have large error bars, the newly discovered $4_5^+ \rightarrow 4_2^+$ transition in this work and the $6_2^+ \rightarrow 4_1^+$ transition are underestimated by 1-2 orders of magnitude. The transition rate of the experimental 2_{4-5}^+ state (2371 keV) to the 0_2^+state also lacks $B(E2)$ strength in the shell model by a factor of 6 in case it is the 2_4^+ state or two orders of magnitude in case it is the 2_5^+ state. Note, that it will be argued in the next section, that the 0_2^+ state is expected to be the head of an intruder band.

Therefore keeping the presence of proton intruder states in mind, it is not surprising, that the shell-model calculation is not able to reproduce certain transition strengths. The proton model space, with the $2p_{1/2}$ and $1g_{9/2}$ orbitals, does not allow particle-hole excitations ($p-h$ excitations) across the $Z = 50$ shell gap (see also Figure 4.1 for an overview of the model space). In the experimental case in contrast, a proton pair might be excited into the $Z = 50-82$ major shell. The number of valence protons thus increases from 2 holes to 4 holes ($4h$) and 2 particles ($2p$). These $4h-2p$ excitations are not present in the current shell-model calculations, which results in a lack of transition strength in the shell-model calculations for certain transitions.

It is however not the intention of this discussion to picture that all the mentioned cases of strong, higher lying transitions, the shell model fails to reproduce are related to intruder states or a configuration mixing with intruder states. It has been discussed, that the experimental situation of energetically close lying levels of equal spin is unexpected. The narrow level spacing, which is not reproduced by the shell model, reveals, that level mixing is not fully understood for some cases in ^{106}Cd. Therefore these issues are suggested as a matter for further investigation of upcoming works. The expansion of the proton model space beyond the $Z = 50$ shell gap in more detailed shell-model calculations could be a first staring point to crosscheck on the influence of intruder configurations to level mixing as well as transition rates.

5 Possible intruder band in ^{106}Cd

Nuclear excitations are not truncated by the presence of shell closures. As indicated in the former section, particles may be excited across a major shell gap. Due to the strong proton neutron attraction some of this energy invest is regained. This effect accounts especially when protons and neutrons occupy orbitals of similar angular momentum l after the excitation from one major shell to the other. The wave function overlap is maximized for these spin orbit partners. These excitations result in a m particle - n hole configuration added to the valence space resulting in an addition in collectivity. mp-nh configurations are thus collective excitations, that appear side by side with low energy excitations in which the nuclear core remaining mainly in a closed-shell system. Intruder states are considered as origin for shape coexistence, as these excitations exhibit a deformation characteristic different to the underlying excitations of the closed-shell system [19].

Intruder states are expected to be present in all but the lightest nuclei [19]. Consequently they have been discovered in many of the cadmium isotopes. An enhanced cross section in a two-proton transfer, (^{3}He,n)-reaction is a founded proof for an intruder state. Intruder 0^+ states have been identified via this reaction in the even Cd isotopes $^{106-112}$Cd [61]. However, the 0_2^+ state in ^{106}Cd did not exhibit enhanced excitation in this reaction. The lowest excited 0^+ state in ^{106}Cd observed in that work is at 3.00 MeV.

On the neutron deficient side of the cadmium chain intruder bands have been stated in ^{110}Cd [20] and ^{108}Cd [21]. It was found in these nuclei, that the intruder bands are based on the 0_2^+state. As already mentioned in Section 4.2.1, it is assumed in this work, that the 0_2^+ state in ^{106}Cd also forms an intruder band head.

In [30, 18] intruder bands have been identified by the "V"-shape pattern of their states when followed over the neutron number. Kumpulainen et al. [30] have tracked the lowest intruder 0^+state identified in ^{110}Cd and ^{112}Cd by the mentioned (^{3}He,n)-reaction over the whole chain of Cd-isotopes. In that work, ratios of $B(E2)$ values as well as the $B(E0)/B(E2)$ ratios of 0^+ states have been used as arguments for this tracking procedure. Figure 5.1 shows the outcome of this method. The Index of the proposed intruder band head changes in ^{114}Cd from 0_2^+ to 0_3^+. Therefore it was labeled with 0_A^+. It can be seen from Figure 5.1 (a) and (b), that the 0_A^+ and 2_3^+ state show a parabolic or "V"-shape pattern at the middle of the shell at ^{114}Cd. Figure 5.1 (c) shows a flat line for the $2_3^+/0_A^+$ ratio of level energies, indicating a similar characteristic for those states over the Cd-chain. (Note that the index of the 2_3^+-state for ^{106}Cd does no longer match with experimental situation after this work, see Figure 4.2a)

Besides these arguments, excitation energies of proposed intruder band members have been plotted relative to the lowest proposed intruder 0^+-state over the Cd-isotope chain in Fig 18 of Ref. [30] . This schematic was compared to ground state bands of Ru ($Z = 50 - 6$) and Ba ($Z = 50 + 6$). The distinct similarities between those schemes underlines the $2p - 4h$ character of the 0_A^+ state.

The left-hand side of Figure 5.2 also shows schematics of low energy levels build by Garrett et al. [18]. Proposed intruder states are marked with the index I. 0^+ states are denoted with the indexes A and B similar to the figures of Kumpulainen

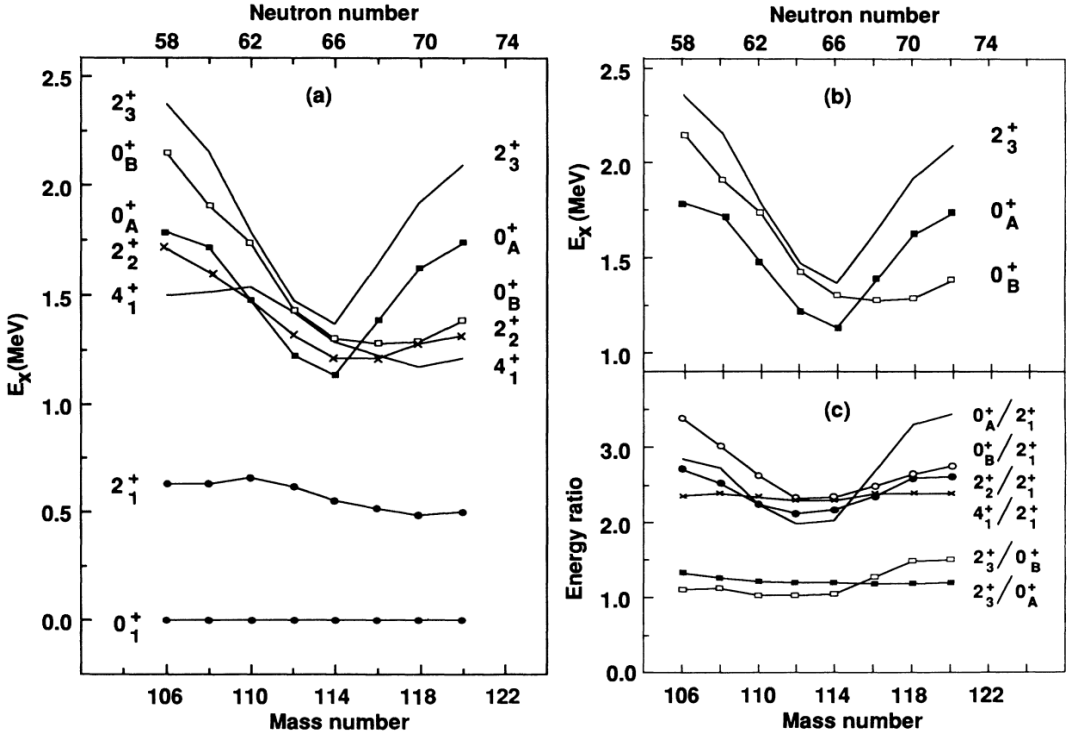

Figure 5.1: Adopted figure from Kumpulainen et al. [30].
(a): Systematic of low-lying, low-spin states in the even $^{106-120}$Cd. For clarity of presentation symbols marking the 2_3^+ and 4_1^+ level are omitted.
(b): Systematics of the 2_3^+, 0_A^+ and 0_B^+ states in the even $^{106-120}$Cd.
(c): Energy ratios of selected levels in even $^{106-120}$Cd.

et al. [30]. Note that contrary to the pattern of Kumpulainen et al. the states 0_A^+ and 0_B^+ were exchanged in ^{106}Cd for reasons not directly described in Ref. [18]. In that work, Garrett et al. studied the mixing of the intruder and normal state configuration by IBM-calculations and lay the focus to the middle of the shell, $^{110-116}$Cd. They state, that significant ambiguities arise in the classification of the 0_2^+ and 0_3^+ levels, since in most cases there is a nearly equal admixture of normal phonon and intruder character in the calculated levels. They state further, that the convention is adopted that the 0^+ state fed with the strongest $B(E2)$ value from the 2_i^+ intruder state is labeled as intruder bandhead [18]. It is additionally mentioned, that Garrett et al. [18] took data for ^{106}Cd from Ref. [27] to build the left-hand side of Figure 5.2. In [27] the 0_2^+ at 1795 keV is stated as a possible two phonon candidate. In this work, the pattern of Kumpulainen et al. is followed in the rebuild of the "V"-shape patterns on the right-hand side of Figure 5.2. As already argued the 0_2^+-state is expected to be the intruder band head in ^{106}Cd, which member states are denoted by red colored dots in Figure 5.2. As can be seen from Figures 4.2a and 5.3 the intruder band head is strongly connected via a transition of 66^{+39}_{-35} W.u., (see Table 4.1) to the 2_3^+-level at 2371 keV. This state is proposed to be the intruder band member. Therefore, contrary to the pattern proposed by Garrett et al. [18], the crossing of the states 2_I^+ and 2_A^+ in ^{106}Cd is also not adopted on the right hand side of Figure 5.2. Figure 5.3 focuses on the level scheme of the proposed intruder band and displays

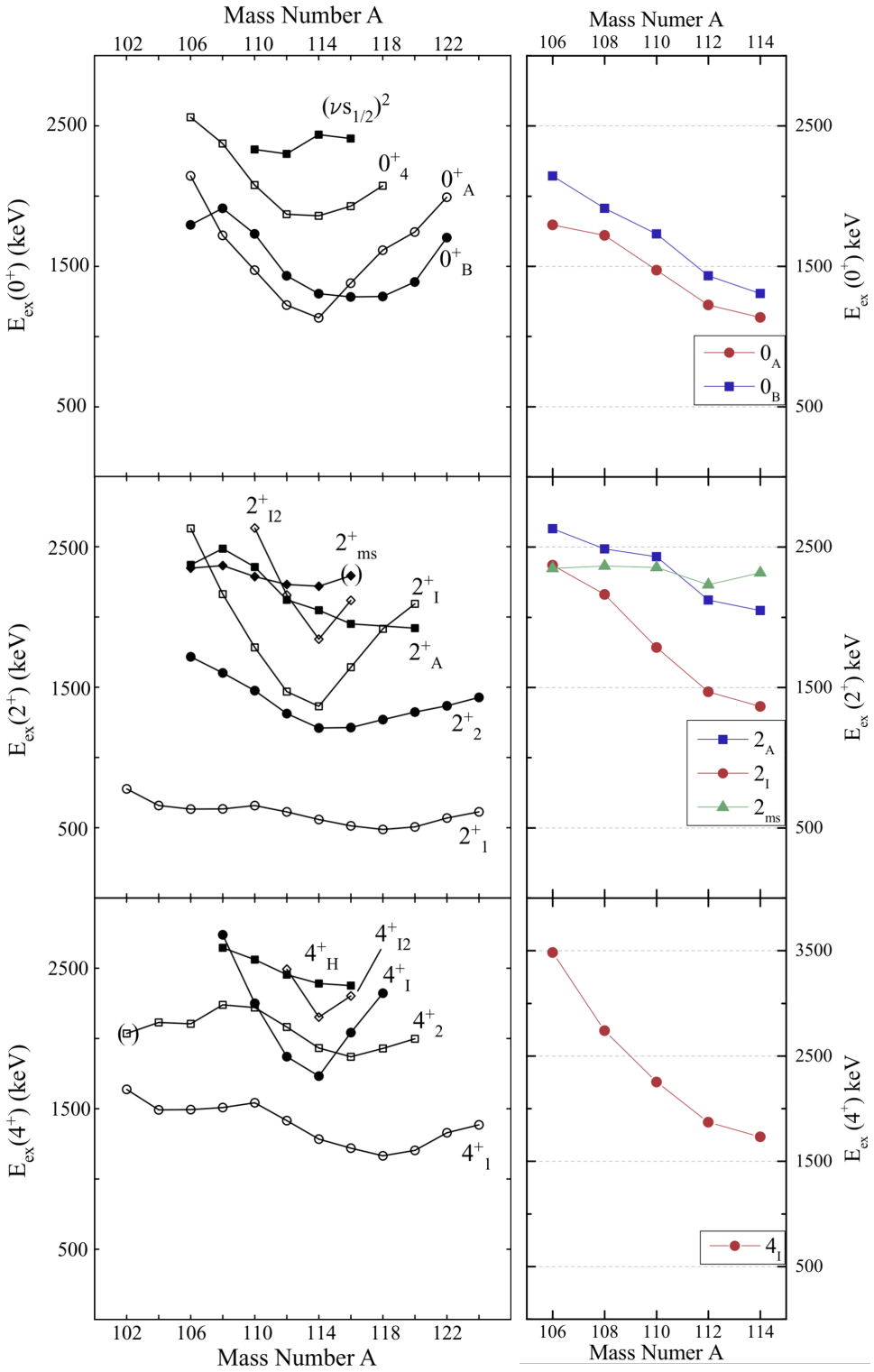

Figure 5.2: *Left-hand side:* Figures adopted from Garrett et al. [18]. Figures show systematic of low energy levels of the Cd-isotopes.
Right-hand side: Rebuild of the figures from Garrett et al. for the neutron deficient side of the shell only. Red colored circles indicate proposed intruder states. An alternative assignment of the 0^+_A, 0^+_B and 2^+_I, 2^+_A in ^{106}Cd [30] was applied. In addition, a 4^+_I state for ^{106}Cd has been proposed in this work (note the changed energy scale). See Text for details.

states that are connected. These are mainly some weaker transitions to the Yrast-band and one transition to the 2_2^+-level at 1717 keV. The latter one has the strongest connection away from the intruder band, with the $2_{I.}^+ \rightarrow 2_2^+$ transition exhibiting an $B(E2)$ value of 31^{+21}_{-17} W.u. and a $B(M1)$ value of 1.0^{+94}_{-8} W.u. (see also Table 4.1).

The newly discovered state at 3483 keV with a spin assignment of $2-4$ matches to the expected "V"-shape pattern of intruder states for a 4_I^+ member, as can be seen from the lower right part of Figure 5.2. This state is further on denoted as (4_I^+). Unfortunately experimental spin and mean lifetime of this state are not yet known. But from the branching ratios deduced in this work a $B(E2)$ transition strength could be estimated, assuming only $E2$-multipolarity relative for the $(4_I^+) \rightarrow 2_I^+$ and $(4_I^+) \rightarrow 2_1^+$ transitions. The strength of the transition to the 2_I^+ state at 2371 keV is a factor of $\sim$58 larger than the transition to the 4_1^+-Yrast-state at 1494 keV. The width of the dashed arrow going of the 3483 keV level in Figure 5.3 accounts for this fact under the assumption of a $\sim$1 W.u. $(4_I^+) \rightarrow 4_1^+$ transition, i.e. 58 W.u. for the the $(4_I^+) \rightarrow 2_{I.}^+$ transition. Accordingly, the presence of an additional $M1$ decay channel would enhance the relative $B(E2)$ value of the $(4_I^+) \rightarrow 2_I^+$ transition beyond the factor of 58.

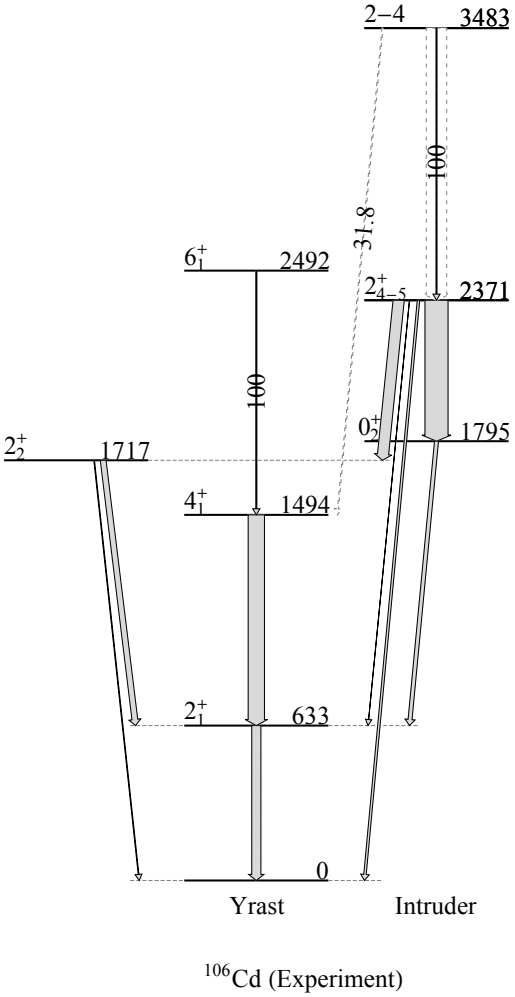

Figure 5.3: Partial level scheme of ^{106}Cd. The intruder band is shown together with connecting transitions to the Yrast-band and the 2_2^+. The arrow width indicates the $B(E2)$ transition strength. Branching ratios of transitions are given instead, whenever the $B(E2)$ values are unknown. The width of the 3482 keV$\rightarrow$2371 keV transition indicats the $B(E2)$ strength, derived using the branching ratios of this work under the assumption of a weak $\sim$1W.u. $E2$ transition to the 1494 keV level.

Except for the $2_I^+ \rightarrow 2_2^+$ transition of 31^{+21}_{-17} W.u., the other known transitions out of the band are orders of magnitudes weaker. With $\sim 0.06^{+0.05}_{-0.03}$ W.u. for the $2_I^+ \rightarrow 2_1^+$ and $6.8^{+4.1}_{-3.6}$ W.u. for the $2_I^+ \rightarrow 0_1^+$ transition. Table 5.1 gives $B(E2)$ values for intruder band transitions and transitions off the intruder band for ^{106,108,110}Cd with values adopted from [21]. The decay characteristics exhibit similarities throughout these, except for the relative enhanced $2_I \rightarrow 0_1^+$transition. The comparison shows furthermore, that the assumption of $B(E2)\sim$1 W.u. for the $(4_I^+) \rightarrow 4_1^+$ transition seems reasonable.

Decay	^{106}Cd B(E2) [W.u.]	^{108}Cd B(E2) [W.u.]	^{110}Cd B(E2) [W.u.]
$2_I \rightarrow 0_I^+$	66^{+39}_{-35}	$\geq 9^{+12}_{-5}$	23^{+27}_{-18}
$4_I \rightarrow 2_I^+$	58*	$\geq 6^{+4}_{-2}$	109^{+62}_{-53}
$2_I \rightarrow 2_1^+$	$0.06^{+0.05}_{-0.03}$	$\geq 0.4^{+0.3}_{-0.2}$	$0.16^{+0.12}_{-0.09}$
$2_I \rightarrow 0_1^+$	$6.8^{+4.1}_{-3.6}$	$\geq 0.06(3)$	0.30(10)
$4_I \rightarrow 4_1^+$	1*	$\geq 0.39(10)$	2^{+4}_{-1}
$4_I \rightarrow 2_1^+$	-	$\geq 0.14(4)$	$0.20^{+0.27}_{-0.10}$

Table 5.1: Comparison of $B(E2)$ values for intruder band transitions and transitions off the intruder band for $^{106-110}$Cd. Values for ^{108,110}Cd are adopted from [21]. * Relative $B(E2)$ values derived from the branching ratio of this work, while setting the strength of the $(2-4)_{intr.} \rightarrow 4_1^+$ transition arbitrarily to 1W.u..

From the presence of the proposed intruder band some issues arise with the classical vibrator picture of the Cd-isotope. It is obvious that a clear 0^+ two phonon candidate in ^{106}Cd does not exist. As the 0_2^+ is considered to be an intruder candidate, the 0_3^+ is the next possible candidate to be part of the phonon triplet. As can be seen from Figure 4.2a and Table 3.1 no collective $B(E2)$-transitions or strong branch are known from possible 2^+ three phonon quintuplet candidates. Neither does the "forbidden" $0_3^+ \rightarrow 2_2^+$ transition with a relative intensity of $I_\gamma = 37.6(16)\%$ support the vibrator picture, as the relative $B(E2)$-value of this transition, is expected to be a factor of ~ 210 larger, than the one of the $0_3^+ \rightarrow 2_1^+$ transition with an intensity of $I_\gamma = 100.0(41)\%$. The next 0^+ can be found at an energy of 2562 keV in the energy range of the 3 phonon quintuplet. Only one weak transition ($\sim$1 W.u. [28]) to the 2_1^+state is known for this state. However the 0_2^+-state could be a composition with an admixture of phonon and intruder character. But such statements are rather speculative at this point. Further discussions were made in e.g. [19, 18] to some extend, but are beyond the scope of this work.

6 A shell-model based deformation analysis of even Cd-isotopes

It is the aim of this work, to calculate the deformation parameters β and γ together with their variances $\sigma(\beta)$ and $\sigma(\gamma)$ from shell-model results for the first time ever conducted. The variances $\sigma(\beta)$ and $\sigma(\gamma)$ are of special interest, as they are observable that allow to distinguish between $O(6)$ and $U(5)$ symmetries, as stated in Ref. [62]. A short introduction to rotational invariants will be given in the beginning of this chapter, as well as a study on the convergence of these invariants as a function of number of shell-model data used as input. The parameters β, γ, $\sigma(\beta)$ and $\sigma(\gamma)$ will be presented and discussed by comparing the results to former studies of deformation in cadmium isotopes.

6.1 Deformation parameter

The very first models of the atomic nucleus were strongly connected to the idea of a nuclear shape. The well known *liquid drop model* of C. F. Weizesäcker was a first and successful approach to estimate nuclear binding energies. Intrinsically a conception about the nuclear shape arise from the picture of this model. A. Bohr and B. Mottelson firmed this concept by the development their *geometrical model* and classifying nuclei as vibrator or rotor type [4].

The nuclear radius of a quadrupole deformed nucleus can be written as [4]:

$$R = R_0 \left[1 + \sum_{\lambda\mu} \alpha_{\lambda\mu} Y^*_{\lambda\mu}(\theta, \phi) \right] \tag{6.1}$$
$$\text{with } \alpha_{\lambda\mu} = (-1)^\mu \alpha^*_{\lambda-\mu} = \frac{1}{R_0} \int R(\vartheta, \varphi)\, Y_{\lambda\mu}(\vartheta, \varphi)\, d\Omega.$$

$\lambda = 0$ is related to a compression of the nuclear matter without deformation, $\lambda = 1$ describes a one directional motion of the whole nucleus. A restriction to $\lambda = 2$ is therefore sufficient to describe nuclear quadrupole deformation. In a body fixed system with the symmetry axes coinciding with the coordinate system for the spherical harmonics, the amplitudes $\alpha_{2\mu}$can be written as:

$$\begin{aligned} \alpha_{21} = \alpha_{2-1} &= 0, \\ \alpha_{22} &= \alpha_{2-2}. \end{aligned} \tag{6.2}$$

The two non vanishing variables α_{20} and α_{22} ($=\alpha_{2-2}$) can be expressed as:

$$\begin{aligned} \alpha_{20} &= \beta \cos\gamma, \\ \alpha_{22} &= \frac{1}{\sqrt{2}} \beta \sin\gamma. \end{aligned} \tag{6.3}$$

The relation $\beta^2 = \sum_\mu |\alpha_\mu|^2$ follows directly from Equations 6.3. The elliptical shape of the nucleus can now be described by the variance of the nuclear radius R along the 3 body fixed symmetry axes, denoted by k:

$$\delta R_k = \sqrt{\frac{5}{4\pi}} R_0 \beta \cos\left(\gamma - k\frac{2\pi}{3}\right) \qquad k = 1,\, 2,\, 3. \tag{6.4}$$

The conservation of nuclear volume is fulfilled by $\sum_k \delta R_k = 0$.

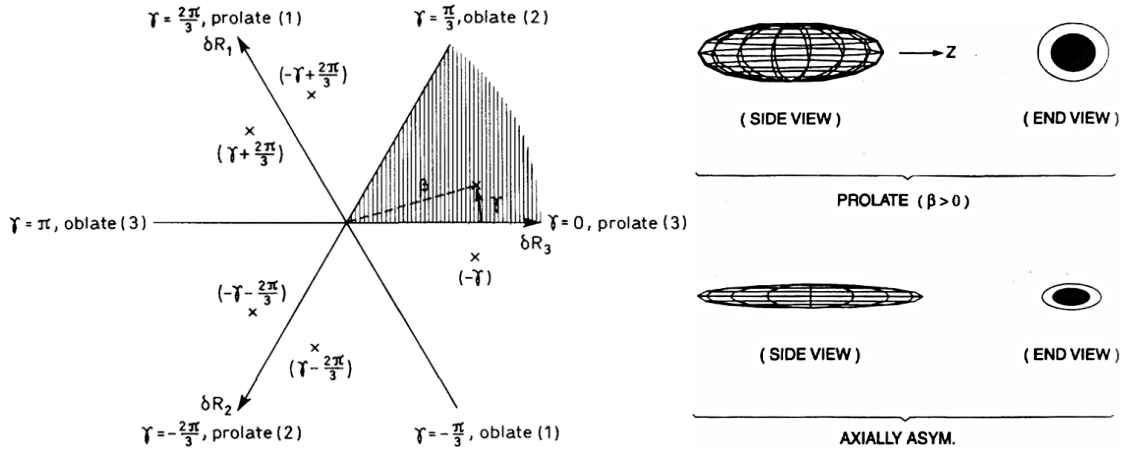

Figure 6.1: Left-hand side: Illustration of the deformation plane spanned by the parameters β and γ. Figure adopted from [4].
Right-hand side: Illustration of prolate (top) and axially asymmetric deformation of the nucleus. Figure adopted from [8].

Thereby, a quantification for the nuclear shape is given by the deformation parameters β and γ. The deformation strength is defined by the parameter β while γ specifies the nuclear shape or asymmetry. The left-hand side of Figure 6.1 shows the deformation plane that is spanned by β and γ. The right-hand side of Figure 6.1 gives an impression of resulting nuclear shapes.

6.2 Shape invariants

One outcome of the vibrator model of Bohr and Mottelson is a direct connection between nuclear deformation and transition strength. The quadrupole deformation with $\lambda = 2$ is therefore related to phonon excitations via [4]:

$$B\left(E\lambda; n_\lambda = 0 \rightarrow n_\lambda = 1\right) = \left(\frac{3}{4\pi} Z e R^\lambda\right)^2 \beta_\lambda^2. \tag{6.5}$$

Equation 6.5 is only valid for the first phonon excitation of the ground state. For completeness it is mentioned, that for higher energetic phonon states N the deformation can be calculated as [6]:

$$\beta_N^2 = \langle \alpha, N, JM | \sum_\mu \hat{\alpha}_{2\mu}^* \hat{\alpha}_{2\mu} | \alpha, N, JM \rangle = \frac{\hbar\omega_2}{2C_2}(5 + 2N). \tag{6.6}$$

The $\hat{\alpha}_{2\mu}$ are now treated as operators composed of phonon creation and annihilation operators. N denotes the phonon number, J spin and M the spin projection. C_2 is the stiffness parameter of the potential.

However this approach depends on the validity of the vibrator model. Which is not the case for all nuclei and as briefly mentioned in Sections 1 and 5, might not be valid to full extend to nuclei considered as vibrational, like the Cd-isotopes.

For a non-ideal vibrator, it can be assumed, that the transition strength does not strictly scale in integer steps of the phonon number n_2 or N of Equations 6.5 and 6.6 respectively. (See also top of Figure 1.2 for the dependence of the transition strength of the phonon number n for an ideal vibrator). On top of that, forbidden transitions of the vibrator model occur, that contain additional $B(E2)$ strength of the nuclear system, which have to be accounted for. K. Kumar [63] and D. Cline [64] developed a model independent way, to extract the nuclear deformation from $E2$ transition strength related to an exited state.

As outlined in detail in Ref. [63], the idea is to start from the $E2$ operator (compare Equation 2.7) befined by:

$$P_{2\mu} = \sum_{i=1}^{A} e_i r_i^2 Y_{2\mu}\left(\Omega_i\right), \tag{6.7}$$

and then couple $n = 2, 3, ...$ such operators to a tensor of rank 0:

$$P^{(n)} = \left[P_2 \otimes P_2 \otimes \cdots \otimes P_2\right]_2 \cdot P_2. \tag{6.8}$$

Because of the zero rank of this operator, a calculation of the expectation value of the operator in any eigenstate of the nucleus $|s, M_s\rangle$ results in a rotational invariant quantity:

$$P_s^{(n)} = \langle s, M_s | P^{(n)} | s, M_s \rangle = \frac{1}{\sqrt{2J_s+1}} \left\langle s \left\| P^{(n)} \right\| s \right\rangle. \tag{6.9}$$

In this notation s stands for J_s and parity π_s defining a nuclear state and M_s are the according magnetic projections. The invariants $P_s^{(n)}$ for $n = 2$, 3, 4, 6 can then explicitly be written as:

$$P_s^{(2)} = \frac{1}{2J_s+1} \sum_r \langle J_s \| P_2 \| J_r \rangle^2, \tag{6.10}$$

$$P_s^{(3)} = -\frac{\sqrt{5}}{2J_s+1} (-1)^{2J_s} \sum_{rt} \begin{Bmatrix} 2 & 2 & 2 \\ J_s & J_r & J_t \end{Bmatrix} \langle J_s \| P_2 \| J_r \rangle \langle J_r \| P_2 \| J_t \rangle \langle J_t \| P_2 \| J_s \rangle, \tag{6.11}$$

$$P_s^{(4)} = \left(\frac{1}{2J_s+1}\right)^2 \sum_{rtu} \langle J_s \| P_2 \| J_r \rangle \langle J_r \| P_2 \| J_t = J_s \rangle \langle J_t = J_s \| P_2 \| J_u \rangle \langle J_u \| P_2 \| J_s \rangle, \tag{6.12}$$

$$P_s^{(6)} = \frac{5}{(2J_s+1)^2} (-1)^{4J_s} \sum_{rtuvw} \begin{Bmatrix} 2 & 2 & 2 \\ J_s & J_r & J_t \end{Bmatrix} \begin{Bmatrix} 2 & 2 & 2 \\ J_u & J_v & J_w \end{Bmatrix} \langle J_s \| P_2 \| J_r \rangle \langle J_r \| P_2 \| J_t \rangle \cdot \langle J_t \| P_2 \| J_u = J_s \rangle \langle J_u = J_s \| P_2 \| J_v \rangle \langle J_v \| P_2 \| J_w \rangle \langle J_w \| P_2 \| J_s \rangle. \tag{6.13}$$

The indices r, t, u, v, and w describe intermediate states of the coupling and $\{\}$ denotes a Wigner-6j symbol. Jolos et al. [65, 66] have introduced approximation

formulas for quotients of these $P_s^{(n)}$ to allow a calculation of the shape invariants up to $P_s^{(6)}$ from only a few $B(E2)$ values. V. Werner et al. [62] have shown, that these quotients are related to β_{eff} and γ_{eff}, as well as their variances σ_β and σ_γ. It has to be mentioned, that the basic concept of relating quotients of $P_s^{(n)}$ to the variances σ_β and σ_γ can already be found in [63, 64], although not outlined in such detail as in [62]. A general expression for these quotients is given as [66]:

$$K_n = \frac{P_s^{(n)}}{(P_s^{(2)})^{n/2}}. \tag{6.14}$$

Therefore it can be written:

$$P_s^{(2)} = \left(\frac{3}{4\pi} ZeR^2\right)^2 \langle\beta^2\rangle = \left(\frac{3}{4\pi} ZeR^2\right)^2 \beta_{eff}^2, \tag{6.15}$$

$$K_3 = \frac{\langle\beta^3 \cos 3\gamma\rangle}{\langle\beta^2\rangle^{3/2}} = \cos 3\gamma_{eff}, \tag{6.16}$$

$$K_4 = \frac{\langle\beta^4\rangle}{\langle\beta^2\rangle^2}, \tag{6.17}$$

$$K_6 = \frac{\langle\beta^6 \cos^2 3\gamma\rangle}{\langle\beta^2\rangle^3}. \tag{6.18}$$

From these findings $\sigma(\beta)$ and $\sigma(\gamma)$ are expressed as:

$$\sigma(\beta) = \frac{\langle\beta^4\rangle - \langle\beta^2\rangle^2}{\langle\beta^2\rangle^2} = K_4 - 1, \tag{6.19}$$

$$\sigma(\cos 3\gamma) = \frac{\langle\beta^6 \cos^2 3\gamma\rangle - \langle\beta^3 \cos 3\gamma\rangle^2}{\langle\beta^2\rangle^3} = K_6 - K_3^2. \tag{6.20}$$

At this point the apparent similarity between Equations 6.5 and 6.15 is pointed out, although no model assumptions are made in deriving the rotational invariants, except for the assumption of a nuclear ellipsoid with a homogeneous charge distribution. It is also noted, that the notation here strongly follows the one of Kumar [63]. The differences to the notation of Cline [64] have been extensively laid open in a former work [22]. Although the notation of Cline is of a more shorthanded form, the notation of Kumar does not disguise the necessary ingredients i.e. Wigner-6j symbols and prefactors, to explicitly calculate the deformation parameters and their variances. Further note, that the prefactor $\left(\frac{3}{4\pi} ZeR^2\right)$ stems from the mentioned assumption of a homogeneous charge distribution over the whole nucleus.

6.3 Convergence study of invariants

From Equations 6.10-6.13 it can be read, that a summation of $B(E2)$ strength and combinations thereof are necessary for the calculation of the deformation parameters β and γ and their variances $\sigma(\beta)$ and $\sigma(\gamma)$. The question arises about the number

of matrix elements necessary to reach convergence or close to convergence for values of the calculated invariants.

For the higher mass isotopes of the cadmium chain the computational resources come to their limits, as the dimension of the possible configurations to form a spin state increases with the number of valence particles. This is especially the case for the calculation of 0^+ states. The computer code KSHELL [55] uses the M-scheme for the shell-model calculations. In the M-scheme the dimension of the configuration space is at maximum for the calculation of 0^+ states [67], as any possible J configuration within the valence space can be projected to $M = 0$. The computation time to calculate 0^+ states is therefore maxed out. The SM-calculations in this work could be extended over 50 2^+ states and 50 0^+ states for $^{100-108}$Cd, except for ^{100}Cd, where, in this model space, the full set of 37 possible SM 0^+ states was found. For ^{110}Cd 50 2^+states but only 10 0^+ states were calculated. The influence of this deficit in variety of 0^+ states in ^{110}Cd is also part of this convergence analysis. In contrast to the former work [22], the deformation analysis in this work will be restricted only to the ground state of the nuclei $^{100-110}$Cd, but this time include the deformation variances.

Convergence of deformation parameter β: Figure 6.2 (a) shows the sum of shell-model $B(E2)$ strength to 0^+ states defined by Equation 6.10 as a function of energy from the SM-calculations of ^{106}Cd as an example. Vertical, dashed drop lines indicate the energies of the 2^+_f states. Solid drop lines indicate a set of ten 2^+ states. In Appendix B, Figure B.1 a compilation of similar figures can be found for the nuclei $^{100-110}$Cd. It is is expected that the $0^+_1 \rightarrow 2^+_1$ transition, on average, covers $\sim$97% of the summed $E2$ transition strength $\sum_f B(E2; 0^+_1 \rightarrow 2^+_f)$ [8, 68]. Consequently a plateau is reached after the first 2^+ state in Figure 6.2 (a), when the $B(E2)$ strength of the 0^+_1 state is summed. The convergence of the mean square deformation β can therefore be considered as fulfilled by accounting for the first 50 $0^+ \rightarrow 2^+$ transitions. For the calculation of $\sigma(\beta)$ the convergence sums of higher 0^+_t states have also to be taken into account, as they form intermediate steps in Equation 6.12. Figure 6.2 (a) shows the convergence for different sums of higher 0^+ states up to an index of 50, 0^+_{50}. It can be seen, that a plateau is reached too in the $B(E2)$ sum of 0^+_{2-3} and possibly even 0^+_5. The sum $\sum_f B(E2; 0^+_{10} \rightarrow 2^+_f)$ exhibits the front edge of a plateau. For higher 0^+ states it is obvious, that the convergence is not fulfilled and some $B(E2)$ strength is missing. On the other hand, the $B(E2)$ sums of higher 0^+ do not exhibit such a steep increase as the $B(E2)$ sums of lower 0^+states and therefore the convergence of the $B(E2)$ sum of higher 0^+ is expected to contribute to a much lesser extend to the variances $\sigma(\beta)$ and $\sigma(\gamma)$. Similar results can be found for all the analyzed Cd-isotopes in Figure B.1. Although in ^{104}Cd the beginning of a convergence plateau for 0^+_{10} is not indicated, in this work it was assumed, that the number of 50 $0^+ \rightarrow 2^+$ transitions is sufficient to reach an overall convergence of the $B(E2)$ sums of the lower 0^+_i states, $i \lesssim 10$.

The influence of adding more $0^+ \rightarrow 2^+$ matrix elements to the sum of Equation 6.12 can be analyzed in Figure 6.2 (b) at the example of ^{106}Cd. The variety of intermediate $0^+$and 2^+ states increases along the x-axis. The black line marks the value of $\sigma(\beta)$ of the ground state with the full set of 50 intermediate 0^+ states

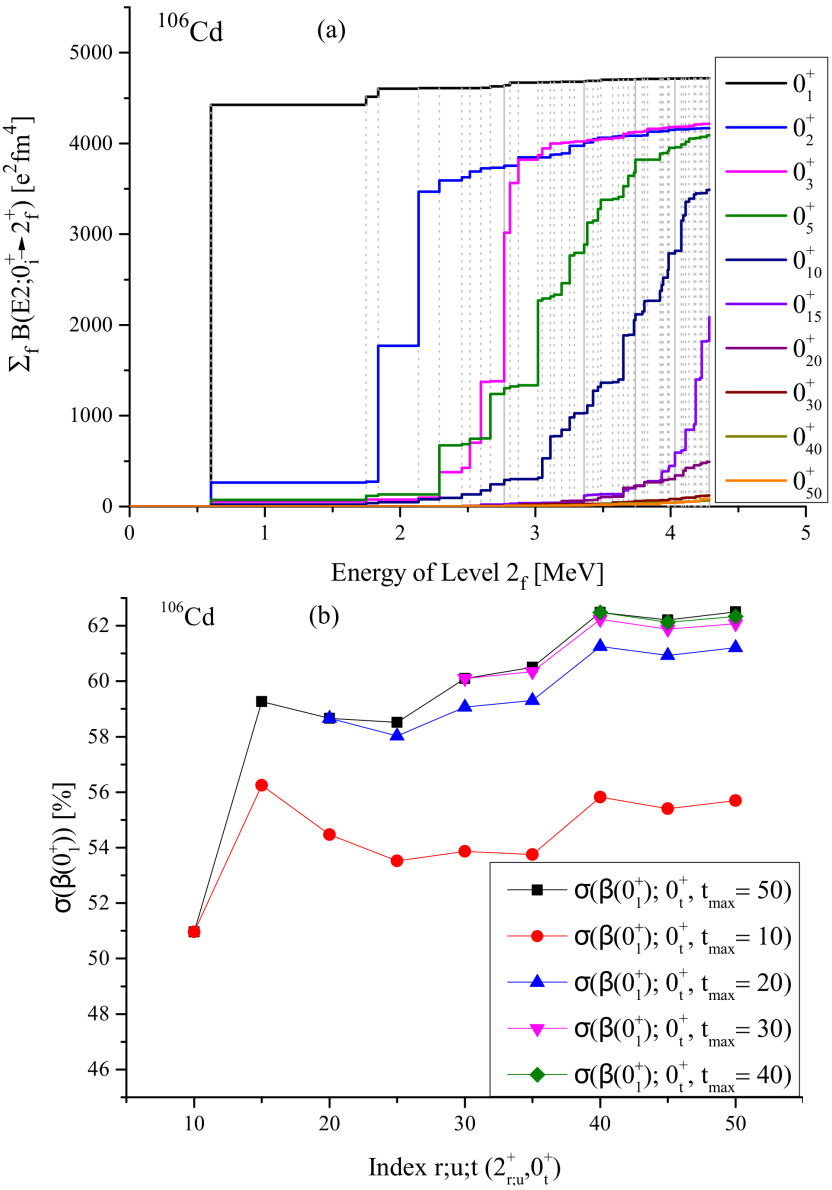

Figure 6.2: (a): A graphical illustration of the contributions of 2_f^+ states to the $B(E2)$ sums of the different 0_i^+ states as a function of energy of 2_f^+ states (with $f = 1, ...50$) on the horizontal axis. Shell-model results for ^{106}Cd are displayed. The sums give an impression of the convergence sums of matrix elements in Equations 6.10 and 6.12 necessary to calculate β and $\sigma(\beta)$. Vertical, dashed drop lines indicate the energies of the 2_f^+ states in each figure, with a solid drop line for every full set of ten 2^+ states.
(b): Mapping of $\sigma(\beta)$ in ^{106}Cd under the variance of contributing intermediate SM 2^+ and 0^+ states in Equation 6.12. The notation of spin indices is equal to Equation 6.12.

available. The number of $0^+$and 2^+ states contributing to $\sigma(\beta)$ therefore is equal in every point of this line. Due to different signs of the matrix elements involved no steady increase is observed by adding more states throughout the lines, (i.e. in

the sum of $\sigma(\beta)$). In Appendix B, Figure B.2 a compilation of similar figures for $^{100-110}$Cd can be found. Some figures, like for ^{102,104,106,110}Cd show a pattern of alternating increase and decrease of $\sigma(\beta)$ with increasing number of intermediate states. Whereas ^{100}Cd exhibits predominately a downward trend and ^{108}Cd predominately an upward trend. A clear convergence, like a plateau, can not be observed when the quantity of 50 intermediate 0^+ and 2^+ states is reached for all calculated isotopes, as could already be anticipated from Figure 6.2, showing $B(E2)$ sums of higher 0^+ states did not fully converge.

The color coded lines in Figure 6.2 (b) display values of $\sigma(\beta)$, when the variety of intermediate 0^+ states is limited and only the number of 2^+ states increases along the x-axis. Each colored line is starting from the black line which originates from the full set of 50 intermediate 0^+ states. At each starting point the number of intermediate 0^+ state is the same as the number of intermediate 2^+ states and consequently values of $\sigma(\beta)$ are equal to the ones shown in the black line. When studying the last step of intermediate 2^+states from 2^+_{45} to 2^+_{50} of all colored lines in Figures 6.2 (b) and B.2 (Appendix), a variation of $\sigma(\beta)$ of $1-2\%$ can be observed. It is assumed, that a contribution of matrix elements involving even higher index 2^+ states ($2^+_i; i > 50$) will not change the outcome of $\sigma(\beta)$ significantly. The value of $\sigma(\beta(0^+_1))$ for the isotopes $^{100-110}$ Cd is therefore considered to be sufficiently converged in the variety of 2^+ states. Another outcome of Figures 6.2 (b) and B.2 is a steady increase of $\sigma(\beta)$ with increasing maximum number of intermediate 0^+ states, denoted by the different color codes. It can be observed, that the distance of the lines reduces with increasing number of intermediate 0^+ states to the black line of 50 intermediate 0^+ states. The difference of $\sigma(\beta)$ calculated from 40 and 50 intermediate 0^+ states is below $\sim 1\%$. A convergence of $\sigma(\beta(0^+_1))$ in the variety of 0^+ states can be assumed, for $^{100-108}$Cd.

As a full set of 50 0^+ states was not calculated for ^{110}Cd it is interesting to get an estimate on the effect for $\sigma(\beta)$, if the full set was available using the Figures of the lighter isotopes. Figure 6.3 displays the difference for $\sigma(\beta)$ calculated by 50 2^+ and by only 10 0^+ states compared to $\sigma(\beta)$ calculated from 50 2^+ and 50 0^+ states in the nuclei $^{100-108}$Cd, plotted with increasing neutron number: $\sigma(\beta(0^+_1);\, 0^+_u,\, u_{max} = 10)/$ $\sigma(\beta(0^+_1);\, 0^+_u,\, u_{max} = 50) - 1$. A linear increase can be observed with increasing neutron number. From the linear fits the value of $\sigma(\beta)$ in ^{110}Cd is expected to be about 20 % underestimated, when calculated only by the available 10 intermediate 0^+ states. This gives a relative variance $\sigma(\beta)$ of 41.2(5)% in ^{110}Cd (compare Figure B.2).

Convergence of deformation parameter γ: For the extraction of the variance $\sigma(\gamma)$ from the shell-model $E2$ strengtrh, Equation 6.13 has to be used. With 50 0^+ and 50 2^+ states the number of intermediate steps in the sum of Equation 6.13 is significantly higher than for the calculation of $\sigma(\beta)$, referring to the ground state. The number of combinations of matrix elements can be calculated as: $50 \cdot \langle 0^+_1 \,|E2|\, 2^+\rangle \cdot 50^2 \cdot \langle 2^+ \,|E2|\, 2^+\rangle \cdot 50^2 \cdot \langle 2^+ \,|E2|\, 0^+\rangle \cdot 50^2 \cdot \langle 0^+ \,|E2|\, 2^+\rangle \cdot 50^2 \cdot \langle 2^+ \,|E2|\, 2^+\rangle \cdot 50 \cdot \langle 2^+ \,|E2|\, 0^+_1\rangle$ $\approx 9.8 \cdot 10^{16}$ combinations, i. e. summands. The computing time for the calculation of 1 value of $\sigma(\gamma)$ took $\sim$3 days. This calculation includes the maximum number of available matrix elements. Although the calculation time decreases when the

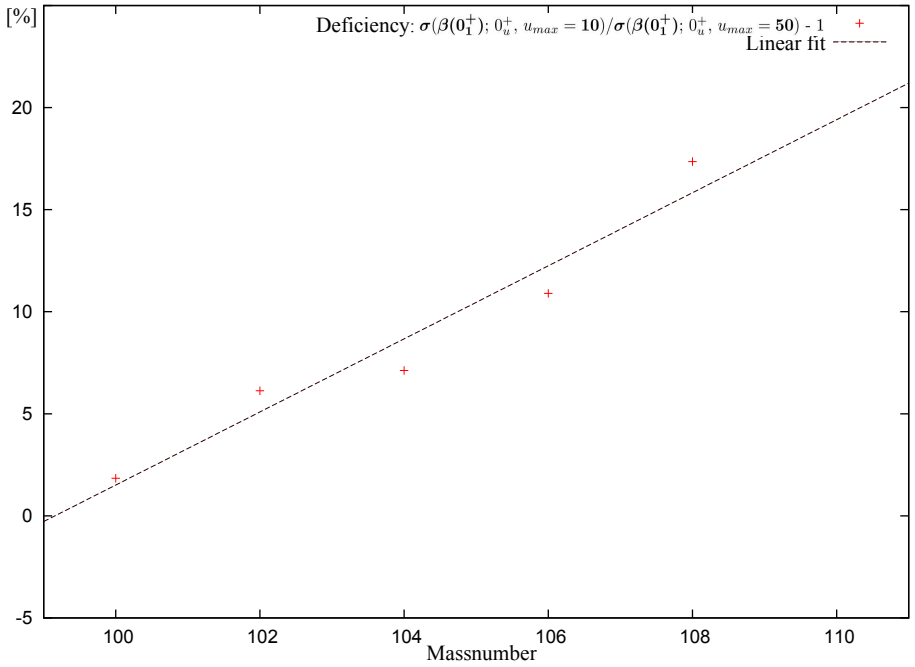

Figure 6.3: Linear fit of the deficiency in $\sigma(\beta)$ over the mass number A. Values were calculated from 10 intermediate 0^+ states and 50 intermediate 2^+states compared to $\sigma(\beta)$ with 50 intermediate 0^+ and 2^+ states.

number of involved 0^+ states is reduced, like done in the former study about the development of $\sigma(\beta)$, the number of matrix element combinations with only 10 intermediate 0^+ states is still $\approx 3.9 \cdot 10^{15}$ and takes $\sim$1.5 days. Therefore a similar study as shown in Figure 6.2 (b) and B.2 was not conducted for $\sigma(\gamma)$.

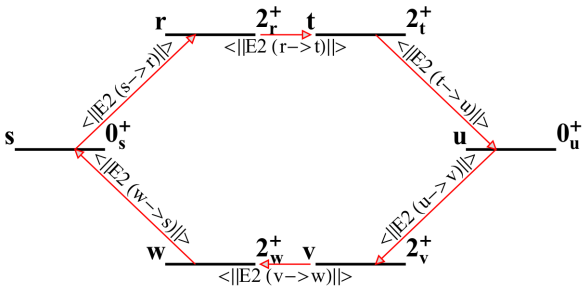

Figure 6.4: Illustration for the combination of matrix elements necessary for the calculation of $P_s^{(6)}$ of Equation 6.13. Leaving out the two $2^+ \rightarrow 2^+$ transitions of one combination ($\Rightarrow 2_r^+ = 2_t^+; 2_v^+ = 2_w^+$), results in the matrix element combinations of $P_s^{(4)}$ of Equation 6.12.

Some comments about the quality of the convergence of $\sigma(\gamma)$ are necessary at this point, especially when the full set of 50 0^+ states is not available, like for ^{110}Cd. By comparing Equations 6.12 and 6.13 it can be seen, that the combination of matrix elements necessary to calculate the invariant $P_s^{(4)}$ are included in the combinations of $P_s^{(6)}$. Figure 6.4 gives an overview of the combinations needed to calculate $P_s^{(6)}$. The Figure reveals, that leaving out the intermediate $2^+ \rightarrow 2^+$ transitions in $P_s^{(6)}$, the matrix element combinations of $P_s^{(4)}$ remain (excluding the Wigner-6J symbols in this perspective). The full set of 50 2^+ states can be considered as an intermediate set of transitions in $P^{(4)}$, that do not influence the convergence, if 0^+ states are missing. Figure 6.5 displays convergence sums of $2^+ \rightarrow 2^+$ $E2$ transition strength similar to the ones shown in

Figure 6.2 (a) for the 0^+ states. A compilation of similar figures for the isotopes $^{100-110}$Cd is given in Figure B.3 in Appendix B. Thus it can be assumed, that the convergence of the set of 50 $2^+ \rightarrow 2^+$ transitions is of the same quality as for the $0^+ \rightarrow 2^+$ transitions. Although the sums of higher 2^+ states in Figures 6.5 and B.3 do contribute a higher amount of $B(E2)$ strength than the ones with the same index of 0^+ states in Figures 6.2 (a) and B.1, the convergence plateau is reached even for sums of $2^+ \rightarrow 2^+$ transitions with higher index (Figures 6.5 and B.3). E.g. the front edge of the plateau can often be observed in the 2^+_{40} sums in Figure B.3.

It can be concluded, that the values of $\sigma(\gamma)$ are of the same quality as the once derived for $\sigma(\beta)$. Since a study of the effect of missing 0^+ states is not examined for $\sigma(\gamma)$, no statement about the influence of missing, intermediate 0^+ states can be made. As the sign of matrix elements of $0^+ \rightarrow 2^+$ transitions changes an increase of $\sigma(\gamma)$ with increasing number of 0^+ states can not be assumed. And linear development, like found for $\sigma(\beta)$ in Figure 6.3, is not guaranteed for $\sigma(\gamma)$. Anyhow, a 20% uncertainty for the derived value of $\sigma(\gamma)$ will be assumed for ^{110}Cd in analogy to the case of $\sigma(\beta)$.

Occupation of the $h_{11/2}$ orbital: One interesting effect that can be observed in Figures 6.5 (b) and B.1 is the excess of the summed $B(E2)$ strength for the 0^+_2 and 0^+_3 states compared to the ground state in ^{108,110}Cd. This change in the character of excited 0^+ states can not be observed in the lighter nuclei $^{100-106}$Cd. An explanation can be found in the $h_{11/2}$ orbital occupation numbers. Table 6.1 gives a short overview of the mean shell-model occupation for the $h_{11/2}$ orbital of the corresponding shell-model state. According to that outcome, the 0^+_2 and 0^+_3 states exhibit an $h_{11/2}$ orbital filling of approximately one neutron and even above for the 0^+_2 in ^{110}Cd. However, the 0^+ states are of positive parity, whereas the $h_{11/2}$ orbital is of negative parity. It can therefore be assumed, that the mean $h_{11/2}$ occupation numbers of Table 6.1 represent an admixture of configurations of even $h_{11/2}$ occupations $(0n, 2n)$, that build the 0^+ states. As also the ground state of ^{110}Cd is build up by a similar $h_{11/2}$ occupation as the other mentioned excited 0^+ states in ^{108,110}Cd, the argument of a $h_{11/2}$ orbital filling is not a stand alone explanation for the excess of the $B(E2)$ sums. The occupation of the 2^+ states of the $2^+ \rightarrow 0^+$ transitions have also to be taken into account. Therefore, to not extend the discussion too much, only two examples are given at this point: The $h_{11/2}$ orbital of the 2^+_3 state in ^{108}Cd is filled with 1.34 neutrons whereas the 2^+_1state is filled with 0.34. The $2^+_3 \rightarrow 0^+_2$ transition in ^{108}Cd is the major contributor to the $B(E2)$ sum of the 0^+_2state according to Figure B.1. For ^{110}Cd the $h_{11/2}$ occupation number of 1.65 of the 2^+_2 state is compared to 1.01 for the 2^+_1. In ^{110}Cd the 2^+_2 is the first major contribution to the $B(E2)$ sum of the 0^+_2. Both examples and the findings of Table 6.1 underline the contribution of the

	0^+_1	0^+_2	0^+_3
^{100}Cd	0.03	0.03	0.02
^{102}Cd	0.05	0.05	0.07
^{104}Cd	0.08	0.05	0.12
^{106}Cd	0.16	0.10	0.09
^{108}Cd	0.34	0.90	0.82
^{110}Cd	0.88	1.50	0.83

Table 6.1: Shell-model occupation numbers of the $h_{11/2}$ orbital of the 0^+_{1-3} states tracked over neutron number.

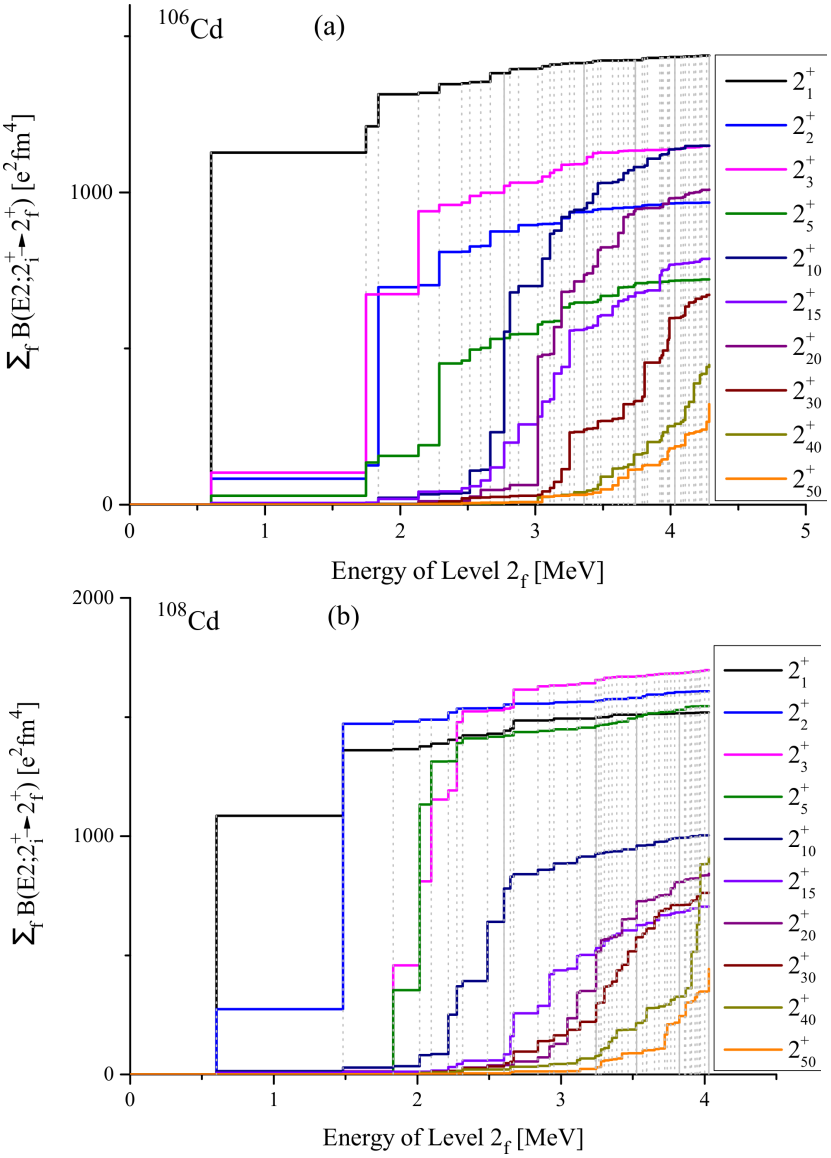

Figure 6.5: A graphical illustration of the contributions of 2_f^+ states to the $B(E2)$ sums of other 2_i^+ states as a function of energy of the various 2_f^+ states (with $f = 1, ...50$) on the horizontal axis. The sums give an impression of the convergence of matrix elements in Equations 6.11 and 6.13 necessary to calculate γ and $\sigma(\gamma)$. Shell-model results of ^{106}Cd (a) and ^{108}Cd (b) are illustrated. Vertical, dashed drop lines indicate the energies of the 2_f^+ states in each figure, with a solid drop line for every full set of ten 2^+ states.

$h_{11/2}$ orbital to $B(E2)$ transition strength starting at ^{108}Cd onwards to the heavier isotopes.

6.4 Deformation analysis

The deformation parameters β derived from Equation 6.15 are presented in Figure 6.6. Results of a former work [22] could thereby be extended up to ^{110}Cd. The

blue line in Figure 6.6 displays the outcome of the shell model with the value for ^{98}Cd taken from the former study. The black color denotes experimental results, whereas only the $2_1^+ \rightarrow 0_1^+$ $E2$ transition strength were considered to derive β. The closeness of both curves is a consequence of Equation 6.5 and underlines the phonon picture of the $2_1^+ \rightarrow 0_1^+$ transition, that accumulates all $B(E2)$ strength within the vibrator model. This accumulation of $B(E2)$ strength can also be seen from the instantaneously beginning of the plateau after the $2_1^+ \rightarrow 0_1^+$ transition in Figures 6.2 (a) and B.1. The newly derived value for ^{110}Cd continues the trend of a beginning saturation in deformation towards midshell. Starting in ^{98}Cd with a small deformation of $\sim$0.07 in β, the deformation increases, although with decreasing steepness in neutron number, ending in ^{110}Cd with $\beta\sim$0.19. The slight over estimate of $B(E2)$ strength in the shell model from ^{106}Cd on can be tracked down to the effective charges, $e_\pi = 1.7e$ and $e_\pi = 1.1e$. A reduction of the values would result in a better overall reproduction of the $2_1 \rightarrow 0_1$ transitions over the Cd-chain, but the shell-model $B(E2; 4_1 \rightarrow 2_1)$ would match to a lesser extend to the experimental findings, as already discussed in [22]. The observed increasing deformation towards the middle of the shell supports findings of Ref. [7], where it is stated, that large quadrupole moments observed in ^{114}Cd suggest a deformed nucleus in the middle of the shell.

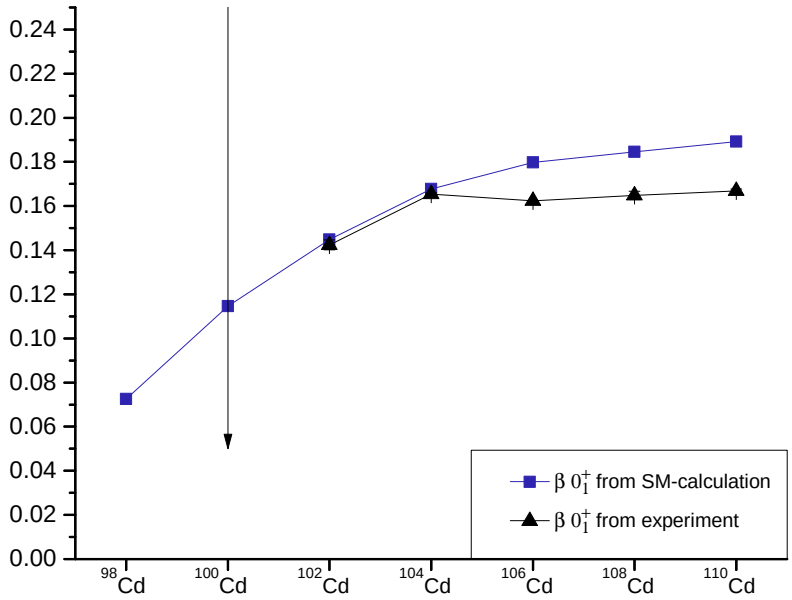

Figure 6.6: The calculated quadrupole deformation for the 0_1^+ ground states (blue squares) compared to experimental data [69] (^{100}Cd), [59] ^{102,104}Cd, [70] ^{106,108,110}Cd. The shell-model effective charges were $e_\pi = 1.7e$ and $e_\nu = 1.1e$. For the experimental ground states only the $2_1^+ \rightarrow 0_1^+$ $E2$ transition strength was considered to extract the value of β. The SM-result for ^{98}Cd has been taken from a former work [22].

	β	$\sigma(\beta)$	γ	$\sigma(\gamma)_+$	$\sigma(\gamma)_-$
^{98}Cd	0.072*	-	7.8°*	-	-
^{100}Cd	0.115	0.157 (137%)	12.3°	12.0° (97%)	27.6° (224%)
^{102}Cd	0.145	0.136 (95%)	13.0°	8.9° (68%)	23.3° (179%)
^{104}Cd	0.168	0.119 (71%)	13.7°	8.3° (61%)	22.5° (164%)
^{106}Cd	0.180	0.105 (58%)	15.2°	6.5° (43%)	11.1° (73%)
^{108}Cd	0.185	0.092 (50%)	17.4°	5.1° (30%)	6.7° (38%)
^{110}Cd	0.189	0.065 (34%)	20.0°	5.0° (25%)	5.9° (30%)
correction $\sigma_{\sim 20\%}$:		0.078 (41%)		5.9° (30%)	7.3° (37%)

Table 6.2: Deformation parameters β, $\sigma(\beta)$, γ and $\sigma_{\pm}(\gamma)$. The last line gives by $\sim 20\%$ corrected variances. Corrections for $\sigma(\gamma)$ should rather be considered a substitute.
* Values taken from [22].

Extending the shell-model results of Figure 6.6 by the variance parameter $\sigma(\beta)$ results gives the outcome shown in Figure 6.7 (a) . The gray variance bar at ^{110}Cd accounts for the estimated deviation of $\sim 20\%$ in the variance stemming from the input of only 10 available 0^+ states, instead of 50 0^+ states like for $^{100-108}$Cd, as discussed in Section 6.3. Figure 6.7 (b) shows the development of γ and $\sigma(\gamma)$ with increasing neutron number. Here the gray bar also indicates an increase of $\sim 20\%$ for $\sigma(\gamma)$. Note however, that this correction is to be considered as a substitute, since no quantitative convergence analysis has been conducted for $\sigma(\gamma)$. The corresponding numerical values of the deformation parameters shown in Figures 6.7 (a) and (b) can be found in Table 6.2. As can be read from Equations 6.16, 6.18 and 6.20, the extraction of γ to values in [°] and its variance involves the arccos-function, which is non symmetric around any value of γ between 0° and 60°. This results in asymmetric upper and lower variances of γ in [°] derived from one value of $\sigma(\cos 3\gamma)$ of Equation 6.20. Upper and lower values of $\sigma(\gamma)$ in [°] given in Table 6.2 are therefore denoted by $\sigma(\gamma)_{\pm}$.

It can be seen from the results of Figure 6.7 (a), that while in ^{100,102}Cd β very soft, e.g. dynamic, it is becoming increasingly rigid towards the middle of the shell, as can also be seen from the relative values of $\sigma(\beta)$ of Table 6.2. The approximated (corrected) value for ^{110}Cd nicely fits in this trend. Figure 6.7 (b) shows together with Figure 6.7 (a), that the nuclear shape is developing from a slightly prolate deformation of $\gamma = 7.8°$ in ^{98}Cd towards an increasingly triaxial deformed one with $\gamma = 20.0°$ in ^{110}Cd. The newly derived value of γ for ^{110}Cd, not available in [22], gives the impression, that γ is increasingly developing towards 30° at the middle of the shell, a value, that separates the prolate from the oblate region in the deformation plane (i.e. triaxial shape). The variance $\sigma(\gamma)$ is constantly decreasing with neutron number in Table 6.2. The substitute for the corrected $\sigma(\gamma)$ value of ^{110}Cd does not adequately fit into this trend, as it seems to reproduce the situation in ^{108}Cd. Values of $\sigma(\gamma)$ for ^{110}Cd derived with the same convergence as available for lighter isotopes are therefore assumed to lie closer to the uncorrected results than to the substitute. Consequently an increase in rigidity can also be observed for γ towards the middle of the shell.

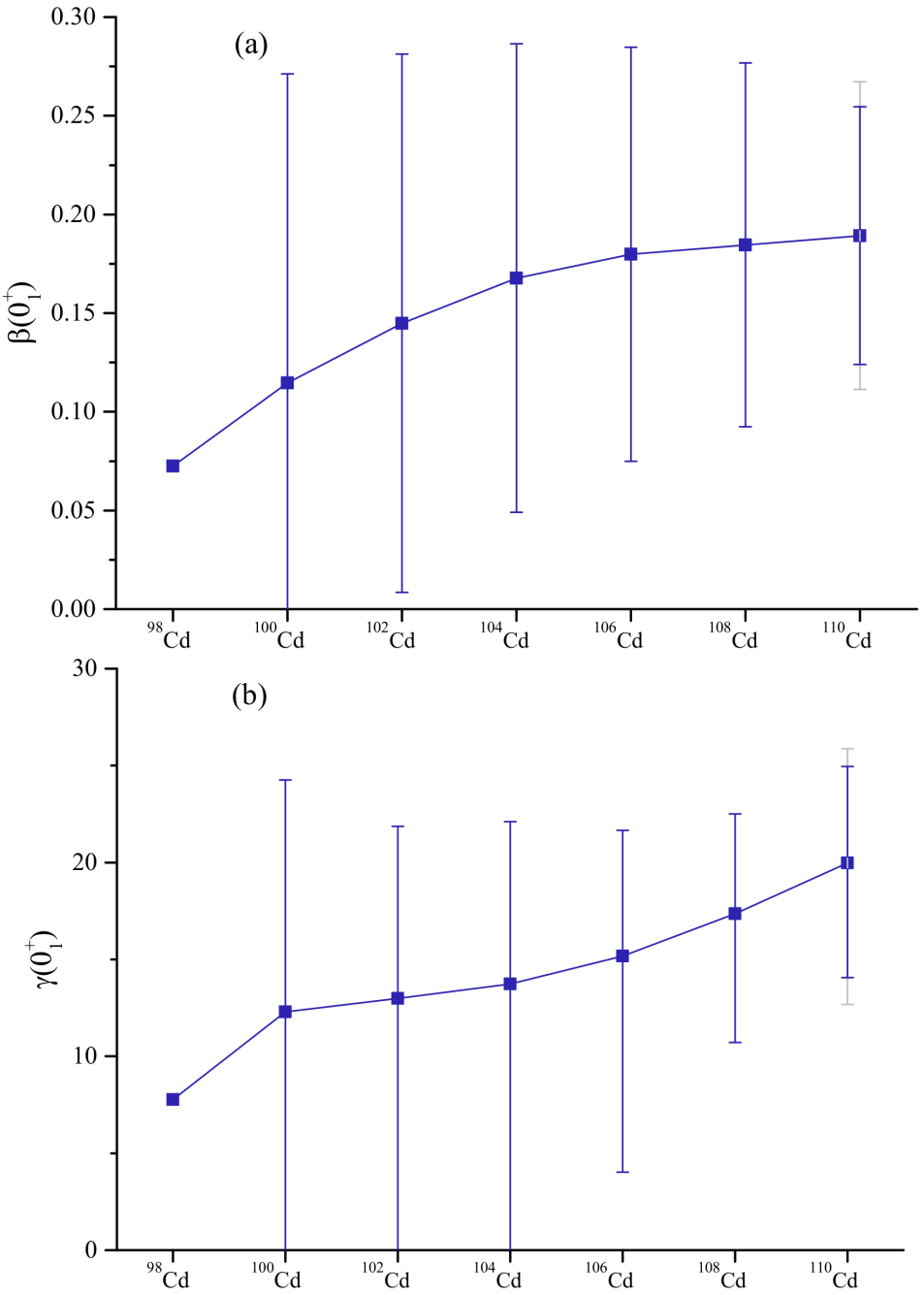

Figure 6.7: (a): The development of deformation the parameter β and its variance $\sigma(\beta)$ with increasing neutron number. The gray variance bar at ^{110}Cd accounts for the estimated deficiency of $\sim 20\%$ in the variance stemming from only 10 available 0^+, states instead of 50 0^+ states like in $^{100-110}$Cd (see discussion in Section 6.3).
(b): The development of deformation the parameter γ and its variance $\sigma(\gamma)$ with increasing neutron number. The same $\sim 20\%$ deficiency correction for the variance is shown as a substitute for ^{110}Cd, represented by the gray bar.
The SM-results for ^{98}Cd has are taken from [22].

In the work of Gade et al. [21] from 2002 the first observation of an intruder band in ^{108}Cd is handled. It is stated, that the chain of isotopes ^{108,110,112}Cd forms a transitional path between the vibrational $U(5)$ and the gamma-unstable $O(6)$ dynamical symmetry of the interacting boson model (interacting boson model). This symmetry transition is stated to happen with decreasing neutron number. i. e. $U(5)$ at the middle of the shell. It is argued, that a two phonon 0^+ state is not allowed in the $O(6)$ symmetry and the non intruder 0^+ states are increasing with distance to mid-shell. As can bee seen from Figures 5.1 and 5.2 0^+ states begin to leave the two phonon range and start to settle at three phonon energies when moving from the middle to the beginning of the shell. However, these arguments for a symmetry transition are based solely on the energies of the first excited 0^+ states.

In a work of 2012 Garrett et al. [20] studied the mixing of intruder states and the underlying (phonon) structure of ^{110}Cd and concluded, that the rejection of a strong mixing scenario for ^{116}Cd reveals, that the non intruder states are not vibrational, but the decay pattern is strongly suggestive of a γ-soft, or $O(6)$-type, nucleus. A statement confirmed by two former works of Garret et. al. from 2008 [18] and 2010 [7].

The increase in rigidity in β and γ shown in Figure 6.7 support these findings, as it reveals the development from a nearly spherical vibrator towards a deformed, axially asymmetric, γ-soft structure. Werner et al. [62] have mapped the invariants of Equations 6.15 - 6.18 and 6.20 derived from IBM calculations for 10 bosons towards the ECQF (extended consistent Q formalism) square. Figures of the mapping procedure of the invariant values can be found in Appendix C Figure C.1. Together with values of K_3, K_4, K_6 and $\sigma(\cos 3\gamma)$ derived in this work, given in Table C.1, the corresponding position on the ECQF square can be tracked. The heaviest studied nucleus of this work, ^{110}Cd, has 1 proton boson and 6 neutron bosons. The lighter nuclei posses less neutron valence bosons. The invariant maps of Figure C.1 are therefore not strictly applicable to the invariants derived in this work, but give a qualitative guideline about the nuclear structure development. Starting close to the edge representing the $U(5)$ limit with $K_3 = 0.80$, $K_4 = 1.16$, $K_6 = 1.14$ for ^{100}Cd in Figure C.1, the decreasing values especially of K_3 and K_6 with increasing neutron number point towards the $O(6)$ symmetry. Although no definite position can be pinpointed on the ECQF square from Figure C.1, the values of $K_3 = 0.50$ and $K_6 = 0.49$ of ^{110}Cd are indicating, that the $O(6)$ limit with $K_3 = 0$ is not reached, but this nucleus is rather placed in the region of $\zeta \sim 0.6 - 0.8$ and $\chi \sim -(0.1 - 0.3)$.

It is now interesting to compare the derived deformation results from the shell model with results of different approaches. A recent work of Nomura and Jolie of 2018 studied the structure of the even $^{108-116}$Cd isotopes [71]. As a starting point self-consistent mean-field (SCMF) calculations have been carried out. The resulting potential energy surfaces have later on been used to match the energy surfaces of the IBM-2 Hamiltonian to them. The reader is referred to [71] for further details. On the left hand side of Figure 6.8 the $\beta\gamma$ deformation energy surfaces of the SCMF calculations of that work are shown for ^{108,110}Cd. The right hand side shows the corresponding ground state deformation parameters of the shell model derived in this work (Similar figures for all analyzed nuclei can be found in Figure C.2 Appendix C). It can be observed, that the SCMF energy surface shows a minimum for both

nuclei at ~ 0.18 in β. A result in common with the shell-model findings. However the energy surface minimum is placed at $\gamma = 0$ for ^{108,110}Cd, whereas in this work the mean values for γ_{eff} extracted from the shell-model are 17.4° and 20.0°, respectively. A fact that has been commented on by V. Werner et al. [62], where it is noted, that β_{eff} and γ_{eff}, in general, do not exactly coincide with the minima of a corresponding energy surface for the ground state in the deformation parameter plane (page 4 right column). From the shape of the equipotential lines of the energy surface in Figure 6.8, it is obvious, that $\sigma(\beta)$ and $\sigma(\gamma)$ are predicted to posses nearly the same magnitude to acquire a circle like shape around the minimum. Also the energy potential is flater for β values between β_{eff} and $\beta = 0$, resulting in an asymmetry in $\sigma(\beta)$. The shell-model prediction does not account for this with a rather stretched out $\sigma(\beta)$ (or compressed $\sigma(\gamma)$ respectively), which is symmetric around β_{eff} by construction. The picture, that the deformation variances imply, is that a certain area of the deformation plane is occupied by the ground state averaged over time. Transferring $\sigma(\beta)$ to the energy surface 5-6 contour lines are covered by $\sigma(\beta)$ in increasing β direction in ^{108,110}Cd. As each contour represents 250 keV [71], the ground state covers an energy range up to $\sim$1500 keV, which includes the 4_1^+ states of ^{108,110}Cd. However, deviations between two different approaches are expected. The outcomes are in common, in the sense of exhibiting β- and γ-softness for both nuclei.

The black square symbols on the energy surfaces of Figure 6.8 indicate local minima, which are predicted to be intruder 0^+ states [71]. Although the intruder states are not implemented in the shell-model calculations, as already discussed in the end of Section 4.2.1, the presented outcome is well capable of analyzing the deformation of the underlying, non-intruder structure. Intruder states can be included by performing new shell-model calculations with a well balanced truncation of the valence proton space beyond the major $Z = 50$ shell gap. From these results the shape invariants of the 0_i^+ intruder states can be derived and the deformation characteristics can be analyzed. A verification of shape coexistence from within the shell model is therefore an open challenge for future works.

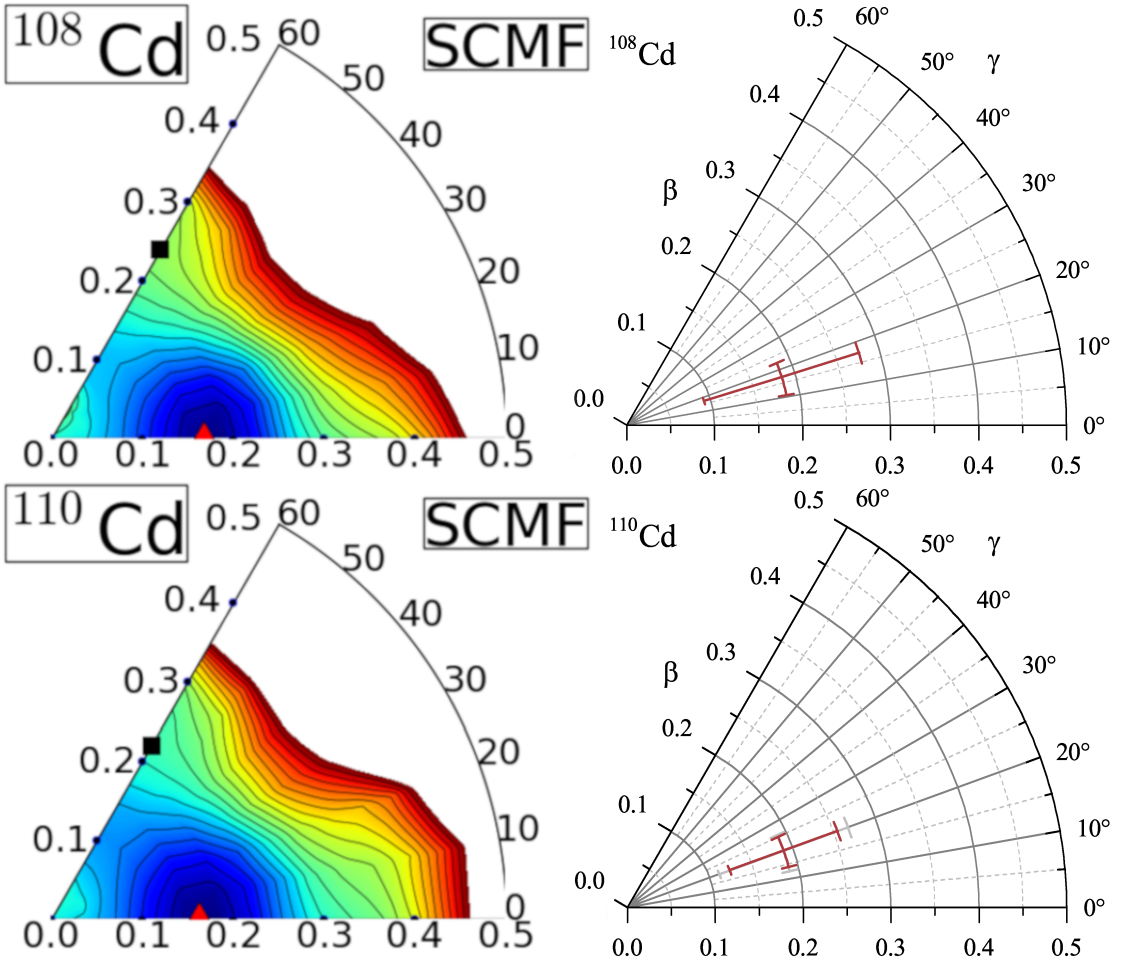

Figure 6.8: Left hand side: $\beta\gamma$ deformation energy surface of ^{108,110}Cd. Figure adopted form [71], energy difference between neighboring contours is 250 keV. Right hand side: Shell-model based β_{eff} and γ_{eff} of ^{108,110}Cd presented on the deformation plane together with the variances $\sigma(\beta)$ and $\sigma(\gamma)$.

7 Summary, conclusion, outlook

A (p, p') experiment was performed with the SONIC@HORUS spectrometer at the FN tandem accelerator at the Institute for Nuclear Physics, University of Cologne. The combination of particle and γ-ray detectors proved to be a powerful combination for spectroscopic analysis. The task of cross checking the results of the earlier experiments on ^{106}Cd, published in [27], confirmed many of the findings (compare Table 3.1) and solved discrepancies between previous works. In summary, 42 new γ-ray assignment and five new levels from Ref. [27] could be verified in this work, together with two level corrections compared to the literature [1] and one correction for a γ-ray assignment, i.e. the 535.9 keV line depopulating the 2252 keV level instead of the 2254 keV level, as presented in [27]. On top of that, many new results have been found in this work: 64 new γ-rays and 20 new levels have been discovered, 14 branching ratios could be corrected significantly, 8 levels stated in the literature [1] were proven to be falsely placed or non-existing. The improved knowledge about branching ratios originates mostly from the discovery of γ-ray doublets or multiplets and the ability to resolve them. 23 new multiplets were discovered among a total observation of 32 multiplets, applying a criterion of $<$3 keV for the distance between γ-rays. Therefore, the spectrum of ^{106}Cd has been found to obtain a dense distribution of γ-rays, making the analysis challenging. This can also be observed by looking at Table A.1 in the Appendix, where the results of this work are ordered by γ-ray energy. Branching ratios could be determined for all γ-ray transitions stated in Table 3.1, be it confirmed or newly discovered results. The new findings in the low energy region, especially the branching ratio correction of the 2_2^+ state at 1717 keV and the association of the 536 keV γ-ray to the 2252 keV, 3^+ state are considered significantly important, as they aid to crosscheck the vibrator picture. Values of transition strengths have been calculated from newly obtained lifetimes and multipolarity mixing ratios of the (n, n') data [28] including the branching ratios of this work. Therefore, a wide set of experimental data is now at hand for ^{106}Cd.

The experimental findings were compared to shell-model calculations from a spectroscopic point of view. Level schemes were build both from experimental and theoretical outcome. The comparison to the shell model calculations exhibited a good agreement in the low energy range concerning level energies and transition strength, especially in the Yrast band. Some expected deviations between both outcomes were observed, originating from the incapability of the used model space to reproduce intruder states. It was also found that ^{106}Cd shows an unexpected characteristic in level mixing in the energy range of the three phonon states, which could not be properly reproduced in the shell model calculations. Balancing between an extension of the proton model space beyond the $Z = 50$ major shell gap and at the same time applying a proper truncation of the proton occupation numbers could be a first approach to test the reproduction of intruder states within the shell model.

Strong hints were identified supporting the view that the newly discovered 3483 keV$\rightarrow$ 2371 keV transition is part of the intruder band in ^{106}Cd. Although no certain spin could be assigned to the 3483 keV level and no lifetime is available for this state, the level energy matches nicely into the V-shape pattern of cadmium 4_I^+ intruder states tracked over the neutron shell. The intensity of the supposed intruder band

transition relative to the 3483 keV$\rightarrow$ 1494 keV out of band transition reveals a strong connecting matrix element inside the band. A reanalysis of the (n, n') data could provide the necessary final proof for the existence of the intruder band, or provide the goal for a future experiment.

Rotational invariants have been derived from the shell-model output. The deformation parameters β, γ and their variances $\sigma(\beta)$ and $\sigma(\gamma)$ have been calculated. A convergence study of transition strength for the intermediate matrix elements has been performed. It was found that the calculated 50 0^+states and 50 2^+ states are sufficient to obtain an adequate amount of convergence in the strength functions of the studied isotopes. Some higher lying states did not reach the convergence plateau but contribute to lesser extend to the overall transition strength of the invariants. The effect of under-represented 0^+ states in ^{110}Cd has been studied. A good approximation for the missing amount of $B(E2)$ strength was found for the deformation parameter $\sigma(\beta)$. The same approximation was adopted for $\sigma(\gamma)$, but is concluded to result in a slight overrepresentation of that value.

A deformation analysis was performed from the shell-model results, including the variances $\sigma(\beta)$ and $\sigma(\gamma)$. It was found that the even isotopes $^{98-110}$Cd are undergoing a transition from a soft spherical structure towards a stronger deformed one with triaxial symmetry and increased surface rigidity. The results were interpreted as a development starting from a $U(5)$-like vibrator structure towards a $O(6)$-like asymmetric γ-soft rotor, in terms of the IBM, supporting interpretations of other works [7, 18, 20, 21] about the structure of light cadmium isotopes. This first time derivation of the deformation parameters $\sigma(\beta)$ and $\sigma(\gamma)$ calculated from shell-model results proved to be a useful tool. Together with the invariant planes of [62], shown in Figure C.2, a qualitative picture about the development of the nuclear structure of light cadmium isotopes could be gained. A comparison to energy surfaces, derived from self-consistent mean-field calculations of Ref. [71] showed a reasonable agreement with this work. Calculating intruder states from the shell model and including them in the deformation analysis, is an interesting subject from the perspective of nuclear structure. As the invariants can be calculated, in principle, for any state, a study on shape coexistence from within the shell model is possible.

A Addition (p, p')-data analysis

Table A.1: Results of the $(p, p'\gamma)$-experiment ordered by γ-ray energy. Energy uncertainties are 0.3 keV.

E_γ [keV]	E_i [keV]	J_i^π [$\hbar$]	E_f [keV]	J_f^π [$\hbar$]	E_i [keV]	J_i^π [keV]	E_f [$\hbar$]	J_f^π [keV]
163.2	2468.3	(4)+	2305.1	4+	1201.1	2917.7	1	1716.6
214.1	2468.3	(4)+	2254.1	(2+,3+)	1210.2	2926.7	2-6	1716.6
225.9	2330.6	5+	2104.7	4+	1216.7	3547.3	3-7	2330.6
298.7	2629.3	5-	2330.6	5+	1216.9	2710.8	(2-6)	1493.9
339.2	2717.6	2+,3	2378.6	3-	1219.5	2936.2	2+,3+	1716.6
381.4	2486.1	2+,3+,4+	2104.7	4+	1243.3	3495.6	1,2+	2252.3
388	2104.7	4+	1716.6	2+	1298.7	2792.5	2-6	1493.9
427.4	2144.1	0+	1716.6	2+	1303.8	3020.5	2,3+	1716.6
432.9	2924.6	6+	2491.7	6+	1306.8	2800.6	2-6	1493.9
438.8	3328.2	2+	2889.3	1-2	1324	3119.4	1	1795.2
482.4	3371.9	1-4	2889.3	1-2	1344.7	3061.2	(1),2	1716.6
485.6	2630.1	2+	2144.1	0+	1376.3	3093	(2+)	1716.6
487.3	2792.5	2-6	2305.1	4+	1377.1	3725.2	0-4	2347.9
495.5	2800.6	2-6	2305.1	4+	1401.8	2895.7	2-6	1493.9
518.5	2889.3	1-2	2370.5	2+	1402.9	3119.4	1	1716.6
524.6	2629.3	5-	2104.7	4+	1426.7	2920.6	5-	1493.9
535.9	2252.3	3+,(4+)	1716.6	2+	1427.3	3222.4	1	1795.2
541	3044.2	8+	2503.4	6+	1433	2926.7	2-6	1493.9
541.6	2889.3	1-2	2347.9	(2)+	1442.7	2936.2	2+,3+	1493.9
548.1	2800.6	2-6	2252.3	3+,(4+)	1472.1	2104.7	4+	632.7
552.3	3044.2	8+	2491.7	6+	1497.7	3214.3	1-4	1716.6
553	3119.4	1	2566.3	2+	1511.5	2144.1	0+	632.7
558	3119.4	1	2561.6	0+	1518.5	3012.6	2-4	1493.9
567.7	3285.5	1-4	2717.6	2+,3	1518.7	3235.3	2,3+	1716.6
575.3	2370.5	2+	1795.2	0+	1525	3018.8	3+,(5)+	1493.9
592.6	3084.3	7+	2491.7	6+	1528.8	3245.5	(2+)	1716.6
593.5	3061.2	(1),2	2468.3	(4)+	1538	3916.5	1-5	2378.6
604.9	3323	2+,3	2717.6	2+,3	1565.6	3059.5	3	1493.9
610.8	2104.7	4+	1493.9	4+	1577.5	3829.8	2-6	2252.3
624.2	3127	7+	2503.4	6+	1599.1	3093	(2+)	1493.9
631.1	2936.2	2+,3+	2305.1	4+	1620	2252.3	3+,(4+)	632.7
632.7	632.7	2+	0.0	0+	1621.4	2254.1	(2+,3+)	632.7
640.6	3132.3	4-7	2491.7	6+	1667.1	4045.6	1-5	2378.6
640.7	3018.8	3+,(5)+	2378.6	3-	1672.5	2305.1	4+	632.7
653.9	2370.5	2+	1716.6	2+	1676	3392.6	1,2+	1716.6
654.1	3371.9	1-4	2717.6	2+,3	1704.2	3198.1	2-6	1493.9
687.8	2792.5	2-6	2104.7	4+	1715.2	2347.9	(2)+	632.7
687.9	3018.8	3+,(5)+	2330.6	5+	1716.7	1716.6	2+	0.0
691.2	3320.4	6-	2629.3	5-	1738	2370.5	2+	632.7

E_γ [keV]	E_i [keV]	J_i^π [$\hbar$]	E_f [keV]	J_f^π [$\hbar$]	E_i [keV]	J_i^π [keV]	E_f [$\hbar$]	J_f^π [keV]
694.2	3073	2	2378.6	3-	1745.9	2378.6	3-	632.7
696	2800.6	2-6	2104.7	4+	1746.6	4000.7	1-4	2254.1
713.6	3018.8	3+,(5)+	2305.1	4+	1778.7	3495.6	1,2+	1716.6
747.8	3126.4	1-4	2378.6	3-	1821.1	4075.2	1-4	2254.1
748.6	3119.4	1	2370.5	2+	1822.6	3539.1	0-4	1716.6
751.7	2468.3	(4)+	1716.6	2+	1829.6	3323	2+,3	1493.9
757.8	2252.3	3+,(4+)	1493.9	4+	1833.8	3328.2	2+	1493.9
766.4	3018.8	3+,(5)+	2252.3	3+,(4+)	1835.8	2468.3	(4)+	632.7
766.8	3328.2	2+	2561.6	0+	1839.4	3333.2	2-6	1493.9
769.4	2486.1	2+,3+,4+	1716.6	2+	1853.5	2486.1	2+,3+,4+	632.7
771.4	2566.3	2+	1795.2	0+	1928.9	2561.6	0+	632.7
771.7	3489.4	2-4	2717.6	2+,3	1933.6	2566.3	2+	632.7
780.2	3283.6	4-8	2503.4	6+	1933.9	3427.8	2,3+,4+	1493.9
787.9	3093	(2+)	2305.1	4+	1989.3	3483.2	2-4	1493.9
791.1	2895.7	2-6	2104.7	4+	1995.6	3489.4	2-4	1493.9
801.6	3132.3	4-7	2330.6	5+	1997.4	2630.1	2+	632.7
811.2	2305.1	4+	1493.9	4+	2003.6	3497.5	2-6	1493.9
819.1	3073	2	2254.1	(2+,3+)	2084.9	2717.6	2+,3	632.7
822.1	2926.7	2-6	2104.7	4+	2086.7	2719.4	1,2+	632.7
828.6	3320.4	6-	2491.7	6+	2191.1	2824.6	1	632.7
831.1	2936.2	2+,3+	2104.7	4+	2256.4	2889.3	1-2	632.7
831.9	3461.2	(6-)	2629.3	5-	2282.2	2914.9	0-4	632.7
835.2	2630.1	2+	1795.2	0+	2285.4	2917.7	1	632.7
835.7	3214.3	1-4	2378.6	3-	2293.6	2926.7	2-6	632.7
836.7	2330.6	5+	1493.9	4+	2303.4	2936.2	2+,3+	632.7
849.3	2566.3	2+	1716.6	2+	2340.3	2973.3	2	632.7
859.7	3328.2	2+	2468.3	(4)+	2370.3	2370.5	2+	0.0
861.2	1493.9	4+	632.7	2+	2380.2	3012.6	2-4	632.7
874.8	3366.5	8+	2491.7	6+	2387.5	3020.5	2,3+	632.7
907.2	3285.5	1-4	2378.6	3-	2426.7	3059.5	3	632.7
908.8	3539.1	0-4	2630.1	2+	2428.8	3061.2	(1),2	632.7
913.4	2630.1	2+	1716.6	2+	2439.6	3073	2	632.7
929.2	3495.6	1,2+	2566.3	2+	2459.9	3093	(2+)	632.7
974.5	2468.3	(4)+	1493.9	4+	2486.3	3119.4	1	632.7
980.5	3328.2	2+	2347.9	(2)+	2493.2	3126.4	1-4	632.7
992.2	2486.1	2+,3+,4+	1493.9	4+	2589.6	3222.4	1	632.7
992.8	3245.5	(2+)	2252.3	3+,(4+)	2601.8	3235.3	2,3+	632.7
997.8	2491.7	6+	1493.9	4+	2629.5	2630.1	2+	0.0
1000.8	2717.6	2+,3	1716.6	2+	2689	3323	2+,3	632.7
1009.5	2503.4	6+	1493.9	4+	2694.9	3328.2	2+	632.7
1024.3	3371.9	1-4	2347.9	(2)+	2719.3	2719.4	1,2+	0.0
1026.9	3357.5	3-7	2330.6	5+	2757.9	3392.6	1,2+	632.7
1027.9	3333.2	2-6	2305.1	4+	2793.2	3427.8	2,3+,4+	632.7
1029.3	2824.6	1	1795.2	0+	2823.4	2824.6	1	0.0

E_γ [keV]	E_i [keV]	J_i^π [$\hbar$]	E_f [keV]	J_f^π [$\hbar$]	E_i [keV]	J_i^π [keV]	E_f [$\hbar$]	J_f^π [keV]
1074.3	3328.2	2+	2254.1	(2+,3+)	2861.2	3495.6	1,2+	632.7
1083.9	1716.6	2+	632.7	2+	2888.2	2889.3	1-2	0.0
1094.2	2889.3	1-2	1795.2	0+	2916.3	2917.7	1	0.0
1112.7	3483.2	2-4	2370.5	2+	3060.8	3061.2	(1),2	0.0
1122.3	2917.7	1	1795.2	0+	3071.8	3073	2	0.0
1135.4	2629.3	5-	1493.9	4+	3118	3119.4	1	0.0
1141.1	3245.5	(2+)	2104.7	4+	3220.2	3222.4	1	0.0
1148	3495.6	1,2+	2347.9	(2)+	3244	3245.5	(2+)	0.0
1162.5	1795.2	0+	632.7	2+	3326.9	3328.2	2+	0.0
1172.7	2889.3	1-2	1716.6	2+	3391.4	3392.6	1,2+	0.0
1178	2973.3	2	1795.2	0+	3492.1	3495.6	1,2+	0.0

B Addition to convergence study of rotational invariants

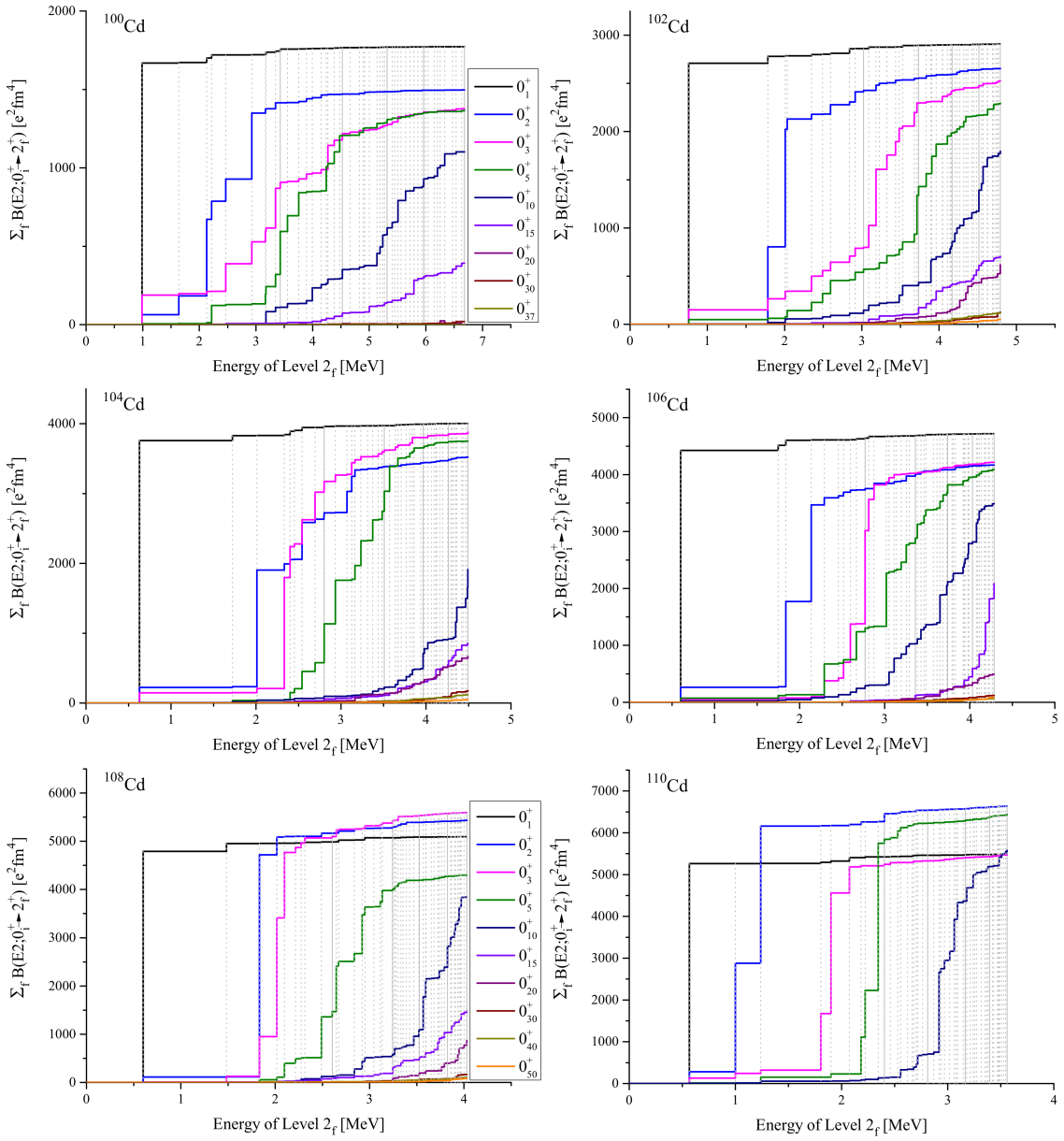

Figure B.1: A graphical illustration of the contributions of 2_f^+ states to the $B(E2)$ sums of 0_i^+ states as a function of energy of the various 2_f^+ states (with $f = 1, ...50$; ^{100}Cd: $f = 1, ...37$) on the horizontal axis. The sums give an impression of the convergence of matrix elements in Equations 6.10 and 6.12 necessary to calculate β and $\sigma(\beta)$. Vertical, dashed drop lines indicate the energies of the 2_f^+ states in each figure, with a solid drop line for every full set of ten 2^+ states. The color code given for ^{108}Cd is valid also for ^{102,104,106,110}Cd.

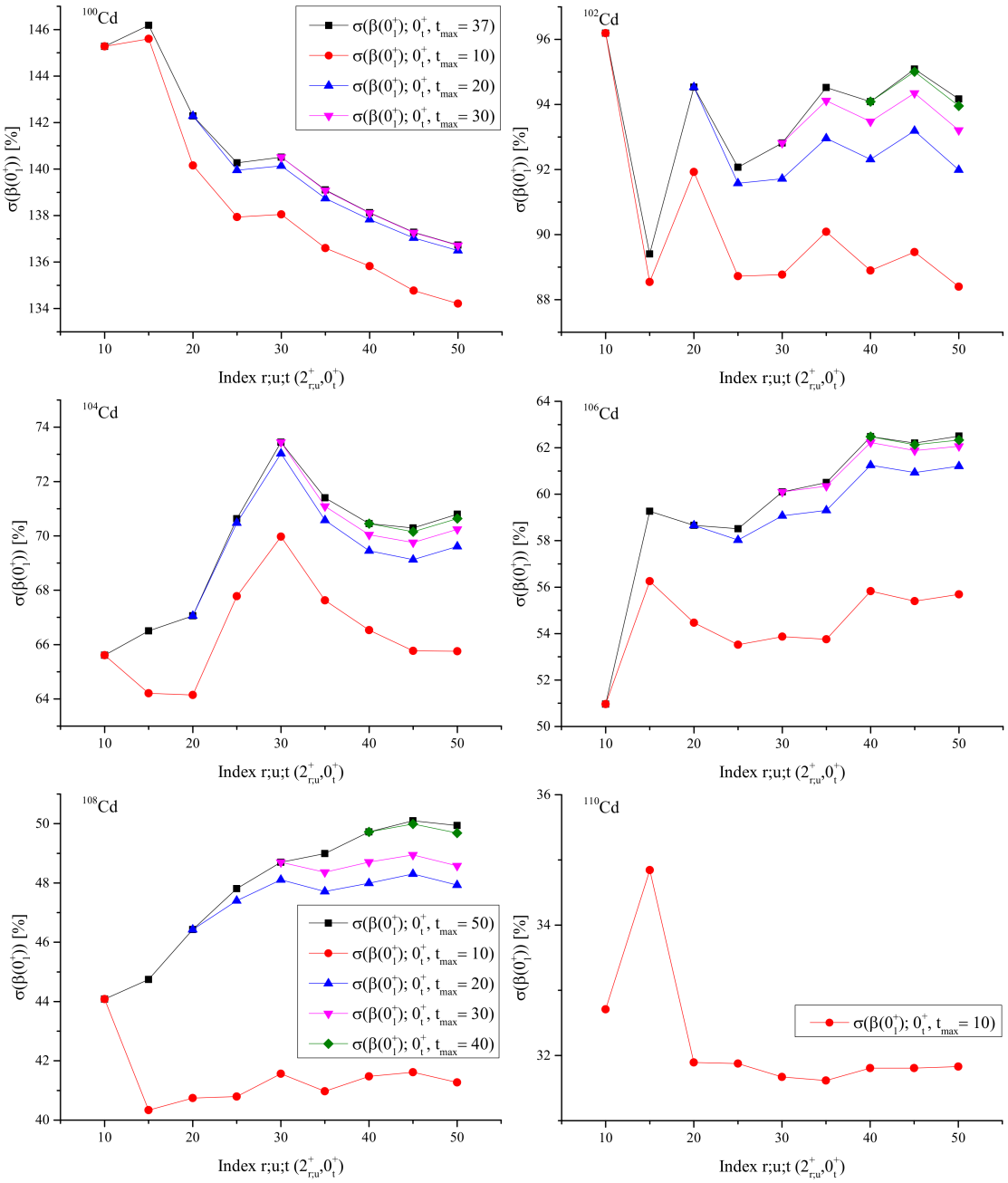

Figure B.2: Mapping of $\sigma(\beta)$ under the variance of contributing intermediate SM 2^+ and 0^+ states in Equation 6.12. The notation of spin indices is equal to Equation 6.12. The color code given for ^{108}Cd is valid also for ^{102,104,106}Cd.

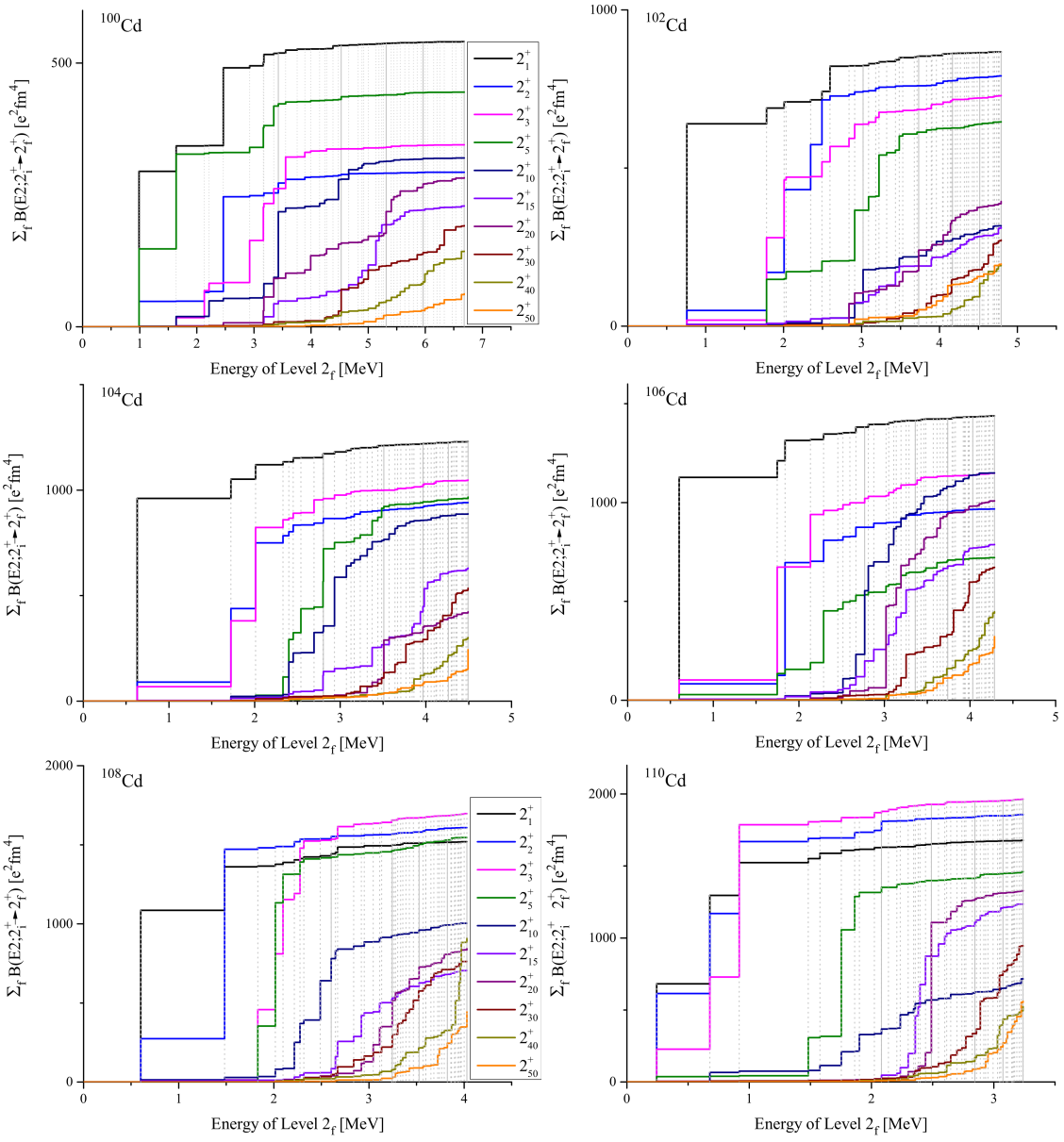

Figure B.3: A graphical illustration of the contributions of 2_f^+ states to the $B(E2)$ sums of other 2_i^+ states as a function of energy of the various 2_f^+ states (with $f = 1, ...50$) on the horizontal axis. The sums give an impression of the convergence of matrix elements in Equations 6.11 and 6.13 necessary to calculate γ and $\sigma(\gamma)$. Vertical, dashed drop lines indicate the energies of the 2_f^+ states in each figure, with a solid drop line for every full set of ten 2^+ states. The color code given for ^{100,108}Cd is valid for all shown isotopes.

C Addition to deformation analysis

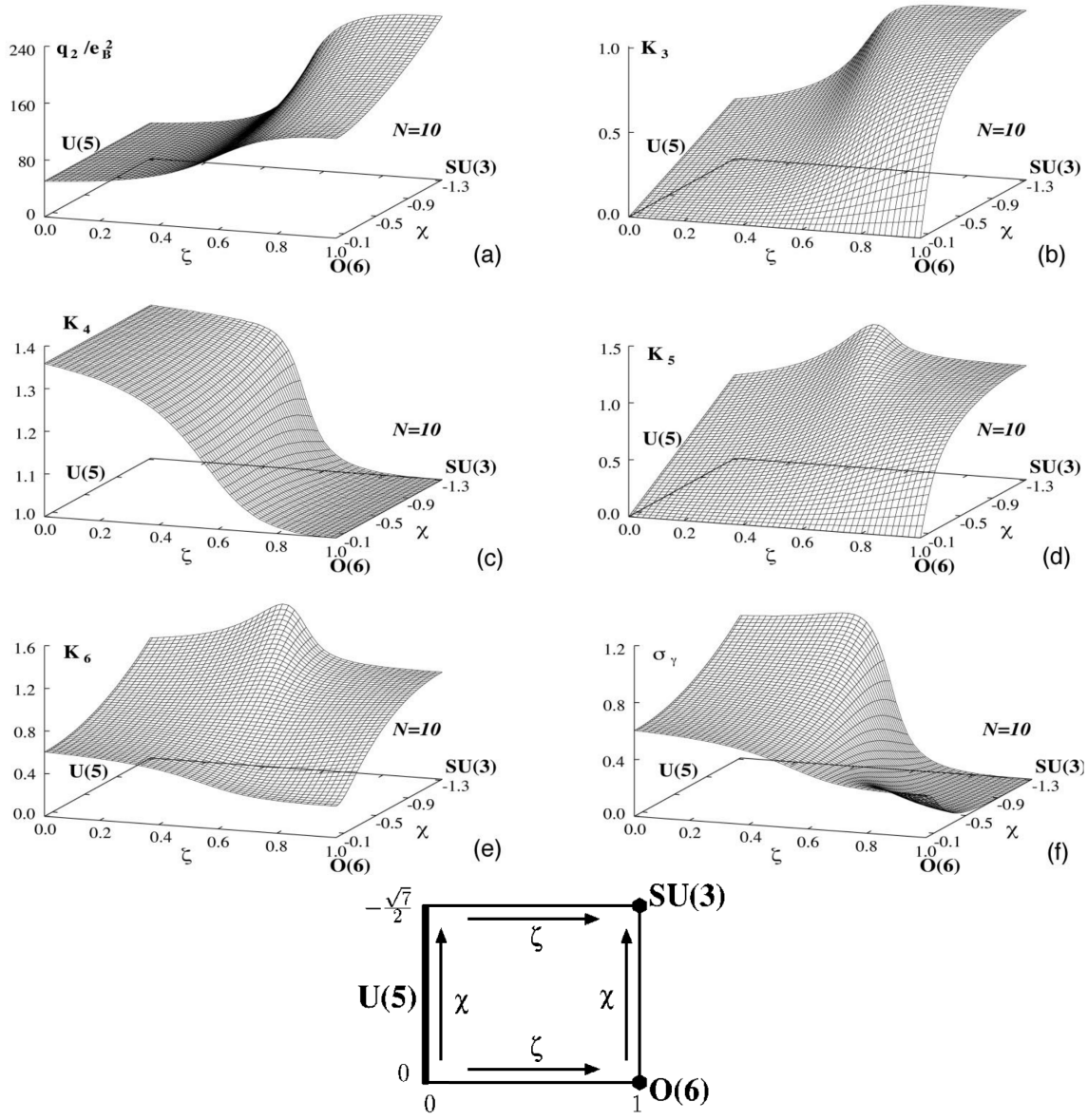

Figure C.1: Adopted figures from [62] showing values of shape invariants derived from IBM-1 calculations for 10 bosons. The structural constants ζ and χ of the IBM Hamiltonian have been varied grid wise over the full range. The $U(5)$ symmetry spans along the left χ-axis at $\zeta = 0$, whereas the $O(6)$ and $SU(3)$ symmetries are corresponding to two of the corners of the ECQF square. The figures present outcomes of Equations 6.15 : (a), 6.16 : (b), 6.17 : (c), 6.18 : (e), 6.20 : (f). Note that K_4 determines $\sigma(\beta) = K_4 - 1$ and $\sigma(\gamma)$ of Figure (e) denotes $\sigma(\cos 3\gamma)$ in common with the notation in this work.

	β	$\sigma(\beta)$	γ	$\sigma(\gamma)_+$	$\sigma(\gamma)_-$	K_3	K_4	K_6	$\sigma(\cos 3\gamma)$
^{98}Cd	0.072*	-	7.8°*	-	-	-	-	-	-
^{100}Cd	0.115	0.157 (137%)	12.3°	12.0° (97%)	27.6° (224%)	0.80	1.16	1.14	0.50
^{102}Cd	0.145	0.136 (95%)	13.0°	8.9° (68%)	23.3° (179%)	0.78	1.14	0.97	0.36
^{104}Cd	0.168	0.119 (71%)	13.7°	8.3° (61%)	22.5° (164%)	0.75	1.12	0.92	0.35
^{106}Cd	0.180	0.105 (58%)	15.2°	6.5° (43%)	11.1° (73%)	0.70	1.10	0.77	0.28
^{108}Cd	0.185	0.092 (50%)	17.4°	5.1° (30%)	6.7° (38%)	0.61	1.09	0.61	0.23
^{110}Cd	0.189	0.065 (34%)	20.0°	5.0° (25%)	5.9° (30%)	0.50	1.07	0.49	0.24
correction $\sigma_{\sim 20\%}$:		0.078 (41%)		5.9° (30%)	7.3° (37%)				0.29

Table C.1: Complete set of Deformation parameters β, $\sigma(\beta)$, γ , $\sigma_{\pm}(\gamma)$ and $\sigma(\cos 3\gamma)$ and the rotational invariants K_3, K_4 and K_6 they are derived of.
The last line gives by $\sim 20\%$ corrected variances. Corrections for $\sigma(\gamma)$ and and $\sigma(\cos 3\gamma)$ should rather be considered a substitute.
* Values taken from [22].

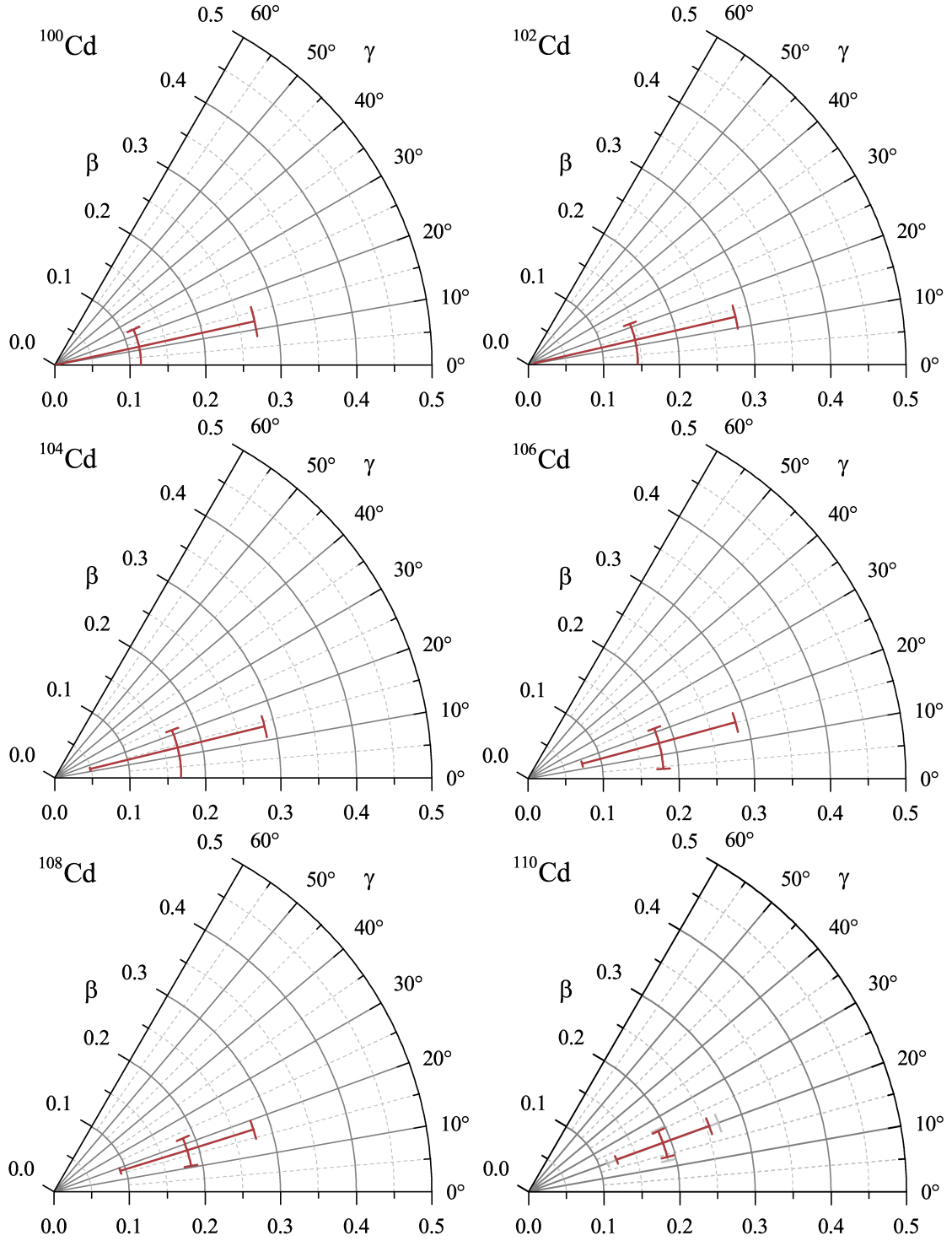

Figure C.2: Figures of the deformation planes of $^{100-110}$Cd illustrating the development of shape formation. With increasing neutron number the shape evolves from a rather soft regime to a more rigid one.

References

[1] National Nuclear Data Center (NNDC). *Brookhaven National Laboratory, http://www.nndc.bnl.gov/ensdf/*, December 2018.

[2] C. F. Weizäcker. Zur Theorie der Kernmassen. *Zeitschrift f. Physik*, 96:431, 1935.

[3] A. Bohr and B. R. Mottelson. *Collective And Individual-Particle Aspects Of Nuclear Structure.* Mat Fys Medd Dan Vid Selsk 27, 16, 1953.

[4] A. Bohr and B. R. Mottelson. *Nuclear Strucure Volume II: Nuclear Deformations.* World Scientic Publishing, 1998.

[5] D. J. Rowe. *Nuclear Collective Motion - Models and Theory.* Methuen And Co. Ltd., 1970.

[6] J. Eisenberg and W. Greiner. *Nuclear Theory Vol. 1 - Nuclear Models.* North-Holland Physics Publishing, 1987.

[7] P. E. Garrett and J. L. Wood. On the robustness of surface vibrational modes: case studies in the cd region. *J. Phys. G*, 37:064028, and corrigendum 06970128, 2010.

[8] R. F. Casten. *Nuclear Structure from a Simple Perspective.* Oxford University Press, 2 edition, 2005.

[9] R. De Leo, N. Blasi, S. Micheletti, M. Pignanelli, W. T. A. Borghols, J. M. Schippers, S. Y. van der Werf, G. Maino, and M. N. Harakeh. Multipole Strength Distribution In ^{112}Cd. *Nucl. Phys. A*, 1989.

[10] M. Dèléze, S. Drissi, J. Jolie, J. Kern, and J. P. Vorlet. The ^{112}Cd nucleus: a laboratory for the study of collective excitations. *Nucl. Phys. A*, 554:1, 1993.

[11] K. Schreckenbach, A. Mheemeed, G. Barreau, T. von Egidy, H. R. Faust, H. G. Börner, R. Brissot, M. L. Stelts, K. L. G. Heyde, P. Van Isacker, M. Waroquier, and G. Wenes. The Importance Of Intruder States ^{114}Cd. *Phys. Lett. B*, 110:364, 1982.

[12] K. L. G. Heyde, P. Van Isacker, M. Waroquier, G. Wenes, and M. Sambataro. Description of low-lying levels in ^{112,114}Cd. *Phys. Rev. C*, 25(6):3160, 1982.

[13] A. Aprahamian, D. S. Brenner, R. F. Casten, R. L. Gill, A. Piotrowski, and K. L. G. Heyde. Observation Of 0^+ States In ^{118}Cd And The Systematic Of Intruder States. *Phys. Lett. B*, 140:22, 1984.

[14] J. Jolie and H. Lehmann. On the influence of the O(5) symmetry on shape coexistence in atomic nuclei. *Phys. Lett. B*, 342:1, 1995.

[15] H. Lehmann and J. Jolie. The U(5)-O(6) model: an analytical approach to shape coexistence. *Nucl. Phys. A*, 588:623, 1995.

[16] K. L. G. Heyde, J. Jolie, H. Lehmann, C. De Coster, and J. L. Wood. Coexistence in even-even Cd nuclei: global structure and local perturbations. *Nucl. Phys. A*, 586:1, 1995.

[17] H. Lehmann, J. Jolie, C. De Coster, B. Decroix, K. L. G. Heyde, and J. L. Wood. Particle-hole excitations in the interacting boson model (ii): The U(5)-O(6) coupling. *Nucl. Phys. A*, 621:767, 1997.

[18] P. E. Garrett, K. L. Green, and J. L. Wood. Breakdown of vibrational motion in the isotopes $^{110-116}$Cd. *Phys. Rev. C*, 78:044307, 2008.

[19] K. L. G. Heyde and J. L. Wood. Shape coexistence in atomic nuclei. *Rev. Mod. Phys.*, 83:1467, 2011.

[20] P. E. Garrett, J. Bangay, A. Diaz Varela, G. C. Ball, D. S. Cross, G. A. Demand, P. Finlay, A. B. Garnsworthy, K. L. Green, G. Hackman, C. D. Hannant, B. Jigmeddorj, J. Jolie, W. D. Kulp, K. G. Leach, J. N. Orce, A. A. Phillips, A. J. Radich, E. T. Rand, M. A. Schumaker, C. E. Svensson, C. Sumithrarachchi, S. Triambak, N. Warr, J. Wong, J. L. Wood, and S. W. Yates. Detailed spectroscopy of ^{110}Cd: Evidence for weak mixing and the emergence of γ-soft behavior. *Phys. Rev. C*, 86:044304, 2012.

[21] A. Gade, J. Jolie, and P. von Brentano. First observation of the intruder band in ^{108}Cd. *Phys. Rev. C*, 65:041305(R), 2002.

[22] T. Schmidt, K. L. G. Heyde, A. Blazhev, and J. Jolie. Shell-model-based deformation analysis of light cadmium isotopes. *Phys. Rev C*, 96(014302), 2017.

[23] H. Moringa and T. Yamazaki. *In-Beam Gamma-Ray Spectroscopy.* North-Holland Publishing Company Amsterdam New York Oxford, 1976.

[24] M. R. Baht and M. J. Martin. Procedures manual for the Evaluated Nuclear Structure Data File. *National Nuclear Data Center, Upton, NY (USA)*, 1987.

[25] K. L. G. Heyde. *The Nuclear Shell Model.* Springer-Verlag, 1990.

[26] K. Krane. *Introductory Nuclear Physics.* John Wiley & Sons, 1988.

[27] A. Linnemann. *Das HORUS-Würfelspektrometer und Multipolanregungen in ^{106}Cd.* PhD thesis, Universität zu Köln, 2006.

[28] Sharmistha Mukhopadhyay. *Private Communication.* University of Kentucky, Department of Physics & Astronomy.

[29] N. Warr. *Private Communication.* Institut für Kernphysik, Universität zu Köln.

[30] J. Kumpulainen, R. Julin, J. Kantele, A. Passoja, W. H. Trzaska, E. Verho, and J. Väärämäki. Systematic study of low-spin states in even Cd nuclei. *Phys. Rev. C*, 45(2):640, 1992.

[31] S. G. Pickstone, M. Weinert, M. Färber, F. Heim, E. Hoemann, J. Mayer, M. Müscher, S. Prill, P. Scholz, M. Spieker, V. Vielmetter, J. Wilhelmy, and A. Zilges. Combining γ-ray and particle spectroscopy with SONIC@HORUS. *Nucl. Inst. Meth. A*, 875:104–110, 2017.

[32] F. Pühlhofer. On The Interpretation Of Evaporation Residue Mass Distributions In Heavy-Ion Induced Fusion Reactions. *Nucl. Phys. A*, 280:267, 1977.

[33] B. Hubbard-Nelson, M. Momayezi, and W. K. Warburton. A module for energy and puls shape data acquisition. *Nucl. Instrum. Methods Phys. Res. A*, 422:411, 1999.

[34] A. Henning. *Study of Proton-Neutron Mixed-Symmetry Excitations in ^{96}Ru by Means of Inelastic Proton Scattering and Digital Pulse Processing of Semiconductor Detector Signals*. PhD thesis, Universität zu Köln, 2014.

[35] N. Saed-Samii. SOCOv2. *https://gitlab.ikp.uni-koeln.de/nima/soco-v2*, 2018.

[36] M.A. Farouk and A.M. Al-Soraya. ^{226}Ra as a standard source for efficiency calibration of Ge(Li) detectors. *Nuclear Instruments and Methods*, 200:593–595, 1982.

[37] I. Wiedenhöver. *Vollständige Gamma-Spektroskopie des Kerns ^{127}Xe*. PhD thesis, Universität zu Köln, 1994.

[38] D.C. Radford. Radware-package. *https://radware.phy.ornl.gov/gf3/*, May 2000.

[39] S.A.Berendakov, L.I.Govor, A.M.Demidov, and I.V.Mikhailov. Gamma-rays from the ^{106}Cd(n, n'γ) reaction. *INDC(CCP)*, 299/G:26, 1988.

[40] W.T. Milner, F.K. McGowan, P.H. Stelson, R.L. Robinson, and R.O. Sayer. Coulomb excitation of the even-a cadmium nuclei. *Nuclear Physics A*, 129:687–696, 1969.

[41] B. Roussière, P. Kilcher, J. Sauvage-Letessier, C. Bourgeois, R. Beraud, R. Duffait, M. Meyer J. Genevey-Rivier, and J. Treherne. Decays of $^{108m+g}$In and $^{106m+g}$In. *Nuclear Physics A*, 419:61–76, 1984.

[42] S. Flanagan, R. Chapman, J. L. Durell, W. Gelletly, and J. N. Mo. The decay of 5.3min ^{106}In and 6.3min ^{106}In. *J. Phys. G: Nucl. Phys*, 2(8), 1976.

[43] H. Huang, B. P. Pathak, and J. K. P. Lee. Decay of $^{104,106m+g}$In. *Can. J . Phys.*, 56:936, 1978.

[44] A. Linnemann, C. Fransen, J. Jolie, U. Kneissl, P. Knoch, C. Kohstall, D. Mücher, H. H. Pitz, 2, M. Scheck, C. Scholl, F. Stedile, P. von Brentano, N. Warr, and V. Werner. Low-lying j = 1 states in ^{106}Cd. *Phys. Rev. C*, 75:024310, 2007.

[45] L. E. Samuelson, J. A. Grau, S. I. Popik, F. A. Rickey, and P. C. Simms. States in ^{106}Cd populated by heavy-ion (xn) reactions interpreted by a two-quasiparticle-plus-rotor model. *Phys. Rev. C*, 19(1):73–95, 1979.

[46] T. Mayer-Kuckuk. *Kernphysik*. Teubner Verlag, 1992.

[47] J. Daniére, R. Béraud, M. Meyer, and R. Rougny. High-spin states in ^{106}Cd. *Z. Physik A*, 280:363–369, 1977.

[48] C.L. Starke, E.A. Phillips, and E.H. Spejewski. Radioactivity of ^{105}Cd and ^{106}In. *Nuclear Physics A*, 139:33–41, 1969.

[49] I.N. Wischnewski, H.V. Klapdor, P. Herges, H. Fromm, and W.A. Zheldonozhski. Investigation of the β^+-decay of ^{105,106,108}In and of ^{100,102}Ag. *Z. Physik A*, 298:21, 1980.

[50] Dan Jerrestam, B. Cederwall, B. Fogelberg, A. Gizon, J. Gizon, L. Hildingsson, E. Ideguchie, W. Klamra, J. Kownacki, F. Lidén, Tb. Lindbladband S. Mitarai, and J. Nyberg. Collective excitations in ^{106}Cd. *Nuclear Physics A*, 571:393, 1994.

[51] P.H. Regan, A.E. Stuchbery, G.D. Dracoulis, A.P. Byrne, G.J. Lane, T. Kibédi, D.C. Radford, A. Galindo-Uribarri, V.P. Janzen, D. Ward, S.M. Mullins, G. Hackman, J.H. DeGraaf, M. Cromaz, and S. Pilotte. High-spin proton and neutron intruder configurations in ^{106}Cd. *Nuclear Physics A*, 586:351, 1995.

[52] W. Klamra and E. Dafni. Collective band structures in ^{106,107}Cd. *Z. Phys. A*, 334:515, 1989.

[53] S. F. Ashley, P. H. Regan, K. Andgren, E. A. McCutchan, N. V. Zamfir, L. Amon, R. B. Cakirli, R. F. Casten, R. M. Clark, W. Gelletly, G. Gürdal, K. L. Keyes, D. A. Meyer, M. N. Erduran, A. Papenberg, N. Pietralla, C. Plettner, G. Rainovski, R. V. Ribas, N. J. Thomas, J. Vinson, D. D. Warner, V. Werner, E. Williams, H. L. Liu, , and F. R. Xu. Intrinsic state lifetimes in ^{103}Pd and ^{106,107}Cd. *Phys. Rev. C*, 76:064302, 2007.

[54] A. Bohr and B. R. Mottelson. *Nuclear Strucure Volume I: Single-Particle Motion*. World Scientific, 1998.

[55] N. Shimizu. Nuclear shell-model code for massive parallel computation, "KSHELL". *arXiv:1310.5431*, 2013.

[56] D.J. Dean, T. Engeland, M. Hjorth-Jensen, M.P. Kartamyshev, and E. Osnes. Effective interactions and the nuclear shell-model. *Prog. Part. Nuc. Phys.*, 53:419–500, 2004.

[57] N. Boelaert, N. Smirnova, K. L. G. Heyde, and J. Jolie. Shell model description of the low-lying states of the neutron decient cd isotopes. *Phys. Rev. C*, 75:014316, 2007.

[58] R. Machleidt. High-precision, charge-dependent bonn nucleon-nucleon potential. *Phys. Rev. C*, 63:024001, 2001.

[59] N. Boelaert, A. Dewald, C. Fransen, J. Jolie, A. Linnemann, B. Melon, O. Möller, N. Smirnova, and K. L. G. Heyde. Low-spin electromagnetic transition probabilities in 102,104 cd. *Phys. Rev. C*, 75:054311, 2007.

[60] N. Saed-Samii. TRANSNUCULAR. *https://gitlab.ikp.uni-koeln.de/nima/transnucular*, 2019.

[61] H. W. Fielding, R. E. Anderson, C. D. Zafiratos, D. A. Lind, F. E. Cecil, H. H. Wieman, and W. P. Alford. 0^+ States Observed In Cd And Sn Nuclei With The (^{3}He,n) Reaction. *Nucl. Phys. A*, 281:389 – 404, 1977.

[62] V. Werner, N. Pietralla, P. von Brentano, R. F. Casten, and R. V. Jolos. Quadrupole shape invariants in the interacting boson model. *Phys. Rev. C*, 61:021301(R), 2000.

[63] K. Kumar. Intrinsic quatrupole moments and shapes of nuclear ground states and excited states. *Phys. Rev. Letters*, 28:249, 1972.

[64] D. Cline. Nuclear shapes studied by coulomb excitation. *Annu. Rev. Nucl. Part. Sci.*, 36:683, 1986.

[65] R. V. Jolos, P. von Brentano, N. Pietralla, and I. Schneider. Shape invariants in the multiple "Q-excitation" scheme. *Nucl. Phys. A*, 618:126, 1997.

[66] Yu. V. Palchikov, P. von Brentano, and R. V. Jolos. Universal description of the 0_2^+ state in collective even-A nuclei. *Phys. Rev. C*, 57(6):3026, 1998.

[67] C. W. Johnson, W. E. Ormand, and P. G. Krastev. Factorization in large-scale many-body calculations. *Comp. Phys. Comm.*, 184:2761, 2013.

[68] N. Pietralla, P. von Brentano, R. F. Casten, T. Otsuka, and N. V. Zamfir. Distribution of low-lying quadrupole phonon strength in nuclei. *Phys. Rev. Lett.*, 73:2962, 1994.

[69] A. Ekström, J. Cederkäll, D. D. DiJulio, C. Fahlander, M. Hjorth-Jensen, A. Blazhev, B. Bruyneel, P. A. Butler, T. Davinson, J. Eberth, C. Fransen, K. Geibel, H. Hess, O. Ivanov, J. Iwanicki, O. Kester, J. Kownacki, U. Köster, B. A. Marsh, P. Reiter, M. Scheck, B. Siebeck, S. Siem, I. Stefanescu, H. K. Toft, G. M. Tveten, J. Van de Walle, D. Voulot, N. Warr, D. Weisshaar, F. Wenander, K. Wrzosek, and M. Zielińska. Electric quadrupole moments of the 2+1 states in 100, 102, 104 cd. *Phys. Rev. C*, 80:054302, 2009.

[70] M. T. Esat, D. C. Kean, and R. H. Spear. Mass Dependence Of The Static Quadrupole Moments Of The First 2^+ States In The Cadmium Isotopes. *Nucl. Phys. A*, 274:237, 1976.

[71] K. Nomura and J. Jolie. Structure of even-even Cadmium isotopes from the beyond-mean-field interacting boson model. *Phys. Rev. C*, 98(024303), 2018.

Erklärung

Ich versichere, dass ich die von mir vorgelegte Dissertation selbständig angefertigt, die benutzten Quellen und Hilfsmittel vollständig angegeben und die Stellen der Arbeit – einschließlich Tabellen, Karten und Abbildungen –, die anderen Werken im Wortlaut oder dem Sinn nach entnommen sind, in jedem Einzelfall als Entlehnung kenntlich gemacht habe; dass diese Dissertation noch keiner anderen Fakultät oder Universität zur Prüfung vorgelegen hat; dass sie – abgesehen von unten angegebenen Teilpublikationen – noch nicht veröffentlicht worden ist, sowie, dass ich eine solche Veröffentlichung vor Abschluss des Promotionsverfahrens nicht vornehmen werde. Die Bestimmungen der Promotionsordnung sind mir bekannt. Die von mir vorgelegte Dissertation ist von Prof. Dr. Jan Jolie betreut worden.

Teilpublikationen
keine

Köln, 09. September 2019

(Tobias Schmidt)